6-2023

NUMERICAL SIMULATION OF CONCRETE BEAMS WITH DISCONTINUITY REGIONS REINFORCED WITH NONMETALLIC REINFORCING BARS

Amena Mohammad Ousama

NUMERICAL SIMULATION OF CONCRETE BEAMS WITH DISCONTINUITY REGIONS REINFORCED WITH NONMETALLIC REINFORCING BARS
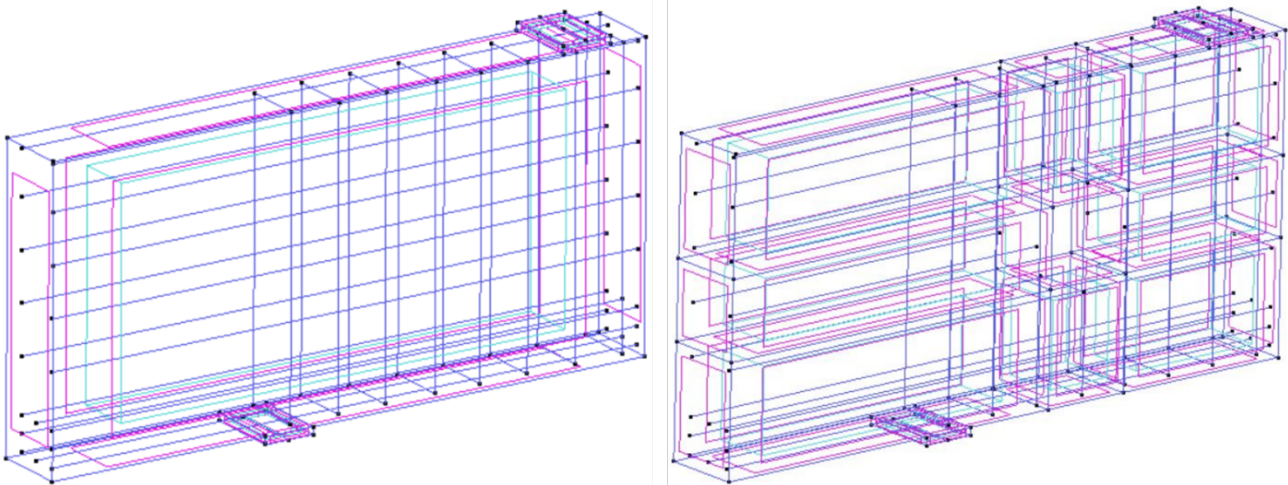
Amena Mohammad Ousama Sheikh Sobeh

United Arab Emirates University

College of Engineering

Department of Civil and Environmental Engineering

NUMERICAL SIMULATION OF CONCRETE BEAMS WITH
DISCONTINUITY REGIONS REINFORCED WITH
NONMETALLIC REINFORCING BARS

Amena Mohammad Ousama Sheikh Sobeh

This thesis is submitted in partial fulfilment of the requirements for the degree of Master
of Science in Civil Engineering

June 2023

Cover: Three-dimensional (3D) numerical models solid and with web opening.

(Photo: By Amena Mohammad Ousama Sheikh Sobeh)

Declaration of Original Work

I, Amena Mohammad Ousama Sheikh Sobeh, the undersigned, a graduate student at the United Arab Emirates University (UAEU), and the author of this thesis entitled *"Numerical Simulation of Concrete Beams with Discontinuity Regions Reinforced with Nonmetallic Reinforcing Bars"*, hereby, solemnly declare that this is the original research work done by me under the supervision of Prof. Tamer El Maaddawy, in the College of Engineering at UAEU. This work has not previously formed the basis for the award of any academic degree, diploma or a similar title at this or any other university. Any materials borrowed from other sources (whether published or unpublished) and relied upon or included in my thesis have been properly cited and acknowledged in accordance with appropriate academic conventions. I further declare that there is no potential conflict of interest with respect to the research, data collection, authorship, presentation and/or publication of this thesis.

Student's Signature: *Amena. Sh. S*

Date: 14.06.2023

Advisory Committee

1) Advisor: Tamer El Maaddawy

Title: Professor

Department of Civil and Environmental Engineering

College of Engineering

2) Co-advisor: Nancy Kachouh

Title: Visiting Faculty

Department of Civil and Environmental Engineering

College of Engineering

Approval of the Master Thesis

This Master Thesis is approved by the following Examining Committee Members:

1) Advisor (Committee Chair): Tamer El Maaddawy
   Title: Professor
   Department of Civil and Environmental Engineering
   College of Engineering

   Signature ⟨signature⟩ Date 14.06.2023

2) Member: Bilal El-Ariss
   Title: Associate Professor
   Department of Civil and Environmental Engineering
   College of Engineering

   Signature ⟨signature⟩ Date 14.06.2023

3) Member (External Examiner): Abdeldjelil Belarbi
   Title: Professor
   Department of Civil and Environmental Engineering
   Institution: University of Houston, USA
   Program coordinator of behalf of external examiner

   Signature ⟨signature⟩ Date 14.06.2023

This Master Thesis is accepted by:

Dean of the College of Engineering: Professor Mohamed Al Marzouqi

Signature Mohamed AlMarzouqi

Date July 18, 2023

Dean of the College of Graduate Studies: Professor Ali Al-Marzouqi

Signature Ali Hassan

Date 18/07/2023

Abstract

Nonmetallic Glass Fiber-Reinforced Polymer (GFRP) reinforcing bars are considered a viable alternative to the conventional steel reinforcement because of their high strength-to-weight ratio and noncorrosive nature. This research aimed to investigate the nonlinear structural behavior of GFRP-reinforced concrete beams with discontinuity regions (D-regions) through numerical analysis. Three-dimensional (3D) numerical models were developed to simulate the nonlinear structural behavior of GFRP-reinforced deep beams with and without web openings. The models adopted realistic constitutive laws that accounted for the nonlinear behavior of the materials used. Predictions of the numerical models were validated against published experimental data. A parametric study was conducted to examine the effect of key variables on the structural behavior of GFRP-reinforced deep beams with and without web openings. The interaction between the concrete compressive strength (f_c'), shear span-to-depth ratio (a/h), size and location of the web opening was elucidated. Simplified analytical formulas capable of predicting the shear capacity of GFRP-reinforced beams with D-regions were introduced based on an inverse analysis of results of the numerical simulation models. Predictions of the proposed analytical formulas were in good agreement with the results of the simulation models.

Keywords: Deep beams, GFRP, Numerical, Openings, Simulation, Shear.

Title and Abstract (in Arabic)

محاكاة عددية للجسور الخرسانية التي تحتوي علي مناطق انقطاع والمسلحة بقضبان غير معدنية

الملخص

تعتبر قضبان التسليح المصنوعة من البوليمر المقوى بالألياف الزجاجية غير المعدنية (GFRP) بديلاً قابلاً للتطبيق لحديد التسليح التقليدي بسبب نسبة القوة إلى الوزن العالية وطبيعة عدم التآكل. يهدف هذا البحث إلى دراسة السلوك الإنشائي غير الخطي للجسور الخرسانية المسلحة بـ GFRP و التي تحتوي علي مناطق عدم الاستمرارية (مناطق D) من خلال التحليل العددي. تم ابتكار نماذج رقمية ثلاثية الأبعاد (3D) لمحاكاة السلوك الهيكلي غير الخطي للجسور العميقة المسلحة بـ GFRP مع وبدون فتحات عرضية. اعتمدت النماذج على قوانين تأسيسية واقعية تفسر السلوك غير الخطي للمواد المستخدمة. تم التحقق من صحة تنبؤات النماذج العددية مقابل البيانات التجريبية المنشورة. تم إجراء دراسة بارامترية لفحص تأثير المتغيرات الرئيسية على السلوك الهيكلي للجسور العميقة المسلحة بـ GFRP مع وبدون فتحات عرضية. تم استنتاج العلاقات بين قوة الضغط الخرسانية ونسبة مسافة القص إلى عمق الجسر، وحجم وموقع الفتحات عرضية. تم تقديم صيغ تحليلية مبسطة قادرة على التنبؤ بقدرة الجسور العميقة المسلحة بـ GFRP و التي تحتوي على مناطق عدم الاستمرارية (مناطق D) على مقاومة قوى القص بناءً على تحليل لنتائج نماذج المحاكاة العددية. كانت تنبؤات الصيغ التحليلية المقترحة متوافقة جيدًا مع نتائج نماذج المحاكاة.

مفاهيم البحث الرئيسية: الجسور العميقة، قضبان البوليمر المقوى بالألياف الزجاجية، النماذج العددية، فتحات عرضية، المحاكاة، قوى القص.

Acknowledgements

I would like to express the deepest appreciation to my committee for their guidance, support, and assistance throughout my preparation of this thesis, especially my advisor Prof. Tamer El Maaddawy for his continuous support and insights that have helped me complete this thesis work. His guidance and advice carried me through all stages of writing my thesis. I am very thankful for having the opportunity to have him as my advisor for my master's thesis. I would also like to sincerely thank Dr. Nancy Kachouh for her continuous support and motivation.

I am deeply grateful to my parents and siblings for their nonending support, appreciation, encouragement, and keen interest in my academic achievements.

Dedication

To my beloved parents and siblings

Table of Contents

List of Tables

List of Figures

xiv

List of Abbreviations

AFRP	Aramid Fiber-Reinforced Polymer
BFRP	Basalt Fiber-Reinforced Polymer
CFRP	Carbon Fiber-Reinforced Polymer
D-regions	Discontinuity Regions
FRP	Fiber-Reinforced Polymer
GFRP	Glass Fiber-Reinforced Polymer
RC	Reinforced Concrete
3D	Three-Dimensional

Chapter 1: Introduction

1.1 Overview

Discontinuity regions (D-regions) are formed in Reinforced Concrete (RC) beams due to statical or geometric discontinuities [1, 2]. The former are regions near concentrated loads and support reactions, whereas the latter are regions adjacent to web openings or abrupt changes in cross section [1, 2]. The D-regions in structural concrete members reinforced with steel reinforcing bars have been designed using dissimilar empirical equations that are not universally applicable [3]-[5]. Nonmetallic Fiber-Reinforced Polymer (FRP) reinforcing bars are considered a viable alternative to conventional steel reinforcement because of their high strength, light weight, and noncorrosive nature [6]-[12]. Types of composite reinforcing bars include Glass Fiber-Reinforced Polymer (GFRP), Carbon Fiber-Reinforced Polymer (CFRP), Basalt Fiber-Reinforced Polymer (BFRP), and Aramid Fiber-Reinforced Polymer (AFRP) (Figure 1.1) [12]. The GFRP reinforcing bars are also nonconductive and nonmagnetic. As such, the use of GFRP bars in reinforcing D-regions eliminates corrosion problems and magnetic interference [6]-[12]. The design of D-regions becomes, however, more challenging when conventional steel reinforcing bars are replaced by nonmetallic reinforcement such as GFRP composites.

(a)   (b)

(c)   (d)
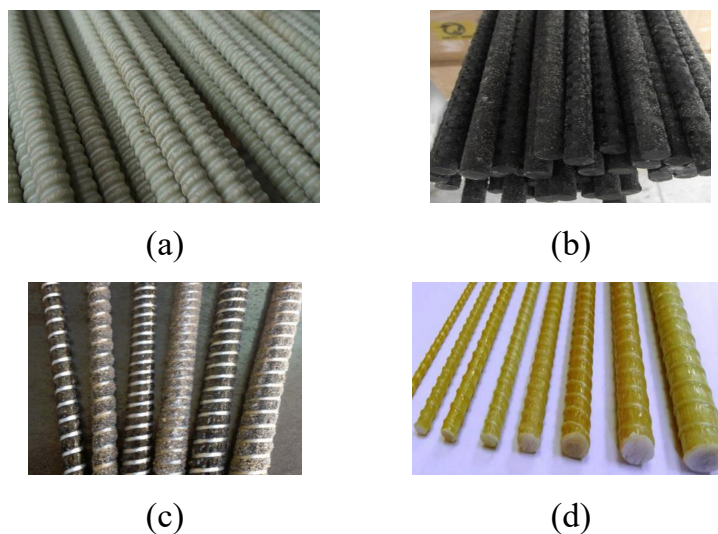
Figure 1.1: Four types of FRP bars [12]: (a) GFRP bars; (b) CFRP bars; (c) BFRP bars; (d) AFRP bars

1.2 Statement of the Problem

The analysis of D-regions in GFRP-reinforced concrete structural members is challenging to the structural engineering community due to the lack of knowledge on their behavior, noting that available codes and standards do not offer a closed form-solution for such a complex problem. The uncertainty in estimating the internal stresses and deformations of structural members with D-regions increases when conventional steel bars are replaced by GFRP reinforcement. The use of computers and numerical simulation tools have made it feasible to perform analysis of such complex structural members. This research aims to provide new knowledge on the behavior of GFRP-reinforced deep beams with and without a web opening through numerical analysis. Three-dimensional (3D) simulation models capable of predicting the structural behavior of GFRP-reinforced concrete beams with D-regions were developed and validated against published experimental data. A parametric study was conducted to investigate the influence of key parameters affecting the structural behavior of GFRP-reinforced concrete deep beams with and without a web opening. Refined simplified analytical formulas were introduced for shear strength prediction of GFRP-reinforced concrete beams with D-regions. Findings of this research offer an improved understanding of the behavior of GFRP-reinforced deep beams with and without a web opening. Such a new knowledge is anticipated to assist practitioners and researchers in designing concrete D-regions reinforced with GFRP bars. The outcomes of the study are anticipated to advance development of design guidelines and standards on reinforcing concrete structures with GFRP bars. The widespread use of GFRP reinforcing bars instead of the conventional steel reinforcement in construction would reduce repair cycles and operational costs with positive impacts on the UAE and worldwide.

1.3 Research Objectives

This research aims to investigate the structural behavior of GFRP-reinforced concrete deep beams with and without a web opening. The specific objectives are as follows:

2

- Develop 3D numerical simulation models for large-scale deep beams with and without a web opening internally reinforced with GFRP bars.
- Verify prediction of the numerical models through a comparative analysis with published experimental data.
- Conduct a parametric study to examine the effect of key parameters on the shear behavior of concrete deep beams with and without a web opening internally reinforced with GFRP bars.
- Introduce refined simplified analytical formulas that can predict the shear capacity of concrete beams with D-regions reinforced with GFRP bars.

1.4 Relevant Literature

Concrete deep beams, i.e., shear span-to-depth ratio $(a/h) \leq 2$, with and without a web opening, are influenced by both statical and geometric discontinuities [1, 2]. The discontinuity in statical loading or geometry causes a complex flow of internal stresses and nonlinear distribution of longitudinal strains within the cross section. As such, the traditional beam theory (Bernoulli hypothesis) applied in the analysis of conventional RC structural members (B-regions), is not valid for the analysis of D-regions [1]-[5]. Although the strut-and-tie modeling approach meets the fundamental principles of equilibrium of forces and compatibility of deformations for D-regions, its accuracy and validity are questionable because of the uncertainties in defining the strength and dimensions of the idealized load-resisting model [1]. In addition, existing codes of practice and design standards emphasize only the basic mechanics of the strut-and-tie modeling approach without providing a closed-form solution for the analysis of D-regions [1, 6]. Research on the shear behavior of concrete beams internally reinforced with FRP bars has attracted several researchers over the last two decades [13]-[35]. Table 1.1 summarizes test variables of previous studies [13]-[23] on the shear behavior of slender concrete beams reinforced with FRP bars, whereas those of other studies on beams with D-regions are summarized in Table 1.2 [24]-[35].

Table 1.1: Test parameters of previous studies on shear behavior of slender beams with FRP bars

References	Test Parameters						
	Beam Geometry		FRP Reinforcement			Material Properties	
	a/h	Web Opening	Flexural	Shear	Around Opening	Concrete	FRP
Tureyen and Frosch [13]			■				■
Guadagnini et al. [14]	■			■			
El-Sayed et al. [15]			■			■	■
El-Sayed et al. [16]			■				■
Bentz et al. [17]			■	■			
Kara [18]	■		■			■	■
Tomlinson and Fam [19]	■		■	■			
Refai and Abed [20]	■		■				
Issa et al. [21]	■		■	■			
Al-Hamrani and Alnahhal [22]	■		■	■		■	■
Refai et al. [23]	■		■			■	

Table 1.1: Test parameters of previous studies on shear behavior of deep beams with FRP bars

References	Test Parameters						
	Beam Geometry		FRP Reinforcement			Material Properties	
	a/h	Web Opening	Flexural	Shear	Around Opening	Concrete	FRP
Omeman et al. [24]	■		■			■	
Abed et al. [25]	■		■			■	
Farghaly and Benmokrane [26]			■			■	■
Andermatt and Lubell [27]	■		■			■	■
Kim et al. [28]	■		■				■
Liu et al. [29]	■		■			■	
Alhamad et al. [30]	■						
Abed et al. [31]	■		■				
Abu-Obaida et al. [32]	■		■			■	
Mohamed et al. [33]	■			■		■	
Frappier et al. [34]		■			■		
Arabasi and El-Maaddawy [35]		■			■	■	

Slender concrete beams (i.e., $a/h > 2$) reinforced with FRP bars are vulnerable to wider shear cracks, reduced contribution of the aggregate interlock, and weakened dowel action, which reduced the shear strength relative to that of beams reinforced with steel bars [13]-[23]. The shear resistance of slender concrete beams with FRP reinforcement is affected by the a/h ratio, flexural reinforcement ratio, spacing between stirrups, detailing of reinforcement around D-regions, concrete strength, and properties of the FRP material used. Several studies indicated that the shear capacity of slender beams increased with an increase in the longitudinal reinforcement ratio [13]-[23]. Similarly, the increase in the compressive strength of the concrete improved the shear capacity of the slender beams [15, 18, 22, 23]. A study by El-Sayed et al. [15] showed that increasing the compressive strength of slender concrete beams reinforced with carbon- and glass-FRP reinforcement by 44% increased the shear strength by 4 and 12%, respectively. The respective improvements in the shear strength caused by increasing the longitudinal FRP reinforcement ratio by 29% were 34 and 33% [15]. Another study conducted by El-Sayed et al. [16] showed that increasing the longitudinal reinforcement ratio by approximately 50% in slender beams reinforced with carbon-FRP bars, increased the shear strength by 46%; however, no shear strength gain was reported for similar beams reinforced with glass-FRP bars. Doubling the amount of the longitudinal reinforcement increased the shear strength of the beams with carbon- and glass-FRP bars by 77 and 17%, respectively [16]. Several studies concluded that slender concrete beams reinforced with FRP bars having a higher modulus of elasticity exhibited a higher shear strength [13, 15, 16, 18, 22]. Increasing the FRP reinforcement ratio or modulus of elasticity, increased the post-cracking stiffness of the tested beams [13, 15, 16, 18, 22]. Guadagnini et al. [14] and Al-Hamrani and Alnahhal [22] concluded that decreasing the spacing between the FRP shear reinforcement, increased the shear capacity and changed the failure mode from a diagonal tension shear mode of failure to a flexural compression failure. Previous studies indicated that the shear capacity of FRP-reinforced concrete beams increased as the a/h decreased [14], [18]-[23].

Numerous studies examined the shear behavior of FRP-reinforced concrete deep beams without web reinforcement [24]-[33]. The shear capacity of solid deep beams reinforced with FRP bars improved with an increase in the value of a/h, modulus of

elasticity and reinforcement ratio of longitudinal FRP bars, and concrete compressive strength [24]-[33]. Omeman et al. [24] reported that solid deep beams reinforced with carbon-FRP bars having a higher value of a/h and an increased effective depth exhibited a more catastrophic failure mode than that of their counterparts with a lower a/h and a reduced effective depth. Results of a study by Abed et al. [25] indicated that increasing the concrete strength of solid deep beams reinforced with longitudinal glass-FRP bars from 43 to 51 MPa (19%), increased the shear capacity by 44%. An additional increase in the concrete strength from 51 to 65% (27%) did not result in a proportional increase in the shear capacity, where an additional shear strength gain of 7% only was recorded [25]. As such, the researchers concluded that the shear strength gain caused by an increase in the concrete compressive strength had a threshold, although not determined in their investigation [25]. Increasing the longitudinal FRP reinforcement ratio by 50 and 100% increased the shear strength by 46% and 70%, respectively [24, 25]. Farghaly and Benmokrane [26] reported that increasing the longitudinal FRP reinforcement ratio-controlled widening of shear crack, where an increase in the FRP reinforcement ratio by 80% resulted in an average reduction in the crack width of 47%. Increasing the section height reduced the normalized shear stress at ultimate load of FRP-reinforced deep beams with a/h of 1.0 [27]. The effect of the section size was insignificant for the deep beams having $h \leq 600$ mm and a/h of 1.2 and 1.7 [27]. Kim et al. [28] indicated that the increase in the shear capacity of FRP-reinforced deep beams due to decreasing a/h, increasing h, or the longitudinal reinforcement ratio can be ascribed to an increase in the angle of inclination and/or width of the inclined concrete strut that governed the beam failure. Liu et al. [29] reported that decreasing the a/h by 11 and 24% increased the shear strength of FRP-reinforced deep beams by 32 and 43%, respectively. An inverse linear correlation between the shear capacity and the cubic root of a/d was reported for solid deep beams reinforced with FRP bars, where d is the beam effective depth [30, 31]. Abu-Obaida et al. [32] reported that a significant increase in longitudinal FRP reinforcement ratio together with the concrete strength was detrimental to the shear strength of FRP-reinforced short-beams without web reinforcement due to a change in the mode of failure from strut crushing to diagonal splitting.

6

Little information is available in the literature on the shear behavior of FRP-reinforced deep beams with web reinforcement and/or cutouts [33]-[35]. The high tensile strength of FRP bars and the absence of yielding could be beneficial in improving the strut capacity, reducing the stress concentrations around cutouts, thus rendering an increased shear capacity of D-regions [33]-[35]. Mohamed et al. [33] concluded that the use of vertical FRP stirrups improved the shear capacity of FRP-reinforced large-scale deep beams by 20%, whereas the use of horizontal web reinforcement solely was detrimental to the shear strength because of the high tensile strains in the horizontal bars that induced deterioration and softening of the concrete in the diagonal strut. Frappier et al. [34] examined the shear response of large-scale FRP-reinforced deep beams with *a/h* of 1.0 having a web opening in the middle of the shear span. The effect of FRP reinforcement details around the opening on the shear response was investigated. Results of the beams with web openings were compared to that of a solid beam with minimum FRP web reinforcement. The solid deep beams failed by crushing of the diagonal strut formed in the shear span between the load and support points. The beams with openings failed by crushing of the concrete along main diagonal cracks formed in the upper and lower chords between the load/support points and opposites corners of the openings prior to failure. Localized rupture around the bent portion of FRP vertical stirrups located between the support plate and vertical side of the opening was observed at failure in the specimens with a low amount of FRP reinforcement around the opening. The shear capacity was reduced by 54% due to the presence of the opening in the deep beam having minimum FRP shear reinforcement without using additional reinforcement around the opening. Providing additional FRP reinforcement around the opening increased the number of cracks around the opening's corners, reduced the crack width, controlled crack propagation, and improved the post-cracking stiffness of the beam. Adding two bars at each side of the opening (i.e., one double-leg vertical stirrup at each vertical side and 2 horizontal bars in each chord above and below the opening) increased the shear capacity by 22%, relative to that of the beam with minimum FRP shear reinforcement only. The use of four additional FRP reinforcing bars at each side of the center of the opening within the D-region (two double-leg vertical stirrups at each side of the center of the opening, one of them was crossed by the opening, and 4 horizontal bars

in each chord above and below the opening) mitigated rupture of the vertical FRP stirrups and improved the shear strength by 56% compared to that of the deep beam without additional reinforcement around the openings. It is noteworthy that the concrete compressive strength of the deep beam with extra four FRP reinforcing bars at each side of the center of the web opening was 20% higher than that of their counterparts. Another study conducted by Arabasi and El-Maaddawy [35] showed that solid deep beams without FRP shear reinforcement exhibited a diagonal splitting mode of failure. The deep beams with openings having diagonal FRP reinforcement in the upper and lower chords exhibited the highest load capacity, whereas those with diagonal FRP reinforcement crossing the upper chord only exhibited the lowest. Placing the diagonal FRP reinforcement in the lower chord rather than in the upper chord was more effective in improving the shear capacity of FRP-reinforced deep beams with web openings [35]. It is worth mentioning that that the focus of the study by Arabasi and El-Maaddawy [35] was to examine the validity of different strut-and-tie modeling design options, which required concentration of reinforcement in specific locations to act as ties without providing minimum shear reinforcement in the shear span. Despite the interesting findings and useful information offered by the study conducted by Arabasi and El-Maaddawy [35], the absence of minimum FRP shear reinforcement is impractical and not in compliance with requirements of international codes and standards (e.g., CSA S806 [6] and ACI 440.1R [7]).

1.5 Research Needs

Previous studies highlighted the lack of knowledge on the shear behavior of FRP-reinforced concrete deep beams with a web opening in the shear span. The interaction between the opening size, opening location, concrete strength, and configuration of the web reinforcement in FRP-reinforced deep beams was not investigated. This study aims to fill this gap through numerical analysis. Simulation models were developed and validated against published experimental data. A parametric study was conducted to investigate the interaction between the parameters. Refined analytical formulas were developed to assist practitioners in predicting the shear capacity of FRP-reinforced deep beams with and without a web opening.

8

Chapter 2: Methods

2.1 Research Design

This research examined the behavior of GFRP-reinforced concrete beams with and without web openings through numerical analysis. Activities of the project included development of simulation models, verification of the models' predictions, parametric study, and development of simplified, yet accurate, analytical formulas for shear strength prediction of GFRP-reinforced concrete beams with and without web openings. The analytical formulas were based on regression analysis of the numerical results. An overview of the research design is provided in Figure 2.1.

Model Development	Model Validation	Parametric Study	Analytical formula
• 3D simulation models • Realistic material laws • Benchmark solid beam • Deep beams with openings	• Deflection response • Shear strength • Crack pattern • GFRP strains and stresses	• Concrete strength • Shear span-to-depth ratio • Opening size • Opening location	• Previous formulas • Regression analysis • Modification and calibration • Validation

Figure 2.1: Overview of the research design

2.2 Model Development

Three-dimensional (3D) numerical models were developed for four large-scale RC deep beams tested previously by other researchers [34]. A photograph of a typical large-scale GFRP-reinforced deep beam with openings during testing by Frappier et al. [34] is shown in Figure 2.2. Details of these large-scale deep beam specimens are given in Table 2.1 [34]. The concrete cylinder compressive strength (f'_c) was 37 MPa, except for the model with 4 extra vertical and horizontal reinforcement where its f'_c was 45 MPa, whereas properties of the GFRP bars are given in Table 2.2. The numerical models were developed using ATENA® software [36].

Figure 2.2: A typical deep beam with cutouts during testing [34]

Table 2.1: Data of the tested large-scale deep beam specimens [34]

Model	Cross Section	a/h	Flexural Bars [1]	Opening Size (mm)	Crack Control Reinforcement [1,2]		Extra Reinforcement Around Openings [1,2]	
					Vertical Bar Size	Horizontal Bar Size	Vertical Bar Size	Horizontal Bar Size
Solid	300 × 1200	1.0	8 No. 25	-	No. 12	No. 16	-	-
With Opening	300 × 1200	1.0	8 No. 25	340 × 304	No. 12	No. 16	-	-
	300 × 1200	1.0	8 No. 25	340 × 304	No. 12	No. 16	2 No. 12	2 No. 12
	300 × 1200	1.0	8 No. 25	340 × 304	No. 12	No. 16	4 No. 12	4 No. 12

[1] No. 25 = 25 mm diameter bars, No. 16 = 16 mm diameter bars, and No. 12 = 12 mm diameter bars.

[2] Spacing between FRP web reinforcing bars = 200 mm.

Table 2.2: Properties of GFRP bars [34]

Property	No. 12 [1]	No. 16 [1]	No. 25 [1]
Area (mm^2)	127	198	507
Tensile Strength (f_{fu}) (MPa)	1019 (459) [2]	1184	1000
Elastic Modulus (E_f) (GPa)	50.0	62.6	66.4

[1] No. 12 = 12 mm diameter bars, No. 16 = 16 mm diameter bars, and No. 25 = 25 mm diameter bars.

[2] Value between parentheses represents the strength at a bent portion [34].

2.2.1 Geometry and Properties of Materials

The deep beam models had dimensions of 300 × 1200 × 5000 mm, effective length of 3000 mm, and a shear span-to-depth ratio (*a/h*) of 1.0. Four numerical models were initially developed so that their prediction can be verified against the published experimental data [34]. One deep beam model was solid (DB-S), whereas the other three models (DB-O1, DB-O2, and DB-O3) had a web opening in the middle of the shear span with a width (*wₒ*) of 340 mm and height (*hₒ*) of 304 mm, which corresponded to an opening width-to-shear span ratio (*wₒ/a*) of 0.27 and an opening height-to-beam depth ratio (*hₒ/h*) of 0.25. Details of reinforcement of the deep beam models DB-S, DB-O1, DB-O2, and DB-O3 are shown in Figures 2.3, 2.4, 2.5 and 2.6, respectively. The flexural tensile and compressive reinforcements consisted of 8 GFRP bars with a diameter of 25 mm (No. 25) and 2 GFRP bars with a diameter of 16 mm (No. 16), respectively. The effective depth (*d*) of the tensile reinforcement was 1100 mm. The web reinforcement included 12 mm diameter (No. 12) vertical GFRP stirrups and 16 mm diameter (No.16)

10

horizontal GFRP bars. The spacing between the web reinforcement in both directions was 200 mm. The deep beam model DB-O2 had 2 No. 12 extra double-leg GFRP stirrups in the vertical direction (one at each side of the opening), 2 No. 12 extra horizontal GFRP bars above the opening, and 2 No. 12 extra horizontal GFRP bars below the opening. The deep beam model DB-O3 had 4 No. 12 extra double-leg GFRP stirrups in the vertical direction (one at each side of the opening and two crossed by the opening), 4 No. 12 extra horizontal GFRP bars above the opening, and 4 No. 12 extra horizontal GFRP bars below the opening.
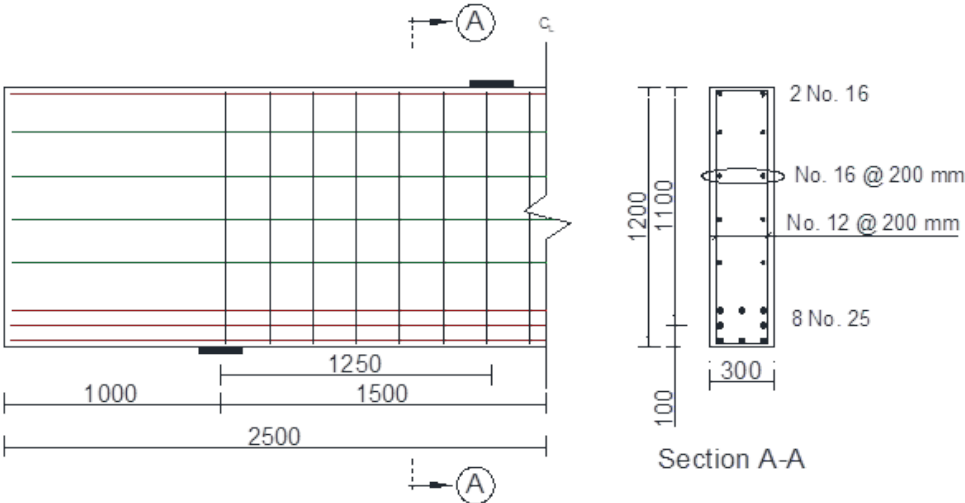
Figure 2.3: Details of DB-S (Dimensions are in mm)
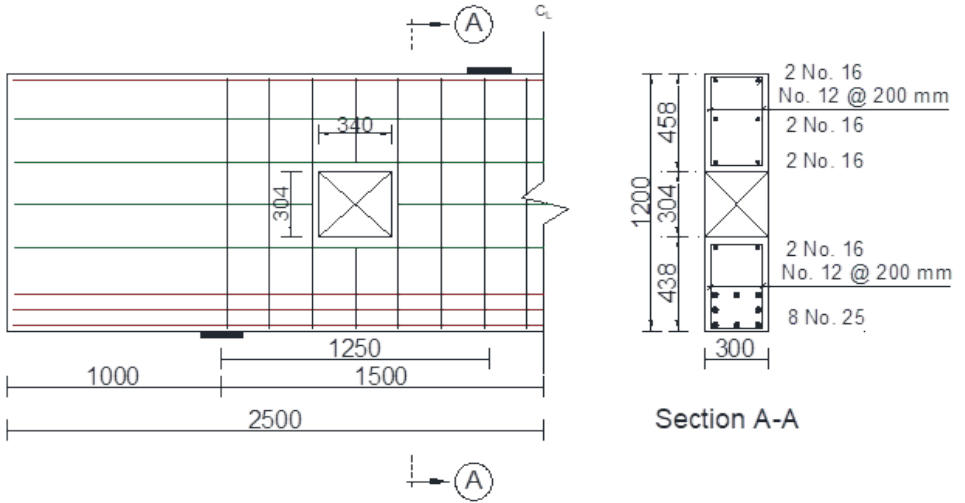
Figure 2.4: Details of DB-O1 (Dimensions are in mm)
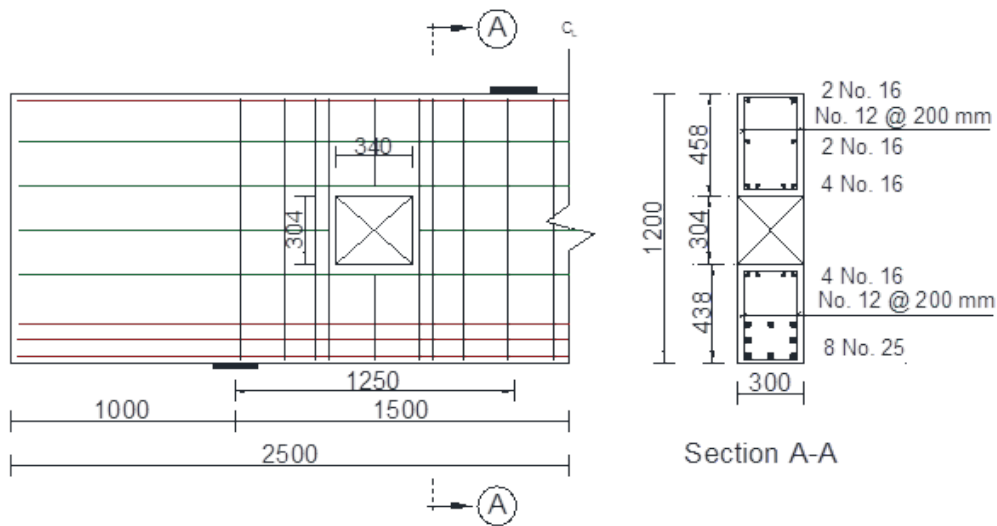
Figure 2.5: Details of DB-O2 (Dimensions are in mm)
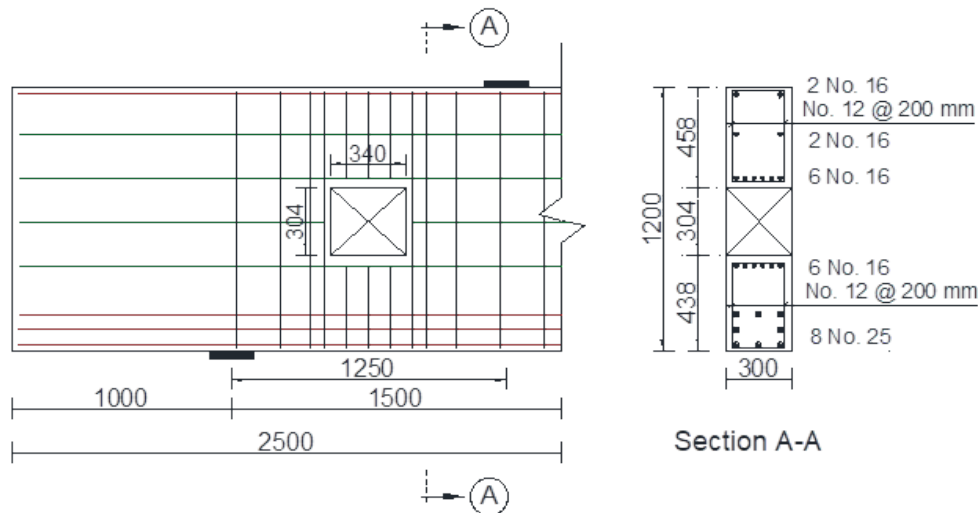
Figure 2.6: Details of DB-O3 (Dimensions are in mm)

2.2.2 Material Constitutive Laws

The nonlinear compressive behavior of the concrete starts at a stress value of f'_{co} = $2.1f_t$, where f_t = concrete tensile strength [36]. The value of f_t is generated automatically by the software, based on the concrete compressive strength. A nonlinear function controls the relationship between the compressive stress (σ_c) in the hardening phase and the plastic strain (ε_p), as shown in Figure 2.7a. The value of the plastic strain at peak (ε_{cp}) is generated automatically by the software, based on the concrete compressive strength. The compressive stress descends linearly in the post-peak phase as

a function of the compressive displacement (w_c) through the length scale L_c, as shown in Figure 2.7b [36]. The complete release of stress is reached at a compressive displacement (w_d) of 0.5 mm [36]. An exponential function controls the softening behavior of the concrete in tension, where tensile stress (σ_t) is linked to the crack opening displacement (w_t) through the length scale L_t, as shown in Figure 2.7c [36]. The crack opening displacement at zero stress (w_{tc}) is generated by the software based on f_t and G_f. Input data of the concrete used in the analysis are given in Table 2.3 based on built-in equations in the software [36]. The vertical stirrups were divided into two U-shape segments (upper and lower) in addition to straight segments for the remaining parts of the stirrup legs. Straight GFRP bars were modeled as linear-elastic, however, the vertical GFRP stirrups were modeled as multilinear with a different tensile strength at the bent portions, as shown in Figure 2.8a. The U-shape segments (upper and lower) were modelled with a tensile strength of 459 MPa, while the straight segments were modelled with a tensile strength of 1019 MPa as per the published experimental data [34]. The stress in the longitudinal, horizontal GFRP web reinforcement, and straight segments of the vertical stirrups was checked at the ultimate load to ensure that it didn't exceed the tensile strengths of straight GFRP bars. Figures 2.8b and 2.8c show the tensile stress-strain response of the straight and U-shaped segments of GFRP bars, respectively, where E_f, f_f, ε_f, f_{fu}, and ε_{fu} refer to the elastic modulus, stress, strain, ultimate strength, and ultimate strain of GFRP bars, respectively. The steel plates (200 × 30 mm) placed at the load and support points to mitigate concentration of stresses at these locations were modeled as linear-elastic.
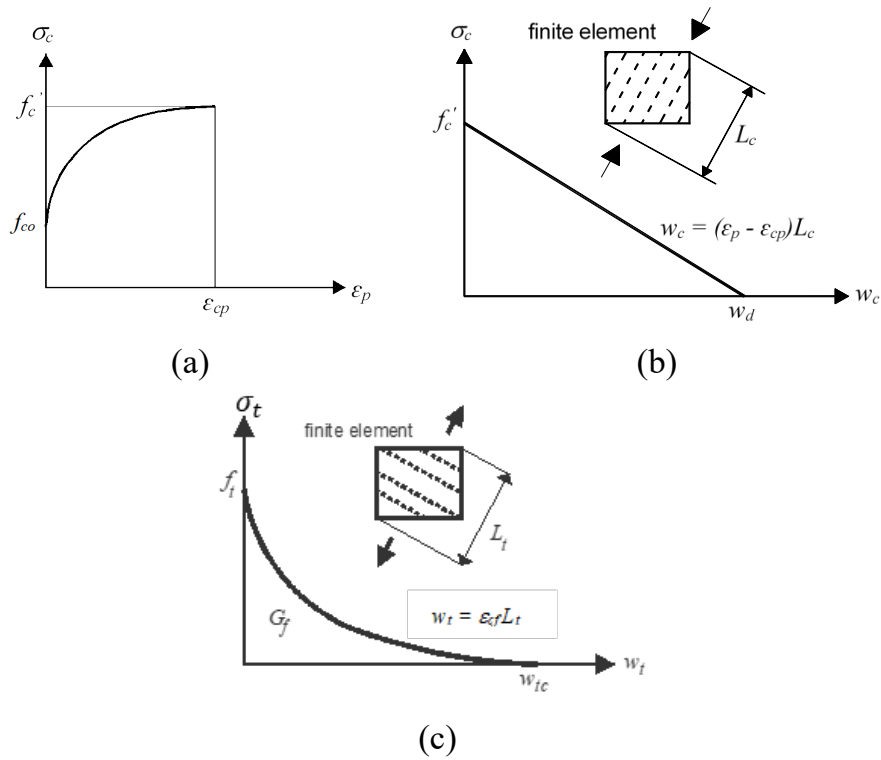
Figure 2.7: Concrete hardening-softening laws: (a) compressive hardening; (b) compressive softening; (c) tensile softening
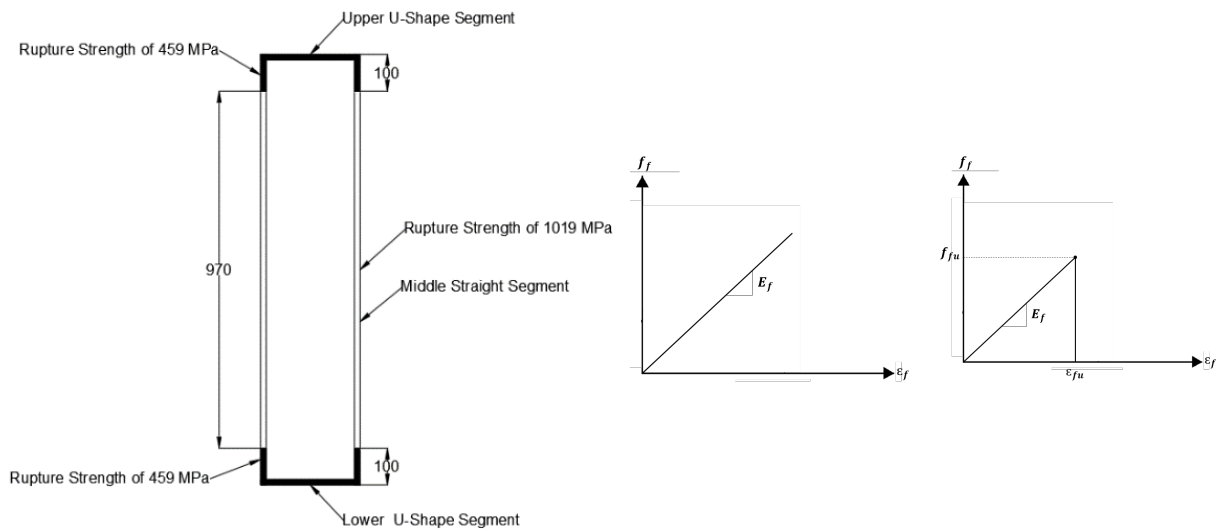
Figure 2.8: GFRP material models: (a) segments of the vertical stirrups (Dimensions are in mm); (b) tensile stress-strain response of straight GFRP bars; (c) tensile stress-strain response of U-shaped GFRP segments

14

Table 2.3: Input data for concrete properties [36]

Parameter	Description	Equation	Value	Unit
f_c'	Compressive strength	N/A	37.00 (45.00) [1]	MPa
E_c	Elastic modulus	$21500 \times \left(\dfrac{f_c'}{10}\right)^{1/3}$	33254 (35496) [1]	MPa
μ	Poisson's ratio	Default value 0.2	0.2	N/A
f_t	Tensile strength	$f_t = 0.3 f_{ck}{}^{2/3}$ $f_{ck} = f_c' - 8$	2.83 (3.33) [1]	MPa
G_F	Specific fracture energy	$G_F = 0.000025 f_t$	70.75 (83.25) [1]	N/m
ε_{cp}	Plastic concrete strain at compressive strength	f_c'/E_c	0.0011 (0.0012) [1]	N/A
f_{co}	Onset of non-linear behavior in compression	$2.1 f_t$	5.94 (7.00) [1]	MPa
w_d	Critical compressive displacement	-	0.50	Mm

[1] Values between parenthesis are for DB-O3

2.2.3 Element Types and Boundary Conditions

Solid 3D brick elements were used to model the concrete and the steel plates. The GFRP bars were modeled as one-dimensional discrete elements embedded into the concrete brick-elements. A mesh sensitivity analysis was conducted to determine the optimum mesh size, which was found to be 50 mm. To take advantage of the plane of symmetry at the midspan and reduce the overall computational time, only half-beam models were created. To restrict the movement in the vertical and transverse directions, a line support is placed at the middle of the bottom surface of the support steel plate. The surface of the plane of symmetry is restrained from movement in the longitudinal direction through surface supports. A displacement-controlled applied load was induced at the midpoint of the top steel plate at a rate of 0.1 mm per step. Monitoring points were installed to measure the load at the midpoint of the top surface of the load plate, the deflection at the midspan, and the strains in some locations at the GFRP bars. The

standard Newton–Raphson iterative solution method was adopted. The iterations should satisfy a tolerance limit of convergence criteria related to compatibility of displacements, equilibrium of forces, and balance of energy. Figure 2.9a shows a typical numerical model for a solid deep beam, while Figure 2.9b shows a typical numerical model for a beam with a web opening in the middle of the shear span. General 3D views showing the flexural and web reinforcements of the numerical models are provided in Figure 2.10.
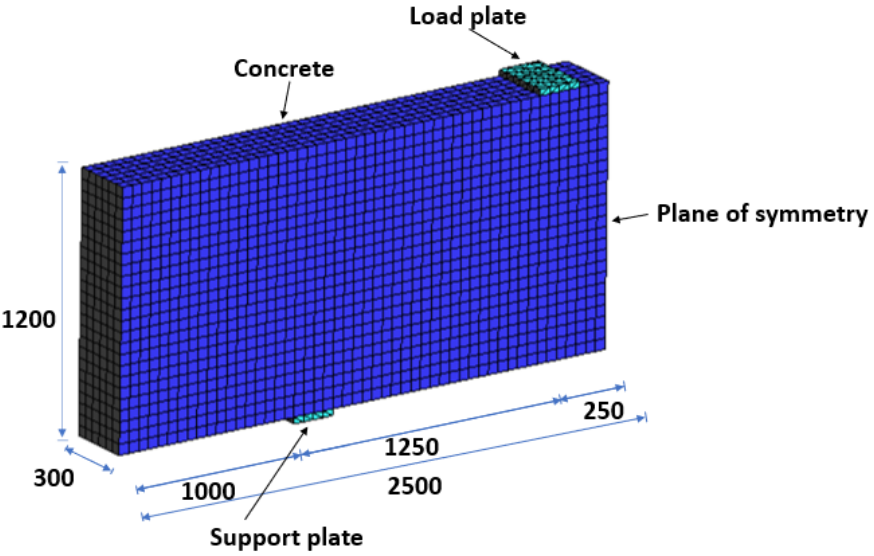
(a)
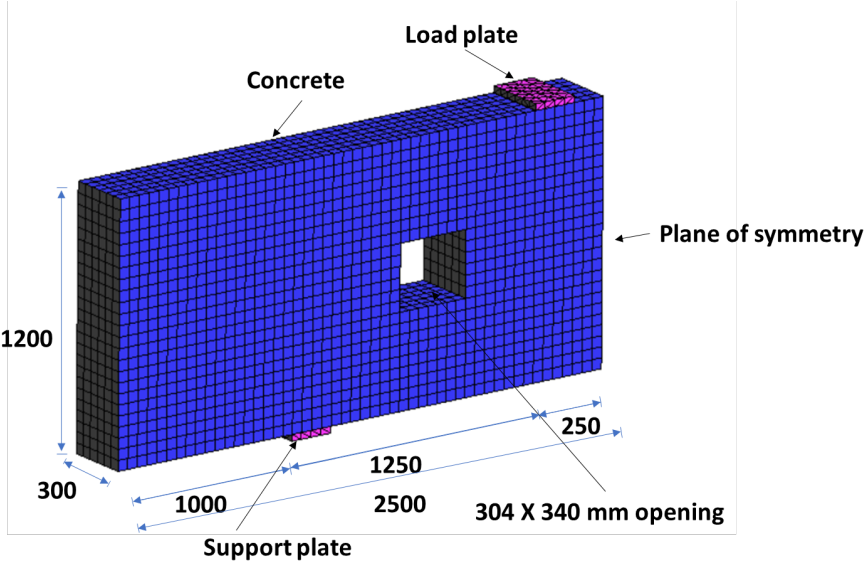
(b)

Figure 2.9: Numerical models (Dimensions are in mm): (a) DB-S; (b) DB-O
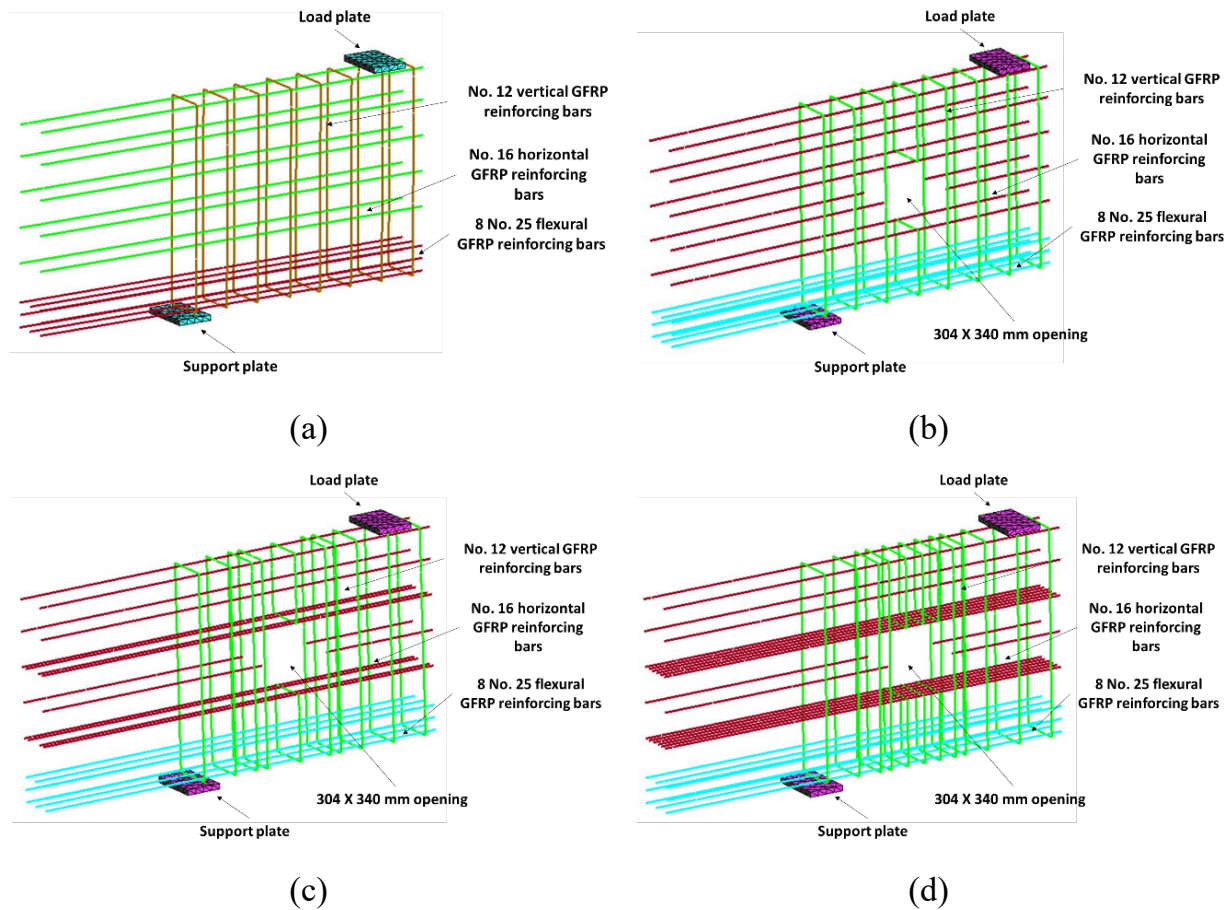
Figure 2.10: Flexural and web reinforcements: (a) DB-S; (b) DB-O1; (c) DB-O2; (d) DB-O3

2.3 Parametric Study

Following validation of the developed numerical models, a parametric study was conducted to study the effect of key parameters on the shear behavior of GFRP-reinforced deep beams with and without a web opening. The parametric study was divided into four phases. The first phase focused on the analysis of solid deep beams without web reinforcement. The second phase focused on the analysis of solid deep beams with web reinforcement. The third phase focused on the analysis of deep beams with a web opening in the middle of the shear span having different sizes. The fourth phase focused on the analysis of deep beams with a web opening at different locations with respect to the natural load path within the shear span. Based on regression analysis of numerical results, refined simplified analytical formulas were introduced for shear strength prediction of GFRP-reinforced concrete deep beams with and without a web opening.

2.3.1 Parameters of Solid Deep Beam Models without Web Reinforcement

Parameters of the solid deep beam models without web reinforcement are summarized in Table 2.4. The variables were the concrete compressive strength (f_c') and *a/h*. The *a/h* value was either 1.0 or 1.5. Values of f_c' were 28, 37, and 50 MPa, representing low (L), moderate (M), and high (H) concrete compressive strengths, respectively. Figures 2.11a and 2.11b show details of reinforcement of the numerical models of this group with *a/h* of 1.0 and 1.5, respectively.

Table 2.4: Parameters of solid deep beams without web reinforcements

a/h	f_c' **(MPa)**	**Model designation**
1.0 (*a* = 1250 mm)	28	SDB-1.0-L
	37	SDB-1.0-M
	50	SDB-1.0-H
1.5 (*a* = 1800 mm)	28	SDB-1.5-L
	37	SDB-1.5-M
	50	SDB-1.5-H
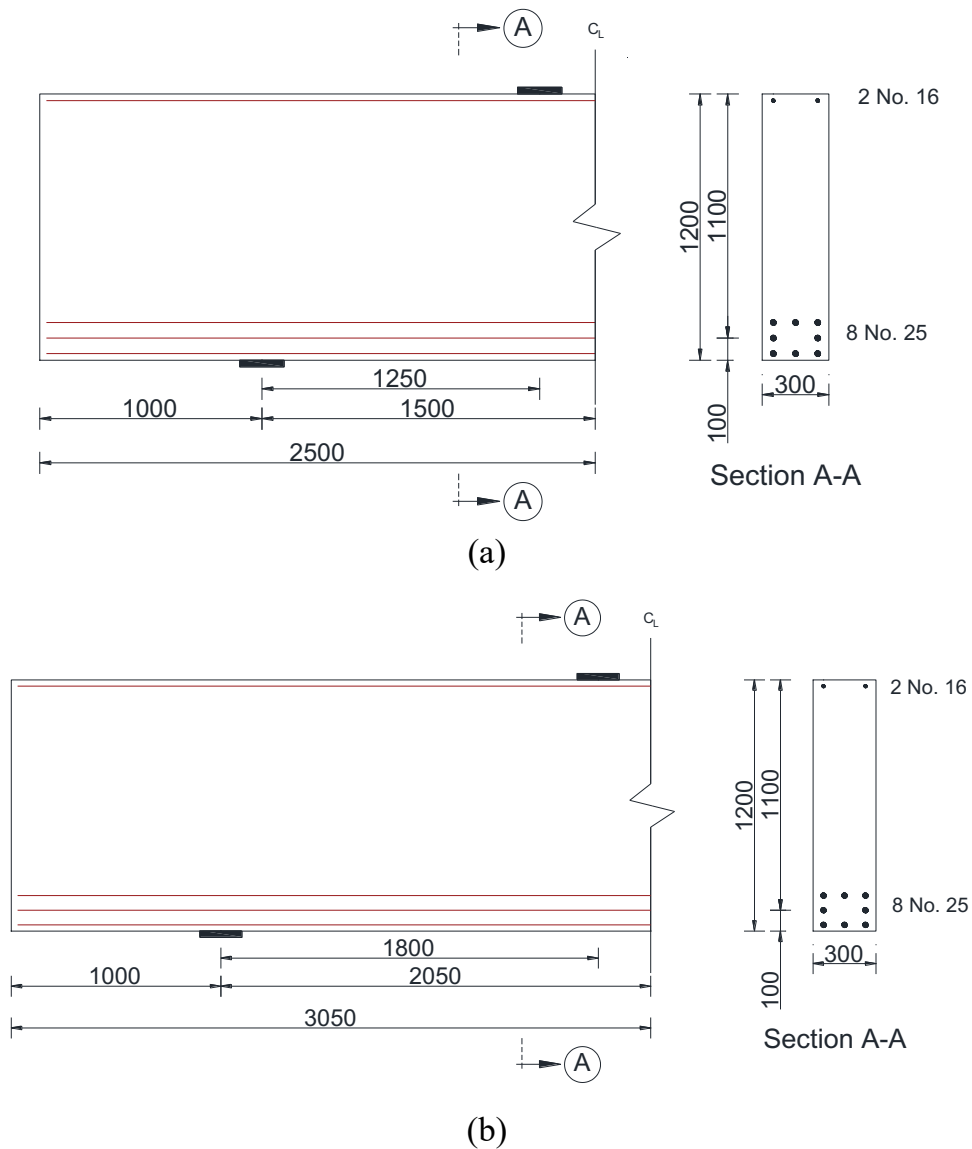
Figure 2.11: Details of solid deep beams without web reinforcement (Dimensions are in mm): (a) *a/h* =1.0; (b) *a/h* = 1.5

2.3.2 Parameters of Solid Deep Beam Models with Web Reinforcement

Parameters of the solid deep beam models with web reinforcement are summarized in Table 2.5. The variables were the concrete compressive strength (f_c'), value of *a/h*, and spacing between the web reinforcement (*s*). The beam models had *a/h* value of either 1.0 or 1.5. Values of f_c' were 28, 37, and 50 MPa representing low (L), moderate (M), and high (H) concrete strengths, respectively. The spacings between the web reinforcement were 100 and 200 mm. Figures 2.12 and 2.13 show details of

reinforcement of the numerical models of this group with *a/h* of 1.0 and 1.5, respectively.

Table 2.5: Parameters of the solid deep beam models with web reinforcement

a/h	f_c'(MPa)	Spacing between Web GFRP bars, (s) (mm)	Model Designation
1.0 (a = 1250 mm)	28	100	SDB-1.0-L100
		200	SDB-1.0-L200
	37	100	SDB-1.0-M100
		200	SDB-1.0-M200
	50	100	SDB-1.0-H100
		200	SDB-1.0-H200
1.5 (a = 1800 mm)	28	100	SDB-1.5-L100
		200	SDB-1.5-L200
	37	100	SDB-1.5-M100
		200	SDB-1.5-M200
	50	100	SDB-1.5-H100
		200	SDB-1.5-H200
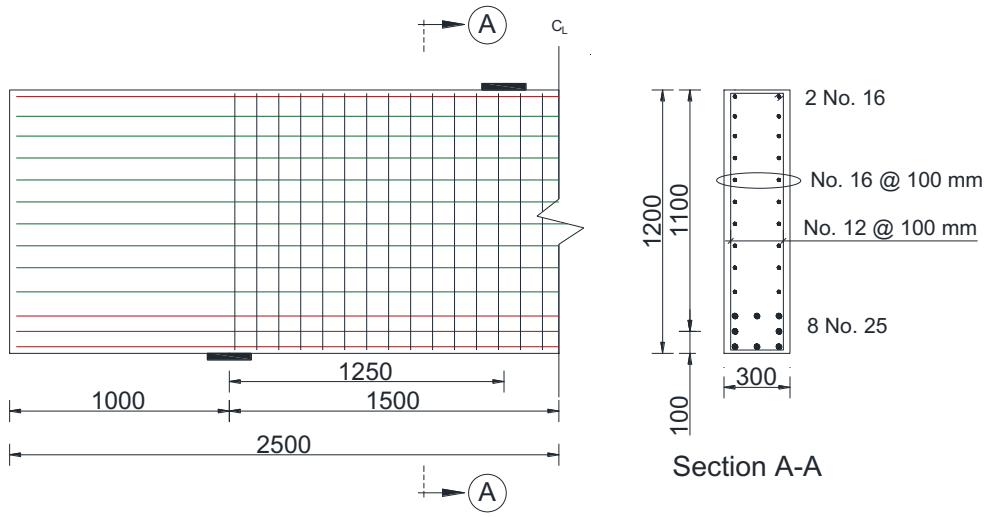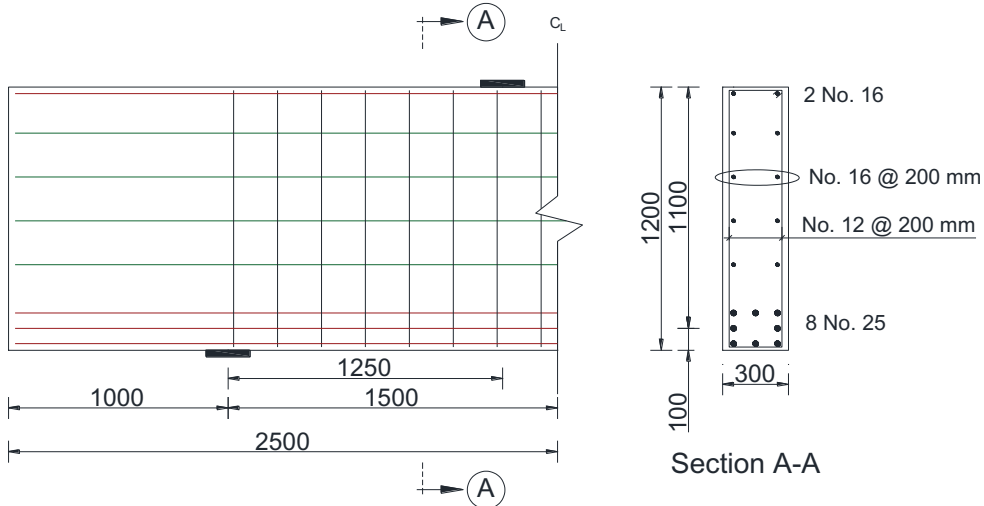
Figure 2.12: Details of solid deep beam models with web reinforcement and *a/h* = 1.0 (Dimensions are in mm): (a) *s* = 100 mm; (b) *s* = 200 mm
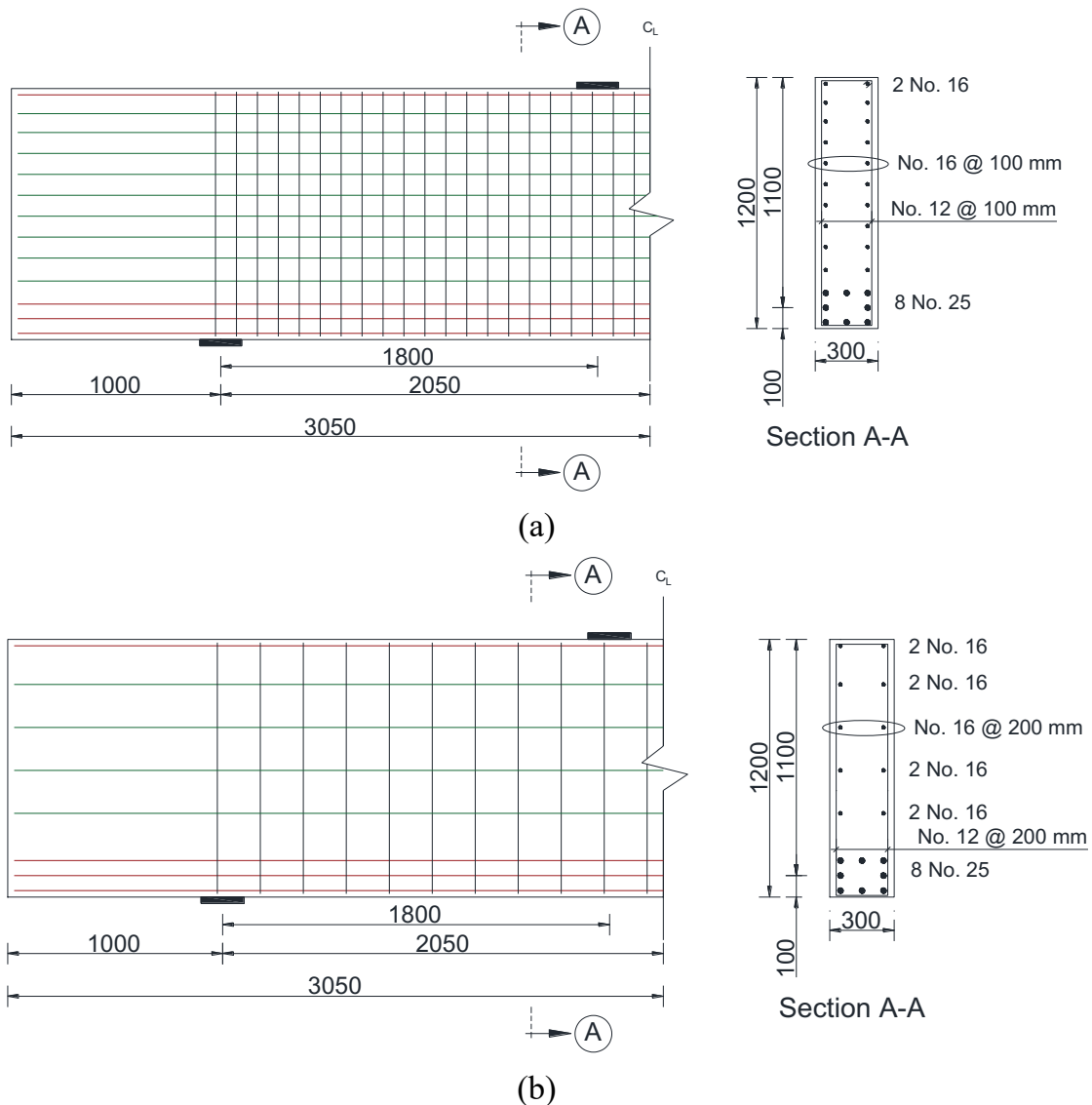
Figure 2.13: Details of solid deep beam models with web reinforcement and *a/h* = 1.5 (Dimensions are in mm): (a) *s* = 100 mm; (b) *s* = 200 mm

2.3.3 Parameters of Deep Beam Models Containing a Web Opening

2.3.3.1 Parameters of Deep Beam Models with Different Opening Sizes

Parameters of the deep beam models with different opening sizes are summarized in Table 2.6. The deep beam models of this group had the same f_c' value of 37 MPa, a/h value of 1.0, and a web opening installed in the middle of the shear span. The variables included values of w_o/a (0.16, 0.27, and 0.32) and values of h_o/h (0.17, 0.25, and 0.33). Figures 2.14 to 2.16 show details of reinforcement of the numerical models of this group with different opening sizes.

Table 2.6: Parameters of deep beam models with different opening sizes

| a/h | f_c' | Opening Size (mm) | | Model Designation |
		w_o[1]	h_o[2]	
1.0 (a = 1250 mm)	37	200	200	DB-W0.16-H0.17
		200	304	DB-W0.16-H0.25
		200	400	DB-W0.16-H0.33
		340	200	DB-W0.27-H0.17
		340	304	DB-W0.27-H0.25
		340	400	DB-W0.27-H0.33
		400	200	DB-W0.32-H0.17
		400	304	DB-W0.32-H0.25
		400	400	DB-W0.32-H0.33

[1] w_o values of 200, 340, and 400 mm correspond to w_o/a values of 0.16, 0.27, and 0.32, respectively.

[2] h_o values of 200, 304, and 400 mm correspond to h_o/h values of 0.17, 0.25, and 0.33, respectively.
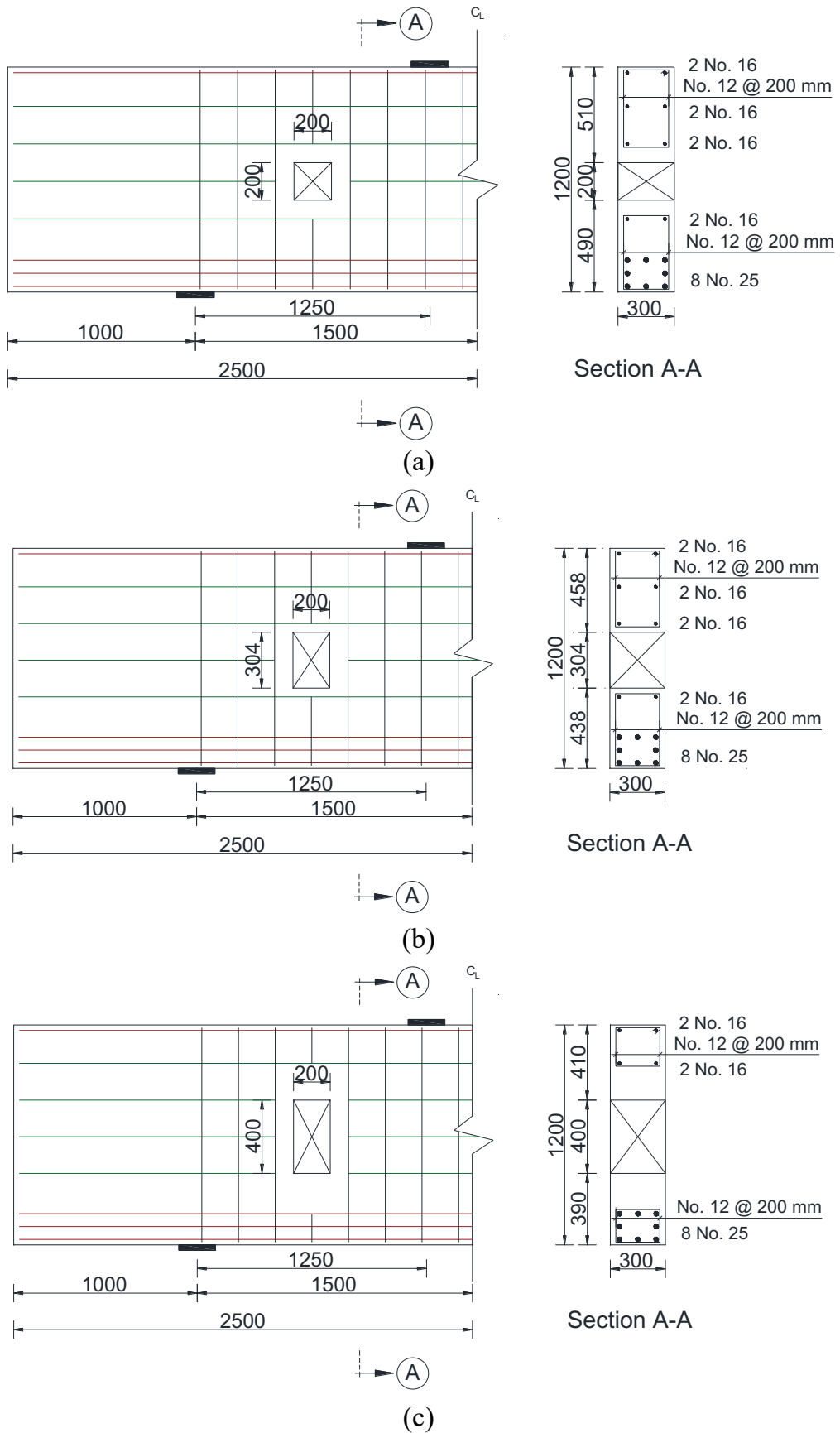
Figure 2.14: Details of deep beam models with $w_o/a = 0.16$ (Dimensions are in mm): (a) $h_o/h = 0.17$; (b) $h_o/h = 0.25$; (c) $h_o/h = 0.33$
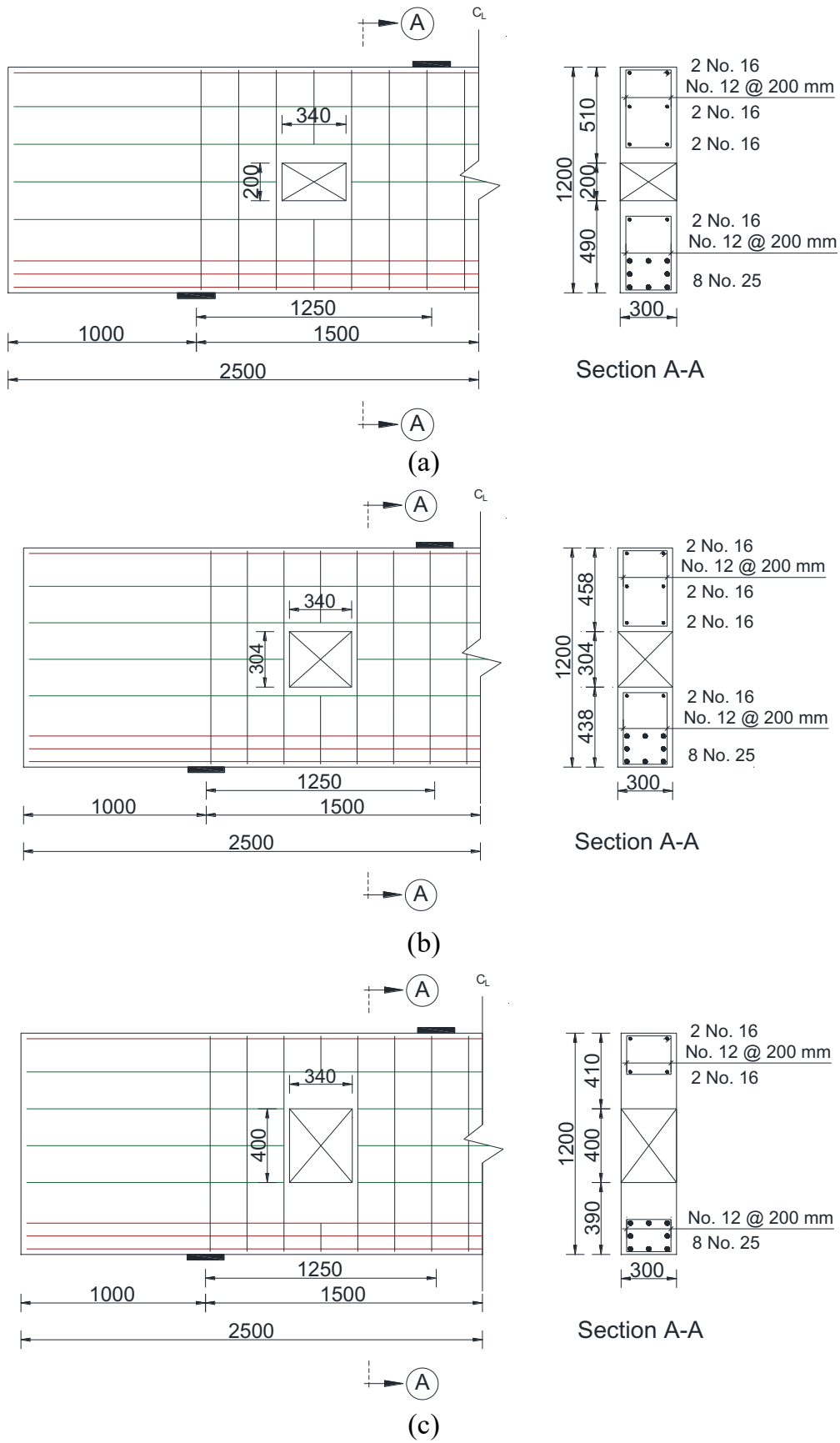
Figure 2.15: Details of deep beam models with $w_o/a = 0.27$ (Dimensions are in mm): (a) $h_o/h = 0.17$; (b) $h_o/h = 0.25$; (c) $h_o/h = 0.33$
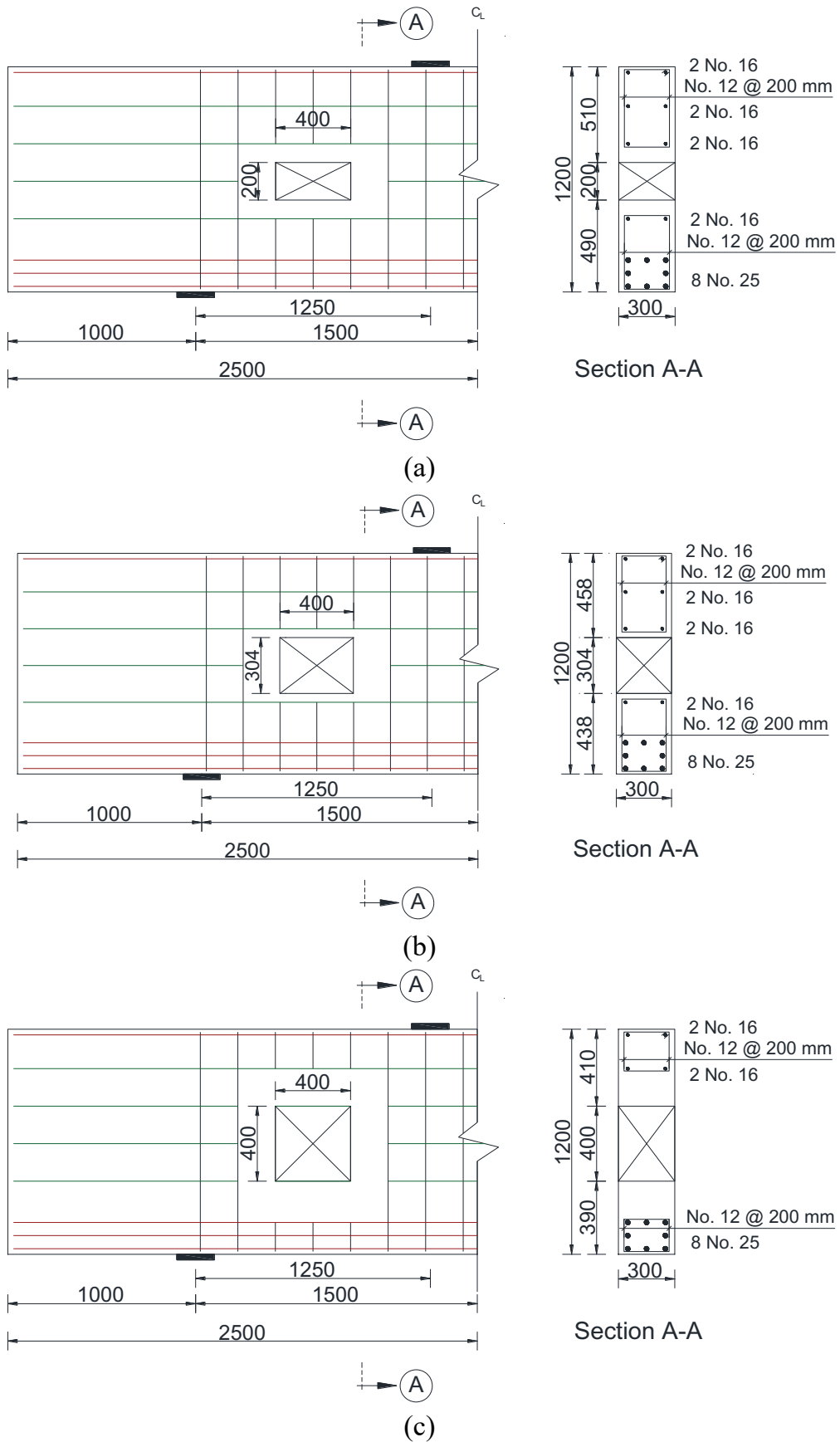
Figure 2.16: Details of deep beam models with $w_o/a = 0.32$ (Dimensions are in mm): (a) $h_o/h = 0.17$; (b) $h_o/h = 0.25$; (c) $h_o/h = 0.33$

2.3.3.2 Parameters of Deep Beam Models with Different Opening Locations

Parameters of the deep beam models with different opening locations are summarized in Table 2.7. The deep beam models of this group had the same f_c' value of 37 MPa, a/h value of 1.0, and a web opening size of $w_o = 340$ mm and $h_o = 304$ mm (i.e., $w_o/a = 0.27$ and $h_o/h = 0.25$). The primary variable of this group was the location of the web opening. The center of the web opening was located at a distance x_o from the face of the support plate and y_o from the bottom soffit of the beam model. The location of the center of the opening in the horizontal and vertical directions were normalized to the clear shear span (X_c) and beam depth (h), respectively. Values of the term x_o/X_c were 0.25, 0.50, and 0.75, whereas those of the term y_o/h were 0.33, 0.50, and 0.75. Figures 2.17 to 2.19 show details of reinforcement for the beam models of this group.

Table 2.7: Parameters of deep beam models with different opening locations

a/h	f_c'	Opening Location (mm)		Model Designation
		$x_o{}^1$	$y_o{}^2$	
1.0 (a = 1250 mm)	37	262.5	400	DB-X0.25-Y0.33
			590	DB-X0.25-Y0.50
			900	DB-X0.25-Y0.75
		525	400	DB-X0.50-Y0.33
			590	DB-X0.50-Y0.50
			900	DB-X0.50-Y0.75
		787.5	400	DB-X0.75-Y0.33
			590	DB-X0.75-Y0.50
			900	DB-X0.75-Y0.75

[1] x_o values of 262.5, 525, and 787.5 mm correspond to x_o/X_c values of 0.25, 0.50, and 0.75, respectively.

[2] y_o values of 400, 590, and 900 mm correspond to y_o/h values of 0.33, 0.50, and 0.75, respectively.

(a)

(b)

(c)
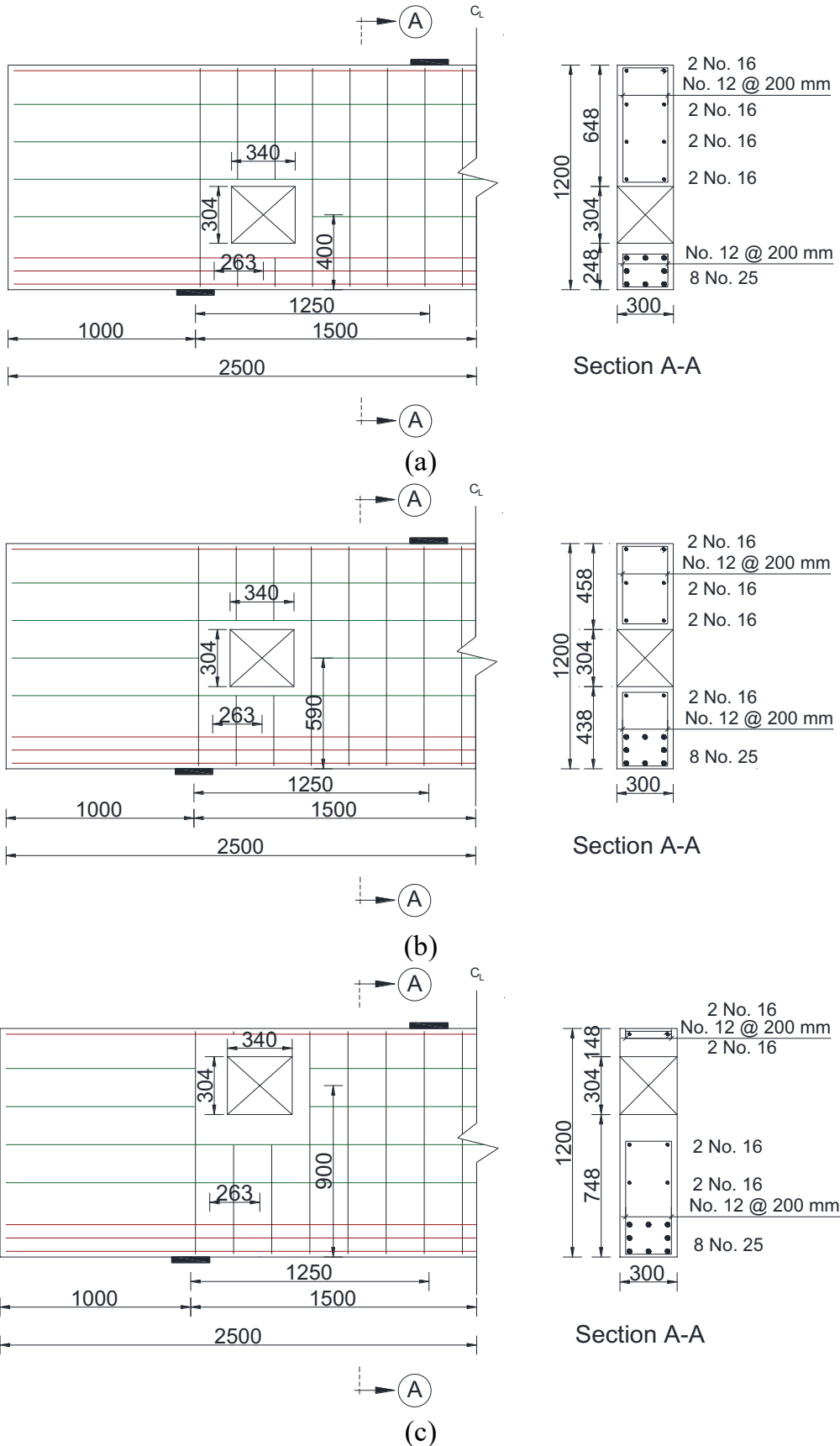
Figure 2.17: Details of deep beam models with $x_o/X_c = 0.25$ (Dimensions are in mm): (a) $y_o/h = 0.33$; (b) $y_o/h = 0.50$; (c) $y_o/h = 0.75$
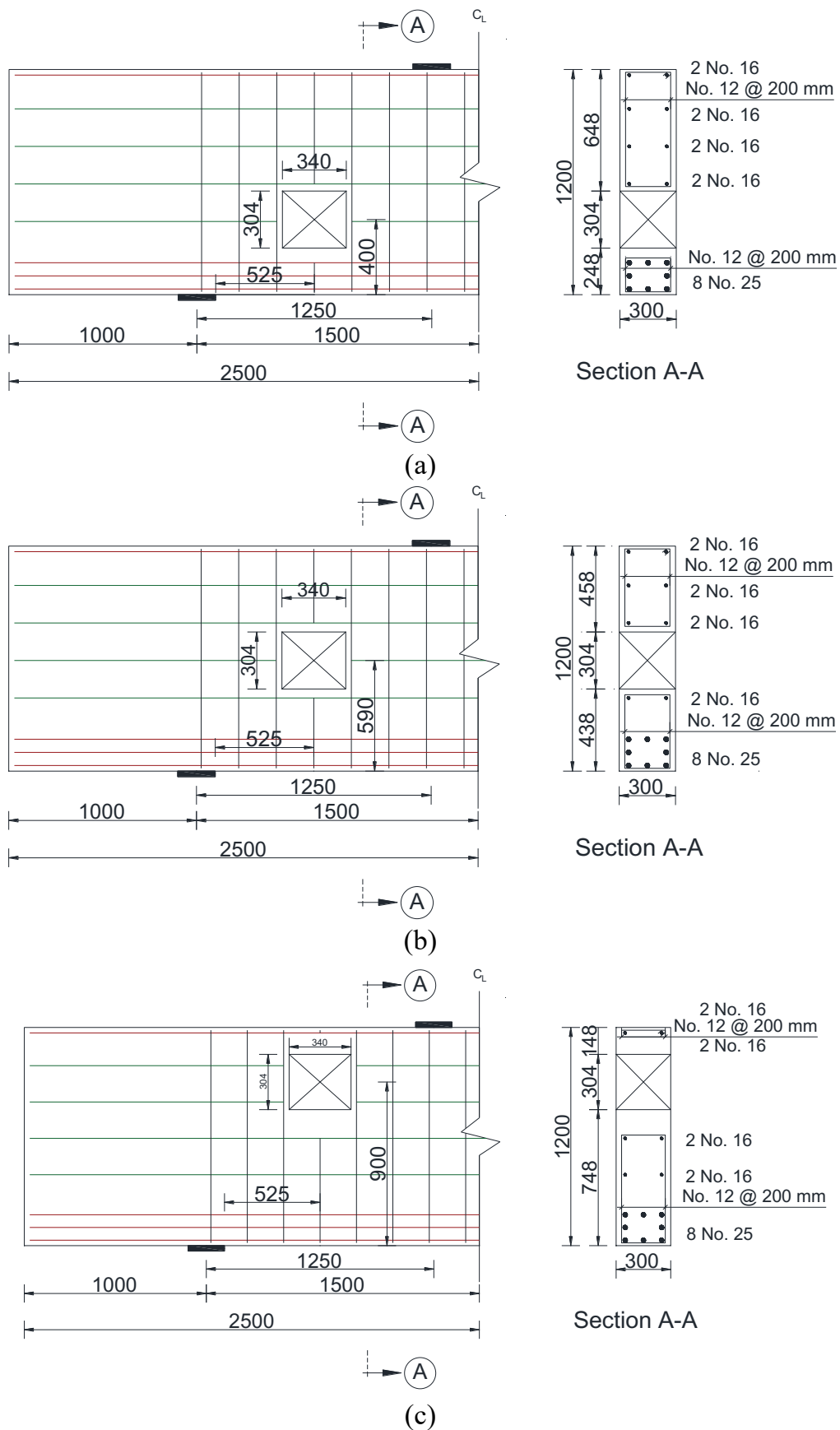
Figure 2.18: Details of deep beam models with $x_o/X_c = 0.50$ (Dimensions are in mm): (a) $y_o/h = 0.33$; (b) $y_o/h = 0.50$; (c) $y_o/h = 0.75$

Figure 2.19: Details of deep beam models with $x_o/X_c = 0.75$ and different opening vertical locations (Dimensions are in mm): (a) $y_o/h = 0.33$; (b) $y_o/h = 0.50$; (c) $y_o/h = 0.75$

30
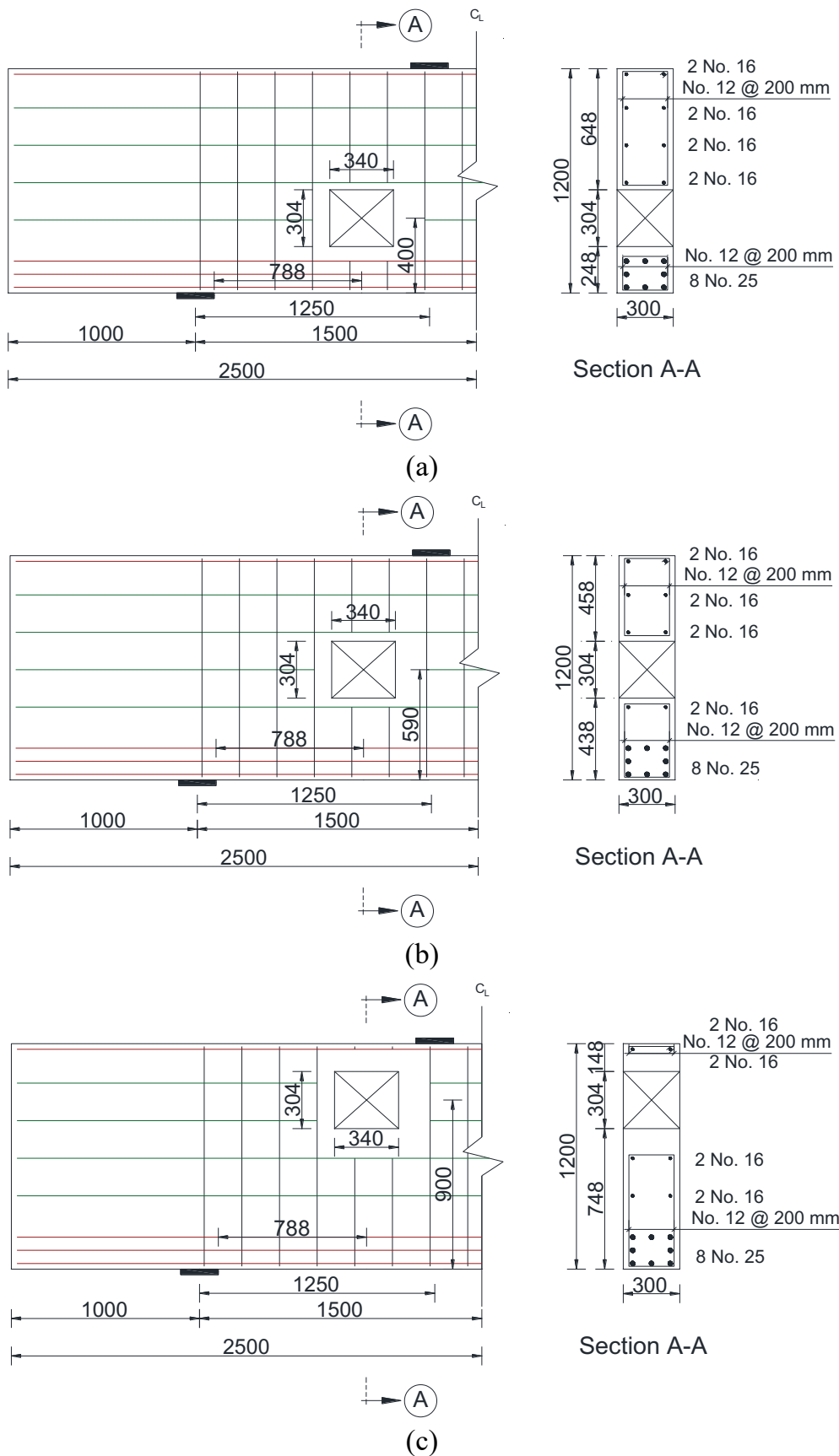
Chapter 3: Model Verification

3.1 Overview

This chapter presents a comparative analysis between predictions of the four simulation models DB-S, DB-O1, DB-O2, and DB-O3 and their experimental results published in the literature [34]. The results in the comparative analysis included the deflection response, ultimate loads, deflection capacity, crack propagation, failure mechanism, and stresses in the GFRP reinforcement.

3.2 Load-Deflection Response

The numerical and experimental load-defection responses of the four beams are given in Figure 3.1. The total load reported experimentally and numerically represents two times the support reaction load. It is evident that the deflection response predicted numerically followed the same trend as that obtained from the tests. The response started by a linear branch until flexural cracks initiated at approximately 500 kN. The initiation of the flexural cracks caused a change in the load-deflection response. The beam models exhibited a quasilinear response in the post-cracking phase due to a progressive development of cracks during loading, which was in alignment with the experimental results. The post-cracking stiffness of the deep beams with openings was lower than that of the solid beam. Another change in slope was observed prior to reaching the ultimate load, probably because of the development of new major cracks. The deep beams DB-O2 and DB-O3 with extra GFRP reinforcement around the opening exhibited an improved behavior relative to that of DB-O1. This behavior was predicted numerically and verified experimentally.

The response of DB-S, DB-O1, DB-O2, and DB-O3 predicted numerically are compared to those obtained from the experiment in Figure 3.2. It is evident that the numerical and experimental deflection responses are in good agreement. There was a deviation between the pre-cracking stiffness predicted numerically and that measured experimentally. This behavior is expected, particularly, for such a large-scale deep beam. The actual deep beams could have had shrinkage cracks due to the large surface area prior to testing, which might have reduced its initial stiffness in the pre-cracking stage. It

is noteworthy that the post-cracking stiffness of all beams predicted numerically almost coincided with that measured experimentally. Table 3.1 presents the numerical and experimental ultimate loads along with the corresponding deflection capacities. The difference between the numerical and experimental ultimate loads was within a 12% error band. The deviation between the deflection capacity predicted numerically and that obtained from the tests did not exceed 15%, except for DB-O3 which showed a deviation of 28% in the deflection capacity. The beam model DB-O3 failed at an ultimate load that was 4% lower than that measured experimentally. Since the numerical and experimental deflection responses had almost the same post-cracking stiffness, the reduction in the ultimate load was accompanied by a reduction in the deflection capacity. Generally, the difference between numerical and experimental results is within the acceptable margin of error.
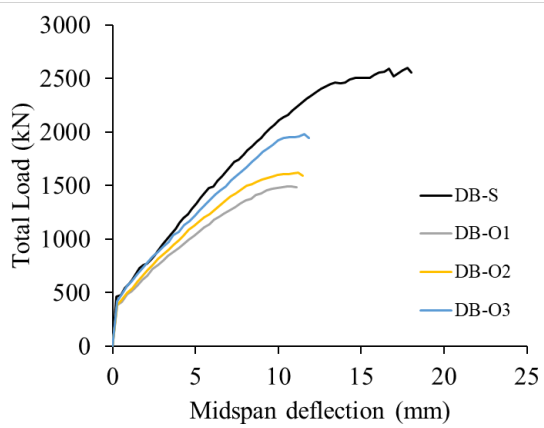
(a)
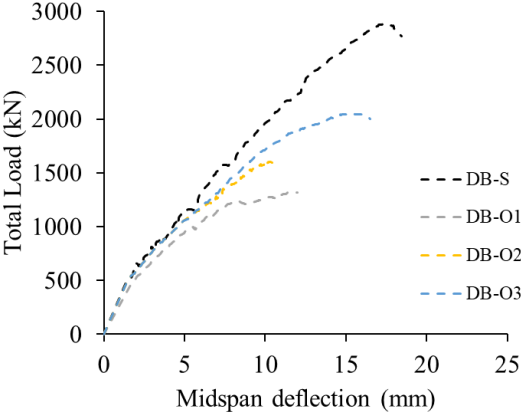
(b)

Figure 3.1: Load-deflection responses: (a) Numerical prediction; (b) Experimental data
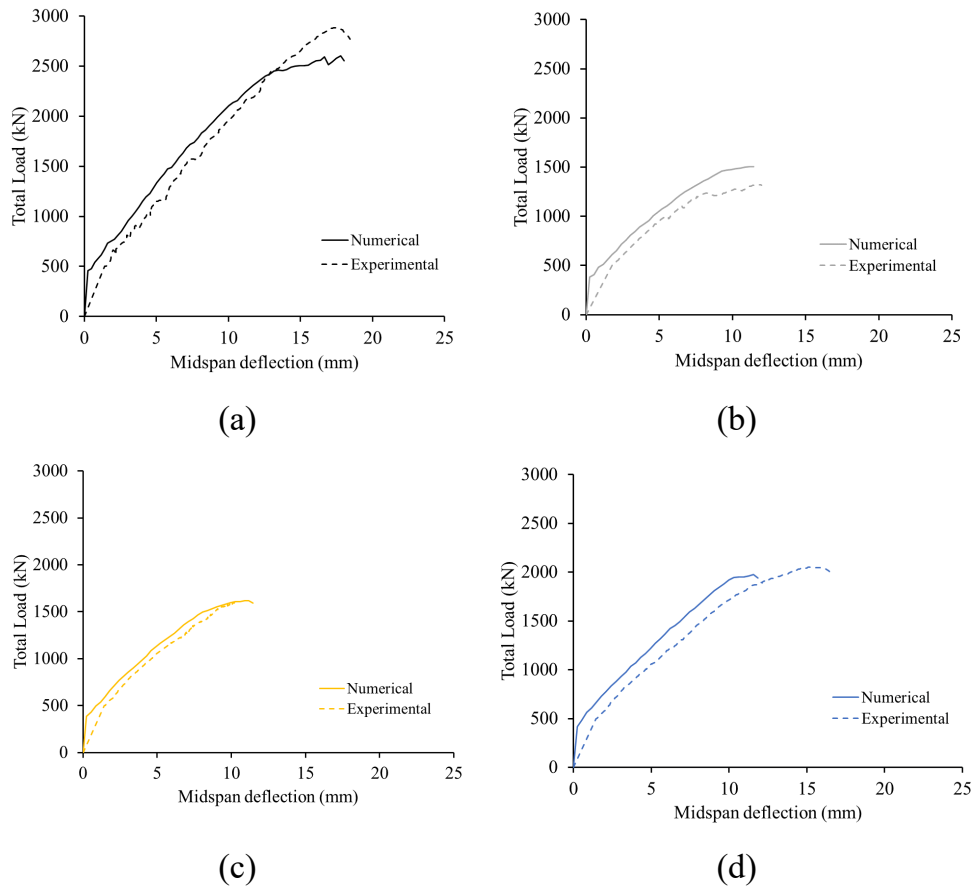
Figure 3.2: Numerical vs. experimental response: (a) DB-S; (b) DB-O1; (c) DB-O2; (d) DB-O3

Table 3.1: Numerical and experimental results

Models	Ultimate Load (KN)			Deflection Capacity (mm)		
	Experimental	Numerical	Error (%) [1]	Experimental	Numerical	Error (%) [1]
DB-S	2904	2601	-10	17.3	17.8	+3
DB-O1	1328	1489	+12	12.7	10.8	+15
DB-O2	1619	1619	0	11.3	11.2	-0.9
DB-O3	2067	1978	-4	16.2	11.6	-28

[1] Error (%)= $\dfrac{\text{Numerical-Experimental}}{\text{Experimental}} \times 100$

3.3 Crack Pattern and Failure Mechanism

The crack patterns predicted numerically at different stages of loading for DB-S are shown in Figure 3.3. The crack pattern obtained from the experiment along with a photograph for DB-S at ultimate are provided in Figure 3.4. The numerical prediction indicated initiation of flexural cracks prior to shear cracks. The published data also indicated initiation of flexural cracks early at 18% of the ultimate load before development of any shear cracks [34]. Diagonal cracks were then formed in the shear span as the load progressed. Additional shear cracks were developed with an increase in the applied load defining the direction of a concrete diagonal strut between the load and support points. Eventually, DB-S failed by crushing of the diagonal concrete strut formed in the shear span. This behavior was predicted numerically and verified experimentally.

(a)

(b)

(c)

(d)
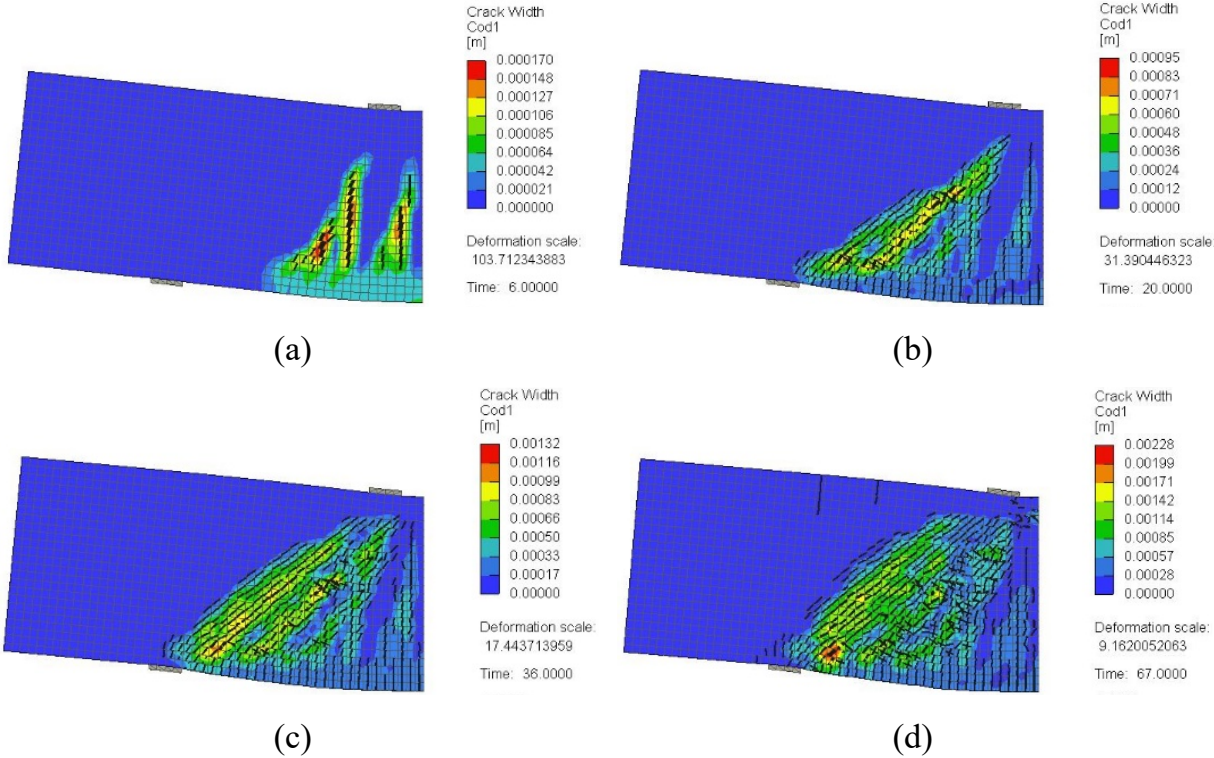
Figure 3.3: Numerical crack pattern of DB-S: (a) at 25% of peak load; (b) at 50% of peak load; (c) at 75% of peak load; (d) at 100% of peak load
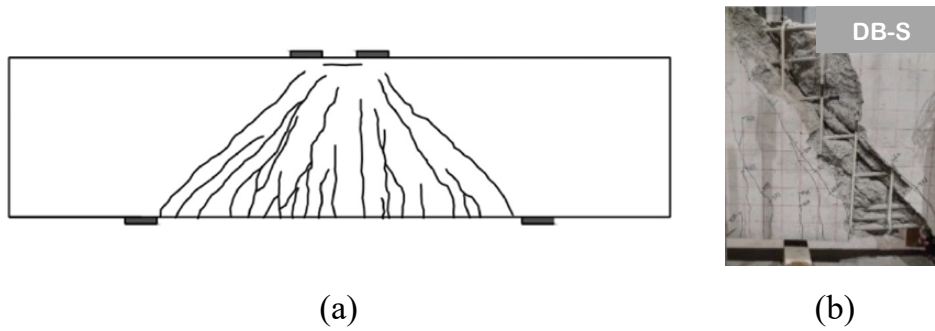
Figure 3.4: Experimental crack pattern of DB-S [34]: (a) schematic; (d) photograph for the right shear span at ultimate

Figure 3.5 shows the crack patterns predicted numerically at different stages of loading for a typical deep beam model with a web opening (DB-O2). Shear cracks initiated first at the opposite corners of the opening closer to the support and load plates. This behavior was in agreement with the published experimental data [34], which indicated early formation of shear cracks at the opening corner at 17 to 24% of the ultimate load. Further increase in load resulted in propagation of these shear cracks toward the load and support plates along with development of flexural cracks. The shear cracks developed earlier at the opening corners were then stabilized and other shear cracks were then developed in the top and bottom chords. Eventually, the beam model with a web opening failed due to formation of two independent major shear cracks developed in the top and bottom chords. The major shear crack causing failure in the top chord connected the edge of the load plate to the top corner of the opening closer to the support plate. The major shear crack causing failure in the bottom chord connected the edge of the support plate and the bottom corner of the opening closer to the load point. The crack patterns at the different stages of loading and the failure mechanism predicted numerically were in good agreement with the sequence of crack propagation and failure mode observed during the experimental tests reported in the literature [34] as shown in Figure 3.6.
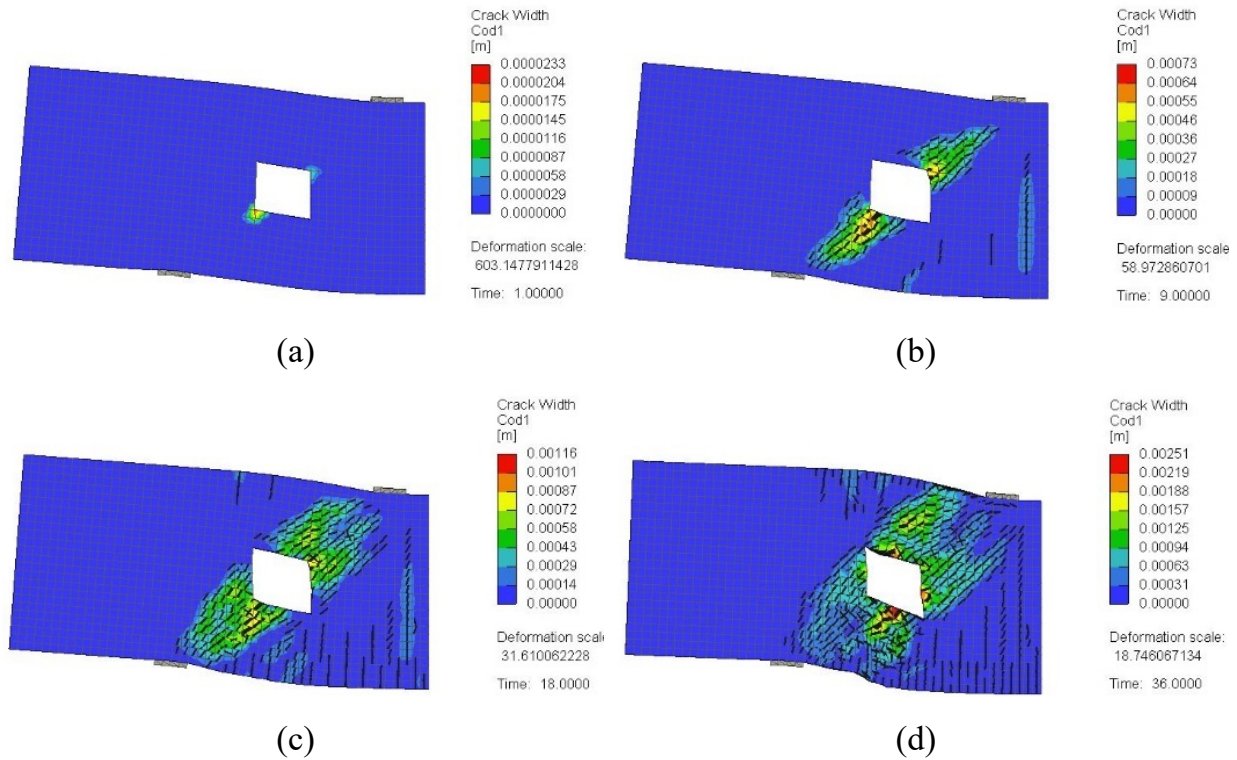
Figure 3.5: Crack pattern for a typical beam model with a web opening (DB-O2): (a) at 25% of peak load; (b) at 50% of peak load; (c) at 75% of peak load; (d) at 100% of peak load
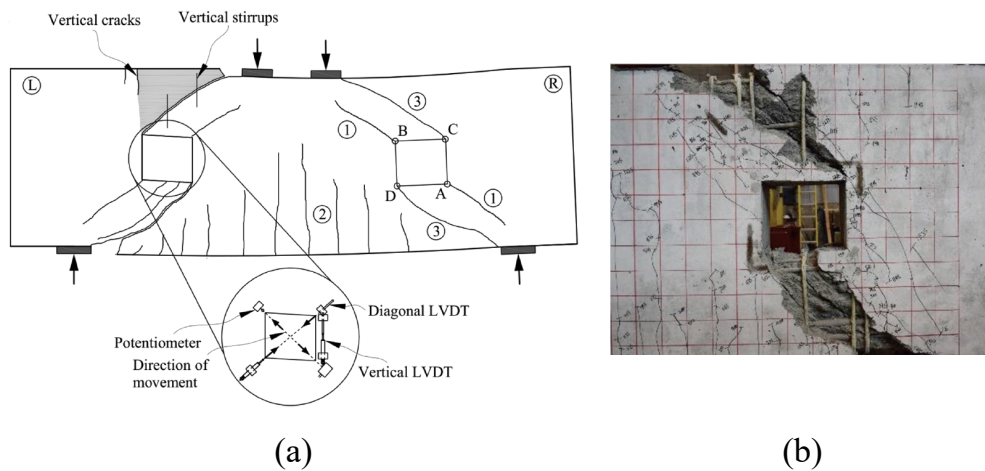
Figure 3.6: Sequence of crack propagation and failure mode of a deep beam with a web opening obtained from the experiment [34]: (a) Schematic; (b) Photograph for the right shear span at ultimate

3.4 GFRP Stresses and Strains

The strains in the web reinforcement were monitored at specific locations along the natural load path of DB-S connecting the load and support points as shown in Figure

36

3.7. The strains predicted numerically are plotted against the load in Figure 3.8. Measured GFRP strain responses at the same locations are shown in Figure 3.9. The numerical results indicated that the vertical and horizontal web reinforcing bars were not strained until shear crack developed in the shear span at a load value of approximately 1200 to 1500 kN. Following shear cracking, the strain increased almost linearly until the ultimate load was reached. The rate of increase in the vertical GFRP stirrups in all monitoring points was almost identical. The strain in the vertical GFRP stirrups predicted numerically at ultimate load was approximately 0.7%. The measured strains in the vertical GFRP stirrups at ultimate load were on average 0.8%. The maxim strain predicted numerically in the horizontal GFRP bars at ultimate load (approx. 0.4%) was lower than that recorded in the vertical stirrups. The strains measured experimentally in the horizontal bars were on average 0.5%. It is noteworthy that the strain predicted numerically in the horizontal GFRP bars closer to the tension face tended to increase at a higher rate than that of the horizontal bars closer to the compression face (Figure 3.8). Experimental measurements shown in Figure 3.9 verified the lower strains in the horizontal GFRP bars closer to the compression face (H4).
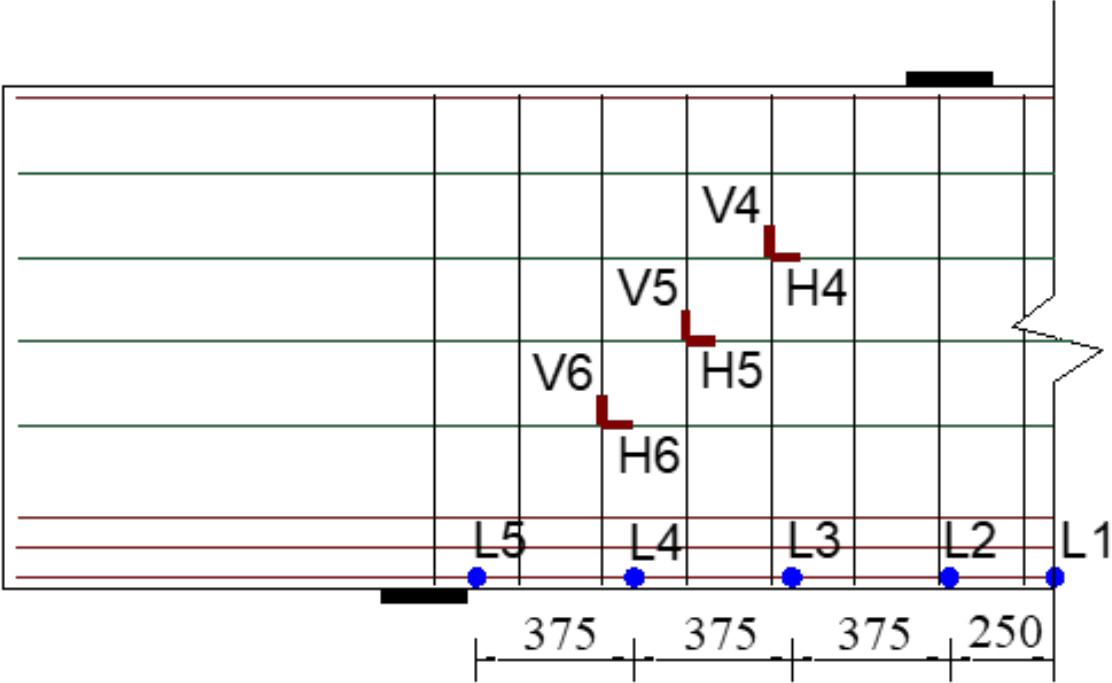
Figure 3.7: Locations of the monitoring points for GFRP strains in DB-S (Dimensions are in mm)
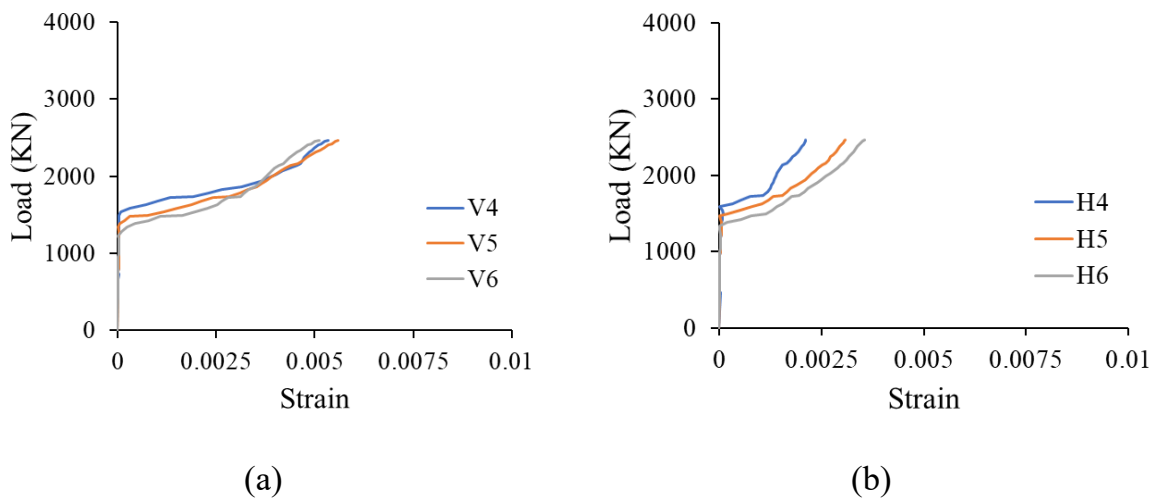
Figure 3.8: Numerical GFRP strains in web reinforcement for DB-S: (a) Vertical stirrups; (b) Horizontal bars
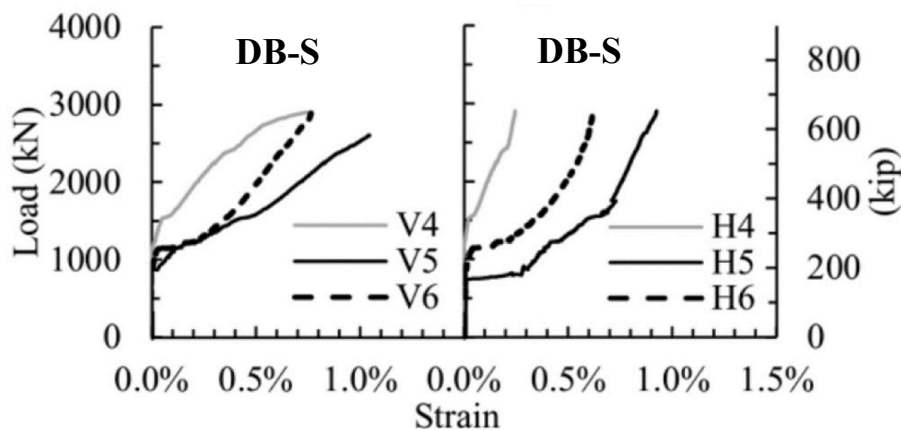
Figure 3.9: Measured GFRP strains in web reinforcement for DB-S [34]

The strains in the flexural reinforcement were monitored in the midspan and at different locations along the shear span. Monitoring points were also installed on GFRP bars to record the strains in the vertical stirrups and horizontal bars at the corner of the openings. Figure 3.10 shows the locations of the monitoring points for a typical deep beam model with a web opening. The strains predicted numerically in the flexural reinforcement are plotted against the load in Figure 3.11. A bi-linear strain response was recorded for all the beam models. The strain response of the beam models with a web opening coincided with that of the solid beam DB-S at all locations, except near the

support where lower longitudinal strains were recorded for the beam models with a web opening. The beam models with a web opening failed at a lower load than that of DB-S, and hence, the strain at ultimate load was lower. The strain response at all locations was insignificantly different, expect at the region near the support having lower strains, verifying the arch action effect. The strain profile obtained from the experiments shown in Figure 3.12 verified the uniform distribution of strains in the flexural GFRP reinforcement within the beam span except at support location. In alignment with the numerical findings, the measured strains at peak loads for the deep beams with a web opening were significantly lower than that of DB-S. Figures 3.13 and 3.14 show the strain response predicted numerically in the vertical and horizontal web reinforcement, respectively. A bi-linear strain response was recorded in all beam models. No strains were recorded prior to the initiation of shear cracks at the opening corners. The strains at the two opposite corners of the openings were almost identical. The strains in the post-cracking stage for the deep models with extra GFRP reinforcement around the opening increased at a lightly lower rate than that of DB-O1. The strains in the vertical web reinforcement at peak load were higher than those of the horizontal web reinforcement, implying a greater contribution to the shear capacity.
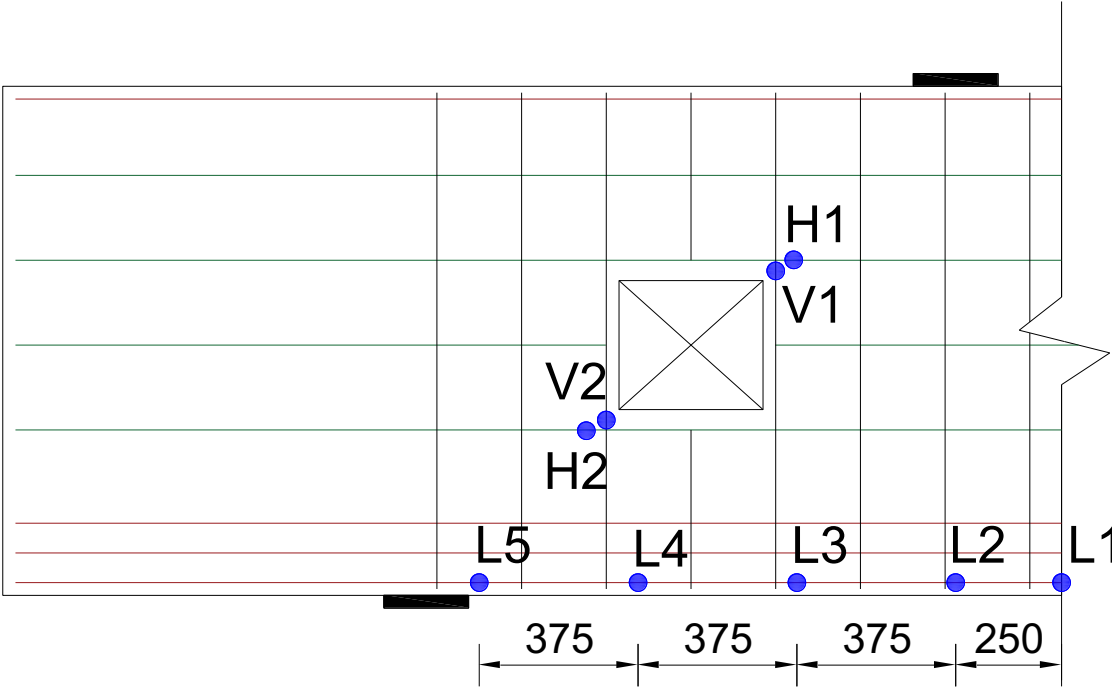
Figure 3.10: Locations of the monitoring points for GFRP strains in models with a web opening (Dimensions are in mm)
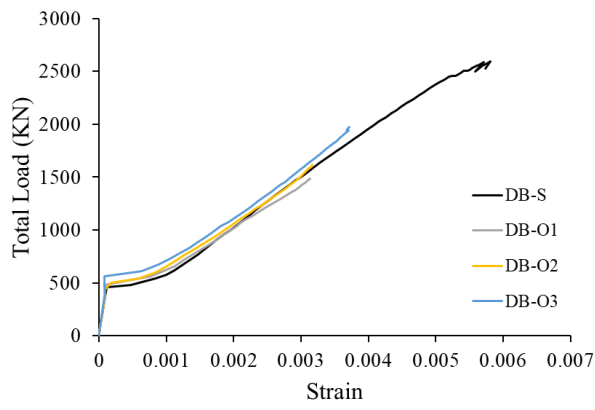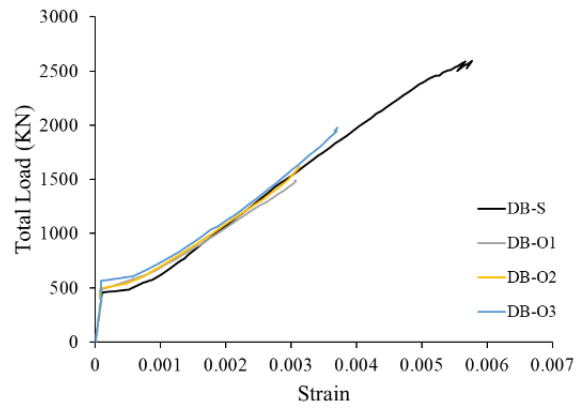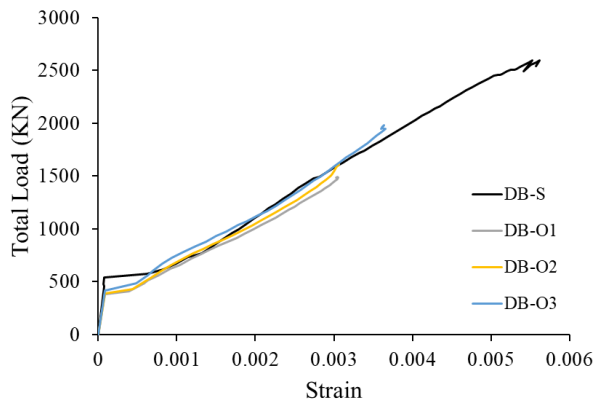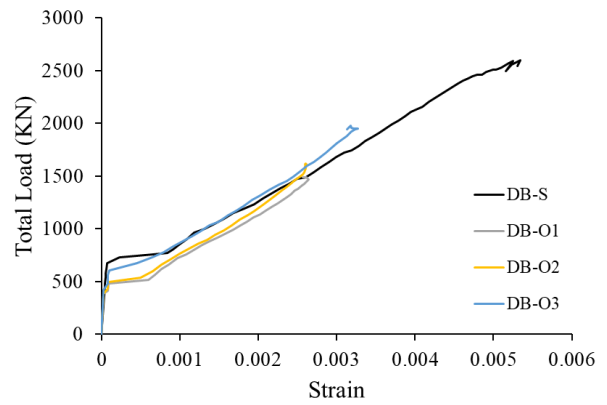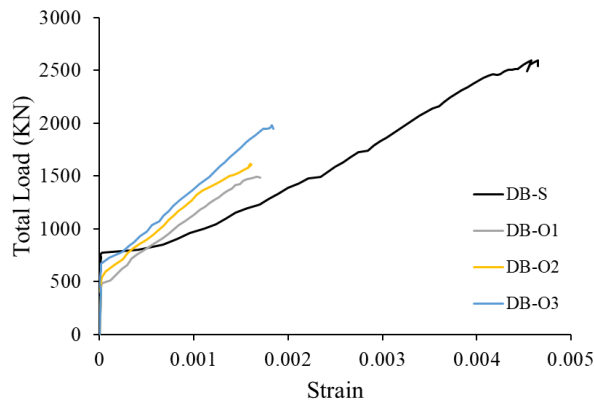
Figure 3.11: Numerical GFRP strains in flexural reinforcement: (a) L1; (b) L2; (c) L3; (d) L4; (e) L5
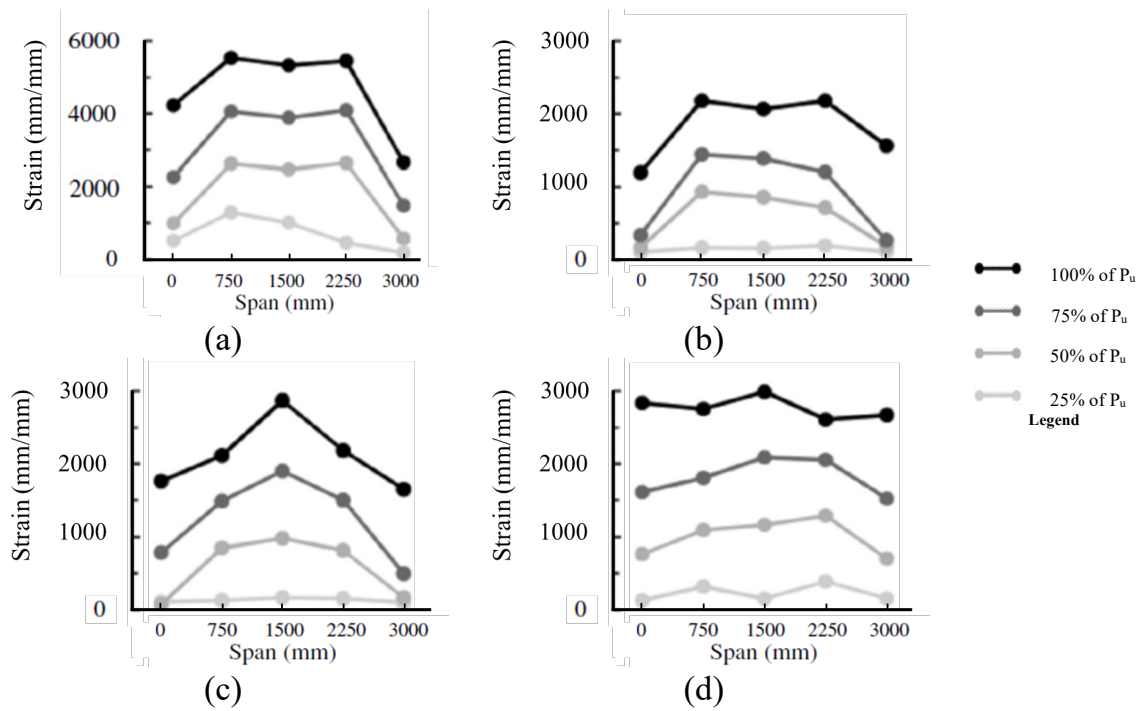
Figure 3.12: Measured GFRP strains in flexural reinforcement [34]: (a) DB-S; (b) DB-O1; (c) DB-O2; (d) DB-O3
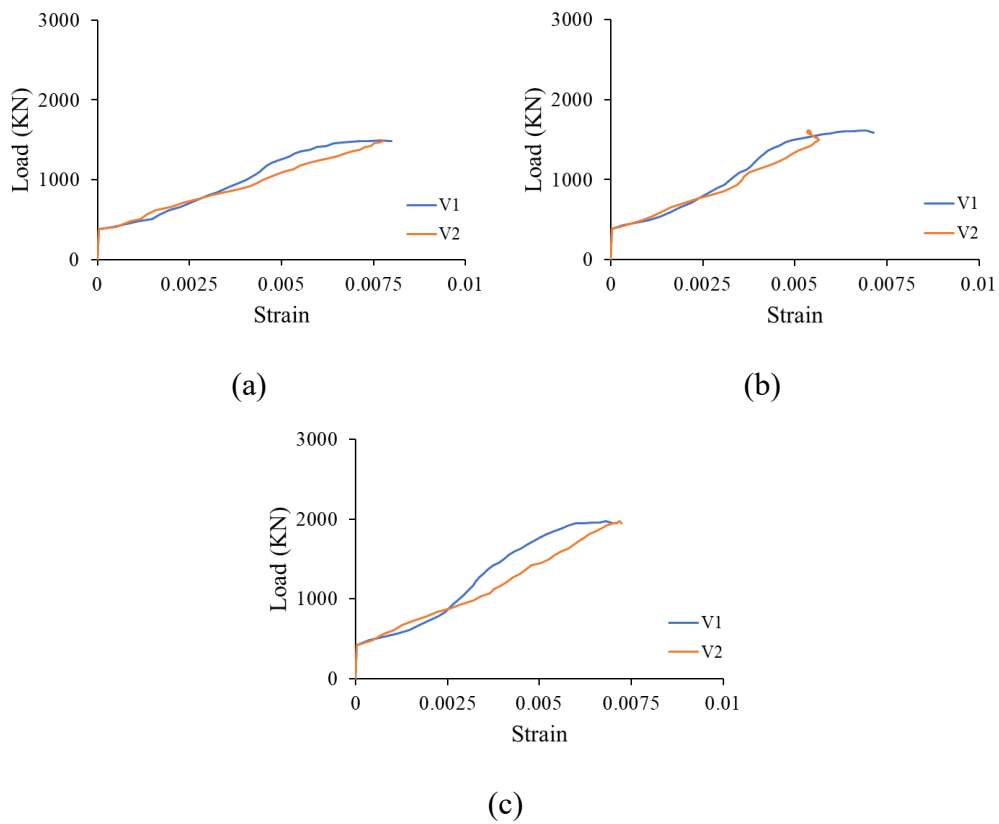
Figure 3.13: Numerical GFRP strains in vertical web reinforcement at opening corners: (a) DB-O1; (b) DB-O2; (c) DB-O3
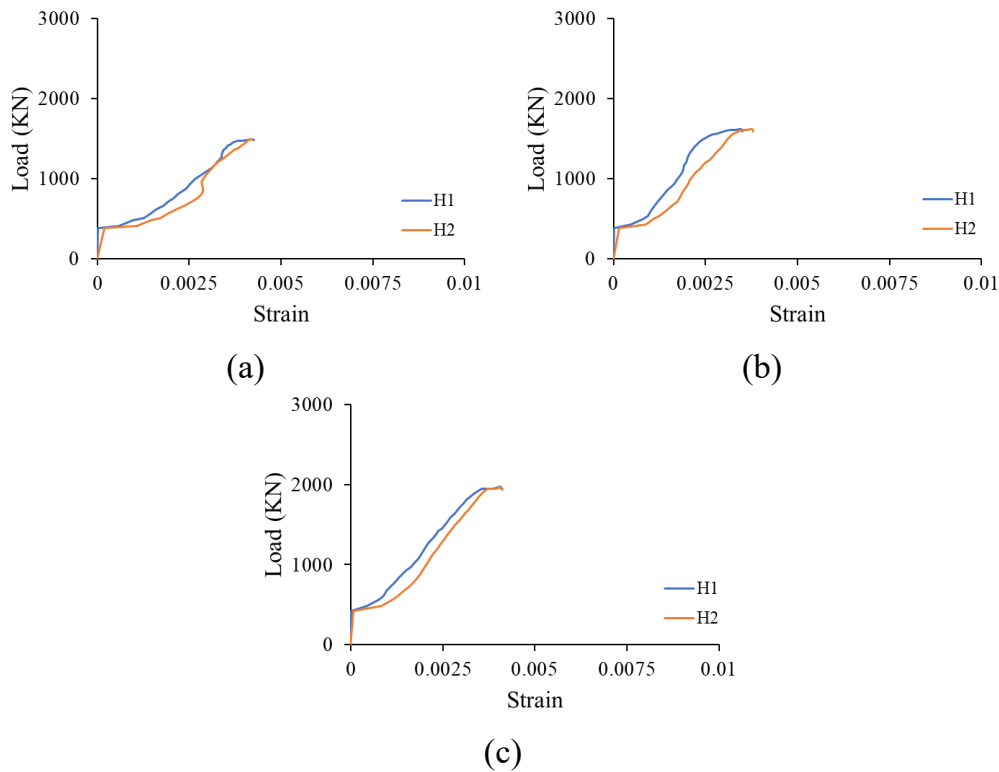
Figure 3.14: Numerical GFRP strains in horizontal web reinforcement at opening corners: (a) DB-O1; (b) DB-O2; (c) DB-O3

Figures 3.15, 3.16, and 3.17, show the stresses in the vertical stirrups, horizontal web reinforcement, and flexural reinforcement of the deep beam models at peak load, respectively. Portions of the web GFRP reinforcement crossing the diagonal strut in DB-S exhibited the highest stresses, as shown in Figure 3.15a. There was, however, a concentration of stresses in the top horizontal portion of the vertical stirrup under the load point in DB-S. The stress in this location was almost equal to that of the tensile strength of the bent portion of GFRP bars, indicating localized rupture of GFRP at this location. These numerical findings are consistent with the published experimental data, which indicated that crushing of the diagonal concrete strut in DB-S was accompanied by a localized rupture at the bent portion of the vertical stirrups [34]. For DB-O1, the stress in the bent portions of the vertical GFRP stirrups at the sides of the opening almost reached the tensile strength of the bent portion of GFRP bars. The experimental findings also indicated that rupture of the bent portions of the vertical GFRP stirrups near the load and support plates occurred at the ultimate load along with crushing of concrete along the diagonal cracks developed in the upper and lower chords [34]. The stresses in the

42

vertical stirrups for DB-O2 and DB-O3 with the extra GFRP reinforcement around the opening were below the tensile strength of the bent portion of GFRP bars. These results verify the effectiveness of the extra GFRP bars in relieving the web reinforcement, which allowed the beam models to develop a higher load capacity. The stresses in the horizontal web reinforcement in DB-O2 and DB-O3 at peak load were also lower than those of DB-O1 (Figure 3.16), which is in alignment with the behavior of the vertical stirrups. The maximum stress in the flexural reinforcement at peak load for DB-S was 390 MPa (i.e., 39% of the tensile strength of straight GFRP bars). The models with a web opening failed at a lower load than that of DB-S, and hence, the maximum stress in the flexural reinforcement was lower at an average value of 265 MPa (i.e., 27% of the tensile strength of straight GFRP bars).

(a) (b)

(c) (d)
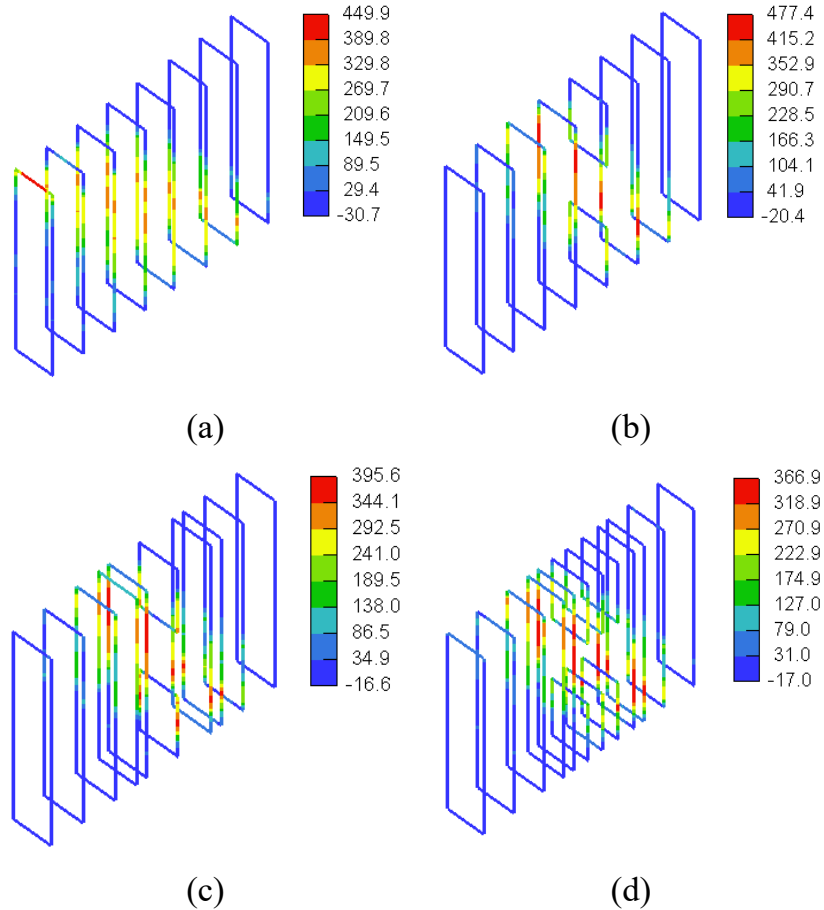
Figure 3.15: 3D view of stresses in vertical GFRP stirrups (MPa): (a) DB-S; (b) DB-O1; (c) DB-O2; (d) DB-O3
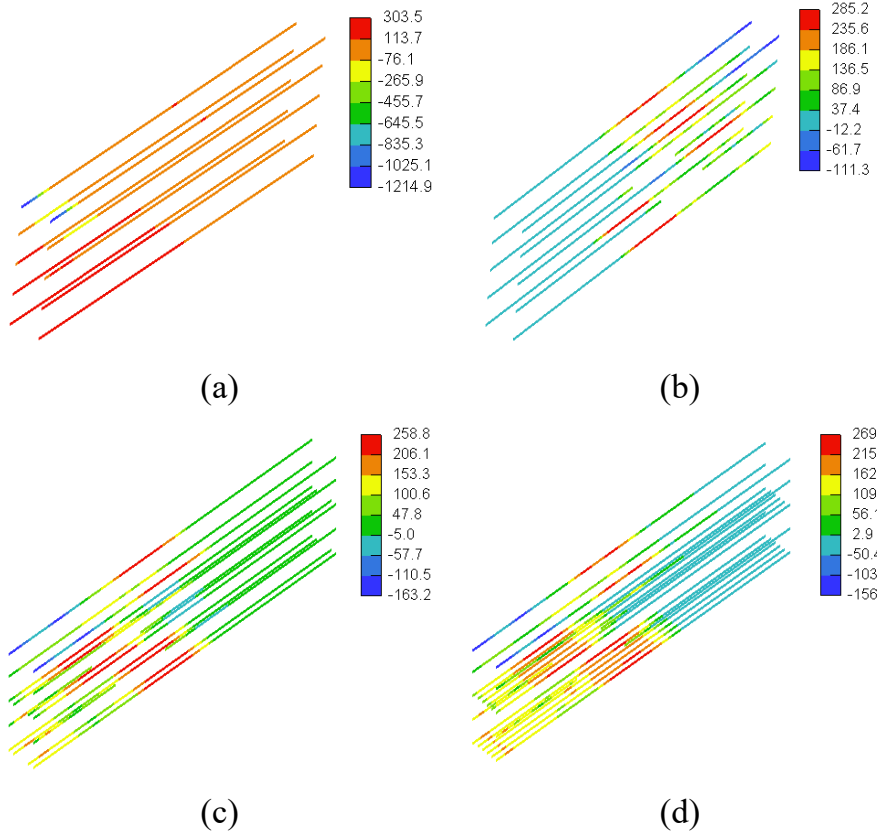
Figure 3.16: 3D view of stresses in horizontal web reinforcement (MPa): (a) DB-S; (b) DB-O1; (c) DB-O2; (d) DB-O3
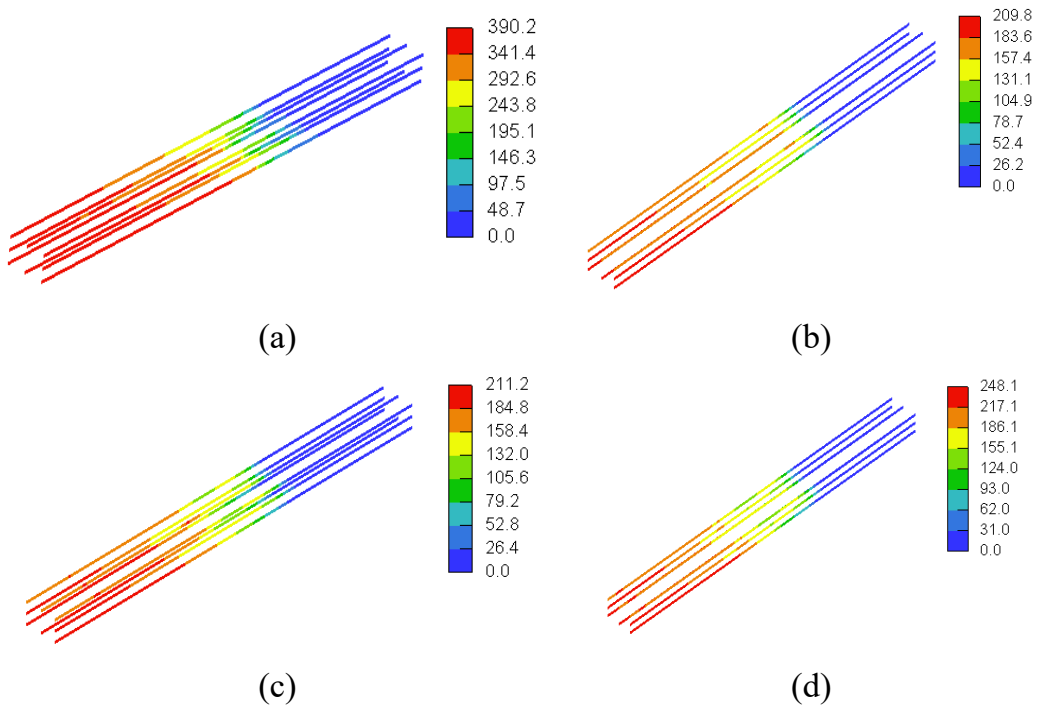
Figure 3.17: 3D view of stresses in flexural reinforcement (MPa): (a) DB-S; (b) DB-O1; (c) DB-O2; (d) DB-O3

44

Chapter 4: Results and Discussions

4.1 Overview

Results of the parametric study are presented in this chapter. The results include the load-deflection response, crack propagation, failure mechanism, and stresses in the GFRP reinforcement. Refined analytical formulas for shear strength prediction of GFRP-reinforced concrete deep beams with and without openings were introduced based on regression analysis of the numerical results. Predictions of the refined analytical formulas are presented and compared to those of the simulation models at the end of the chapter.

4.2 Results of the Solid Deep Beam Models

4.2.1 Results of the Solid Deep Beam Models without Web Reinforcement

The deep beam models of this group were solid without web reinforcement. The variables of this group were the concrete compressive strength (f'_c) and a/h. The a/h value was either 1.0 or 1.5. Values of f'_c were 28, 37, and 50 MPa, representing low (L), moderate (M), and high (H) concrete compressive strengths, respectively.

4.2.1.1 Load-Deflection Response

Figures 4.1a and 4.1b show the load-deflection responses of the deep beam models without web reinforcement having a/h of 1.0 and 1.5, respectively. The beam models exhibited a bi-linear response, irrespective of values of f'_c and a/h. In the first stage, a linear response was recorded until initiation of flexural cracks, which caused a change in the slope of the load-deflection response. Changing the concrete compressive strength insignificantly reduced the post-cracking stiffness of the beam models. Nevertheless, the post-cracking stiffness of the beam models with $a/h = 1.5$ was significantly lower than that of their counterparts with $a/h = 1.0$. The deflection continued to increase with an increase in the applied load until the ultimate load was reached. The beam models with the higher f'_c of 50 MPa failed at a deflection capacity greater than that of their counterparts with the low and moderate f'_c of 28 and 37 MPa, respectively.

Furthermore, the beam models with *a/h* =1.5 had a higher deflection capacity than that of their counterparts with *a/h* =1.0.
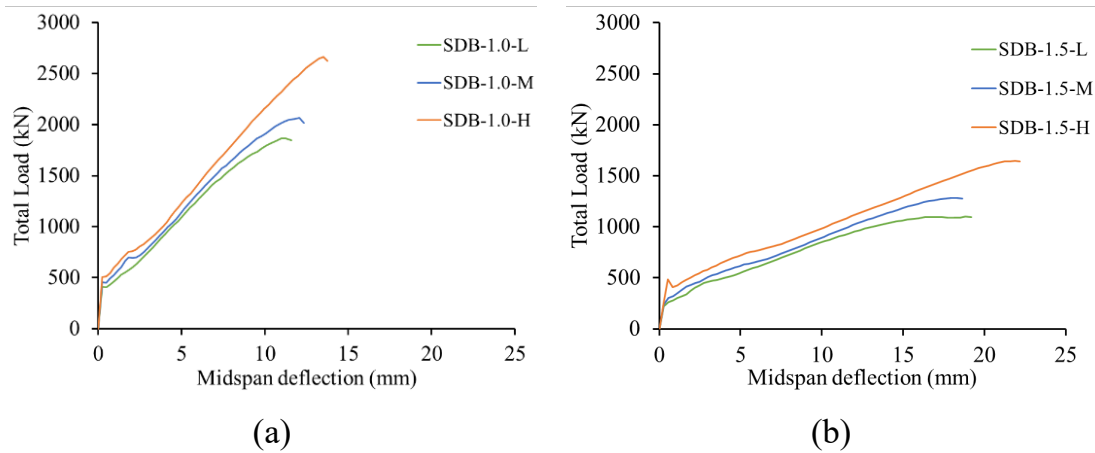
Figure 4.1: Load-deflection responses of solid deep beam models without web reinforcement: (a) *a/h* = 1.0; (b) *a/h* = 1.5

Table 4.1 presents the ultimate load and the deflection capacity for the solid beam models without web reinforcement. The ultimate loads of the deep models increased with an increase in the concrete compressive strength. The strengths of the deep beam models SDB-1.0-M and SDB-1.0-H were 11 and 43% higher than that of the model SDB-1.0-L. Similarly, the ultimate loads of the deep beam models SDB-1.5-M and SDB-1.5-H were 17 and 49% higher than that of the model SDB-1.5-L. The ultimate loads of the deep models with *a/h* = 1.5 were lower than those of their counterparts with *a/h* = 1.0. The beam models SDB-1.5-L, SDB-1.5-M, and SDB-1.5-H with the low (L), moderate (M), and high (H) concrete compressive strengths showed strength reductions of 41, 38, and 38%, respectively due to increasing the value of *a/h* 1.0 to 1.5. These results indicate that varying the concrete compressive strength had almost no effect on the strength reduction caused by increasing the value of *a/h* 1.0 to 1.5. The deflection capacity of the beam models with the low and moderate f'_c were significantly different, irrespective of *a/h*. The beam models with the higher concrete compressive strength failed at a higher deflection capacity than that of their counterparts with the low and moderate concrete compressive strength. Figure 4.2 shows the effect of f'_c and *a/h* on the strength of solid beam models without web reinforcement. The ultimate load increased almost linearly with an increase in f'_c, irrespective of the value of *a/h*. The beam models

46

with *a/h* = 1.0 exhibited higher strengths than those of their counterparts with *a/h* = 1.5. The strength gain caused by reducing the value of *a/h* from 1.5 to 1.0 was in the range of 64% with a minimum of 61% and a maximum of 69%.

Table 4.1: Numerical results of the solid deep beam models without web reinforcement

Group a/h	Model	f_c' (MPa)	Ultimate Load (kN)	Deflection at Ultimate (mm)
1.0 (a = 1250 mm)	SDB-1.0-L	28	1865	11.3
	SDB-1.0-M	37	2064	12.1
	SDB-1.0-H	50	2661	13.5
1.5 (a = 1800 mm)	SDB-1.5-L	28	1101	18.8
	SDB-1.5-M	37	1284	18.3
	SDB-1.5-H	50	1644	21.9
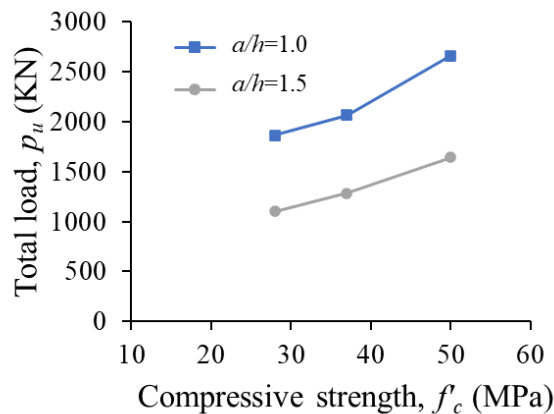
Figure 4.2: Effect of the concrete compressive strength and shear span ratio on the strength of solid beam models without web reinforcement

4.2.1.2 Crack Pattern and Failure Mechanism

Figures 4.3 and 4.4 show the crack development and propagation for sample deep beam models without web reinforcement. The crack patterns of all beam models at peak load are provided in Appendix A.1. The beam models exhibited flexural cracks in the midspan and in the shear span region closer to the load point prior to initiation of any shear cracks. When the load was increased a major shear crack was developed in the shear span with an angle of inclination of approximately 60° from the horizontal direction. This shear crack was connected to another splitting crack developed horizontally at the level of the flexure reinforcement due to the absence of vertical

stirrups. Only the beam model SDB-1.5-L showed two shear cracks in the shear span in addition to the splitting cracks that were developed longitudinally at the level of the flexural reinforcement (Figure 4.4). Eventually, all beam models failed in a shear-tension mode of failure.
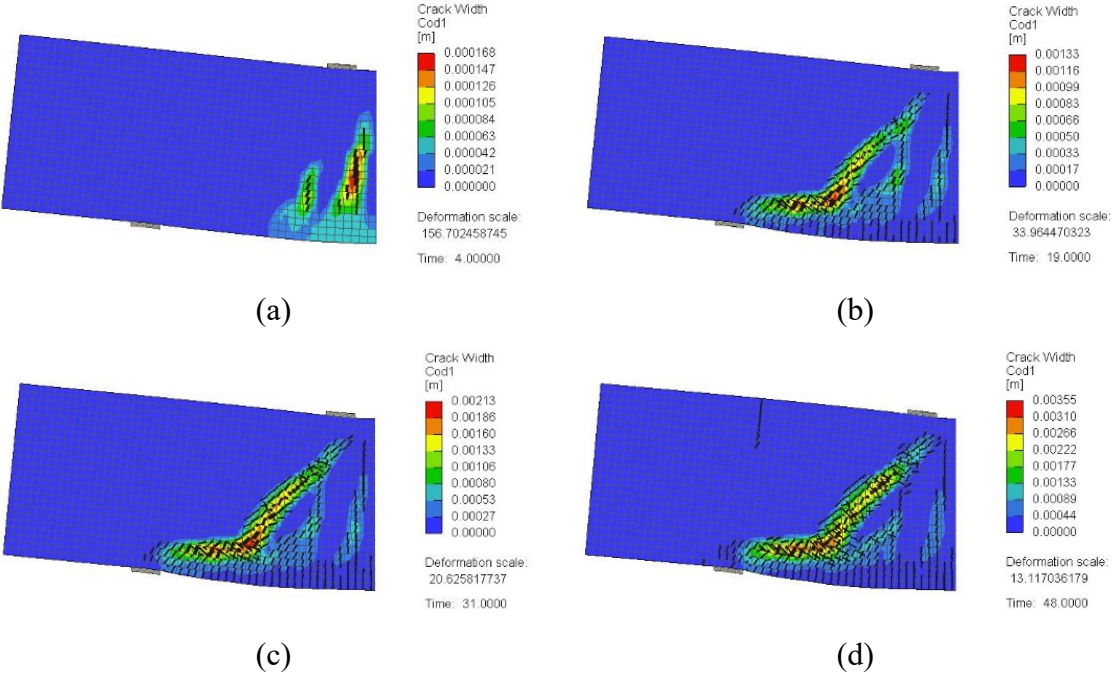
Figure 4.3: Crack pattern for a typical solid model without web reinforcement having *a/h* = 1.0 (SDB-1.0-M): (a) at 25% of peak load; (b) at 50% of peak load; (c) at 75% of peak load; (d) at 100% of peak load

(a)

(b)

(c)

(d)
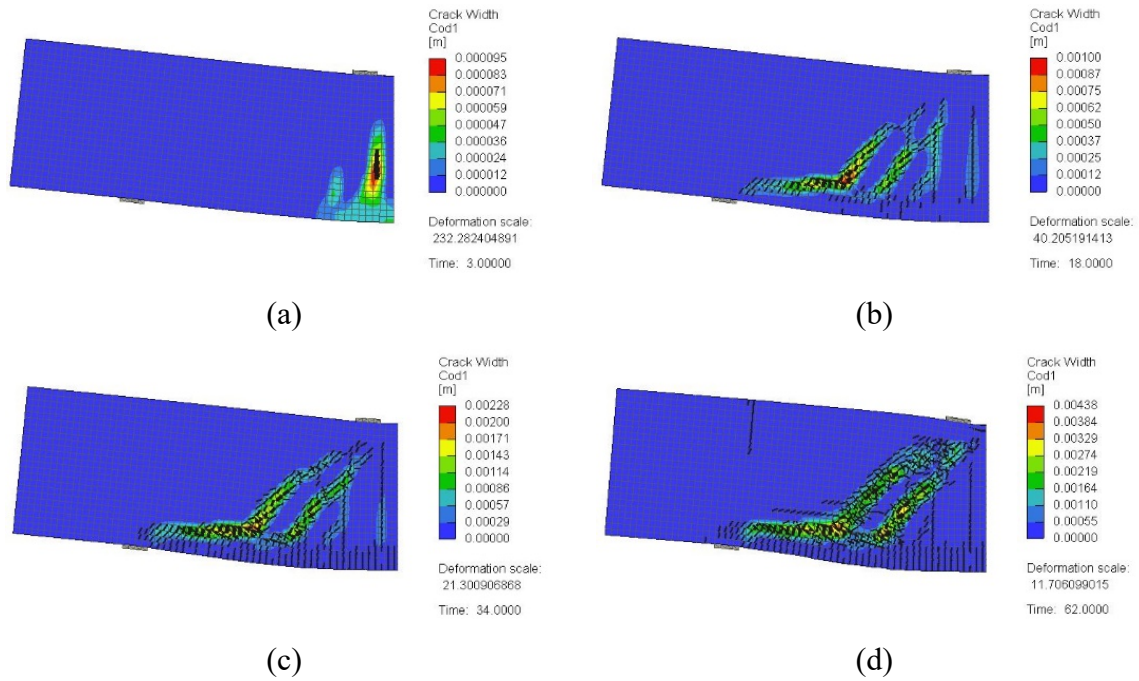
Figure 4.4: Crack pattern for a typical solid model without web reinforcement having *a/h* = 1.5 (SDB-1.5-L): (a) at 25% of peak load; (b) at 50% of peak load; (c) at 75% of peak load; (d) at 100% of peak load

4.2.1.3 GFRP Stresses

Figures 4.5 and 4.6 show general 3D views of the stresses in the GFRP reinforcement predicted numerically for the beam models with *a/h* = 1.0 and *a/h* = 1.5, respectively. It is evident that the flexural GFRP reinforcement at the tension side acted as a tie because they featured a uniform stress distribution along the shear span. The beam models with the higher concrete compressive strength sustained a higher ultimate load, and hence, featured higher GFRP stresses at peak load than those of the beam models with the lower concrete compressive strength. The flexural GFRP reinforcing bars did not reach their tensile strength in any of the beam models. For the beam models with *a/h* = 1 (Figure 4.5), the GFRP stress in the flexural reinforcement at tension side at peak load was on average 342 MPa (i.e., 34% of the tensile strength of straight GFRP bars), with a minimum of 292 (i.e., 29% of the tensile strength of straight GFRP bars), and a maximum of 410 MPa (i.e., 41% of the tensile strength of straight GFRP bars). The maximum GFRP stresses at peak load for the beam models with *a/h* = 1.5 were slightly lower than those of their counterparts with *a/h* = 1.0. For the beam models with *a/h* = 1.5 (Figure 4.6), the GFRP stress in the flexural reinforcement at tension side at

49

peak load was on average 308 MPa (i.e., 31% of the tensile strength of straight GFRP bars), with a minimum of 256 (i.e., 26% of the tensile strength of straight GFRP bars), and a maximum of 376 MPa (i.e., 38% of the tensile strength of straight GFRP bars).

| (a) | (b) | (c) |
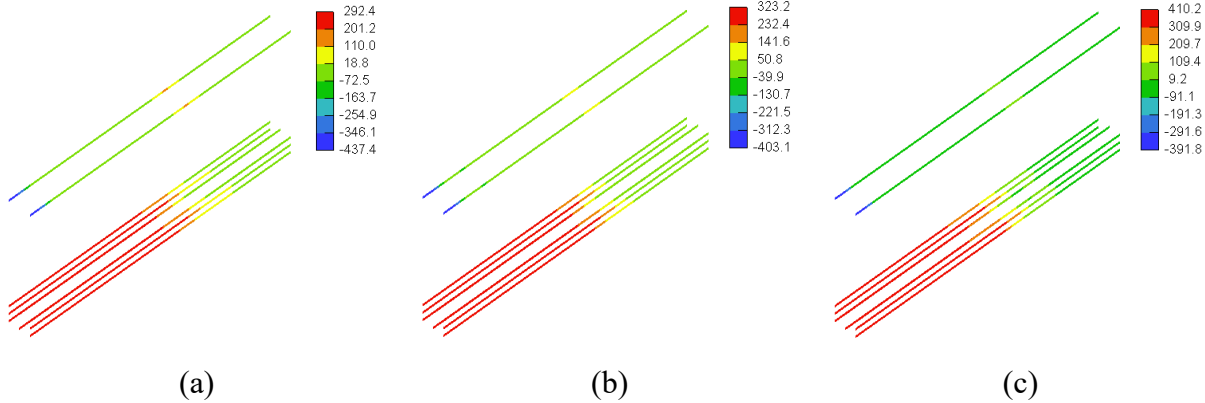
Figure 4.5: Stresses in GFRP reinforcement for models with *a/h* = 1 (MPa): (a) SDB-1.0-L; (b) SDB-1.0-M; (c) SDB-1.0-H

| (a) | (b) | (c) |
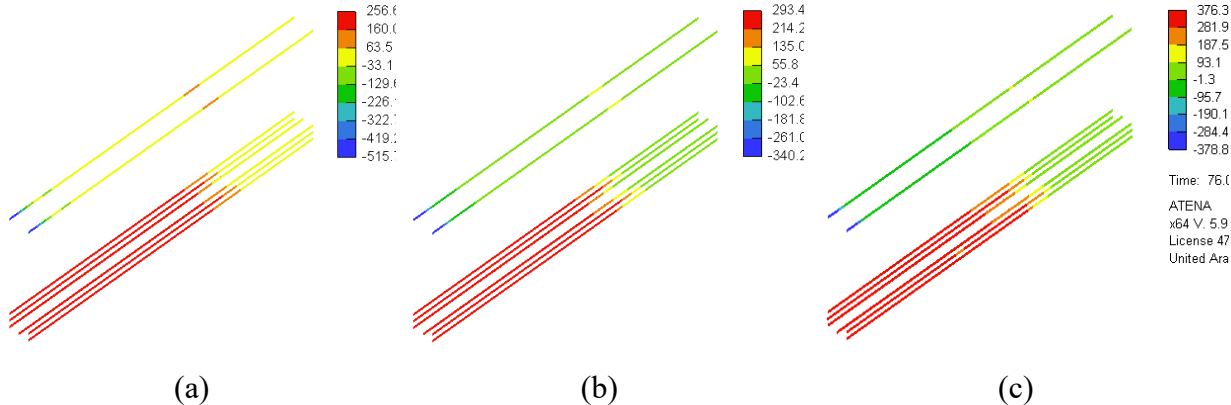
Figure 4.6: Stresses in GFRP reinforcement for models with *a/h* = 1.5 (MPa): (a) SDB-1.5-L; (b) SDB-1.5-M; (c) SDB-1.5-H

4.2.2 Results of the Solid Deep Beam Models with Web Reinforcements

The deep beam models of this group were solid. The variables of this group were the concrete compressive strength (f'_c), value of *a/h*, and spacing between the web reinforcement (*s*). The beam models had *a/h* value of either 1.0 or 1.5. Values of f'_c were 28, 37, and 50 MPa representing low (L), moderate (M), and high (H) concrete strengths, respectively. The spacing between the web reinforcement was either 100 or 200 mm, which corresponded to 0.08*h* and 0.17*h*, respectively.

50

4.2.2.1 Load-Deflection Response

Figures 4.7 and 4.8 show the load-deflection responses of the deep beam models with web reinforcement having *a/h* of 1.0 and 1.5, respectively. The responses of the counterpart deep beam models with *a/h* of 1.5 are provided in Figures 4.7a to 4.7c. At the early stage of loading, the deflection increased linearly with an increase in the applied load until flexural cracking occurred. Following flexural cracking, the deflection continued to increase in a quasilinear fashion at a higher rate until the ultimate load was reached. Development and/or initiation of major shear cracks at load values close to the ultimate load caused a load decay and/or another minor change in the slope of the load-deflection response prior to reaching the ultimate load. Figures 4.7 and 4.8 show that the cracking load slightly increased with an increase in the compressive strength of the concrete. Changing the spacing between the web reinforcement did not affect the pre-cracking stiffness. Nevertheless, the post-cracking stiffness of the beam models with the larger spacing of 200 mm was slightly lower than that of their counterparts with the smaller spacing of 100 mm. The deflection capacity was not significantly affected by the spacing between the web reinforcement, expect for the beam models with the low concrete grade of 28 MPa, where a reduction in the deflection capacity was recorded for the deep beam models with the larger spacing between web reinforcement. When the responses of the beam models with *a/h* of 1.0 (Figure 4.7) are compared to those of their counterparts, *a/h* of 1.5 (Figure 4.8), it can be seen that an increase in *a/h* reduced the cracking load, post-cracking stiffness, and ultimate load. The deep beam models with *a/h* of 1.0 failed, however, at deflection values lower than those of their counterparts with *a/h* of 1.5.
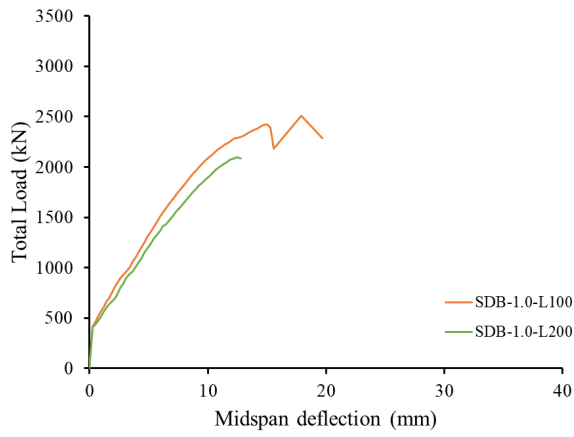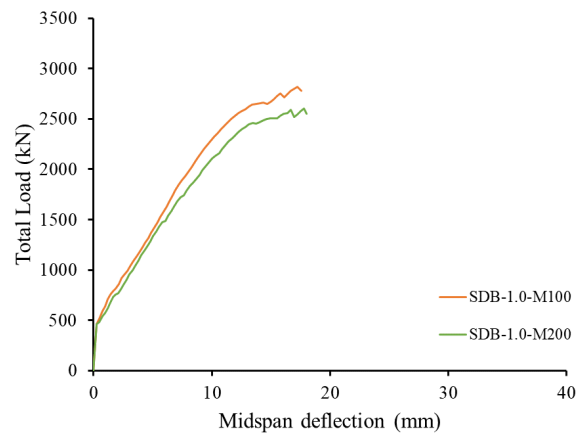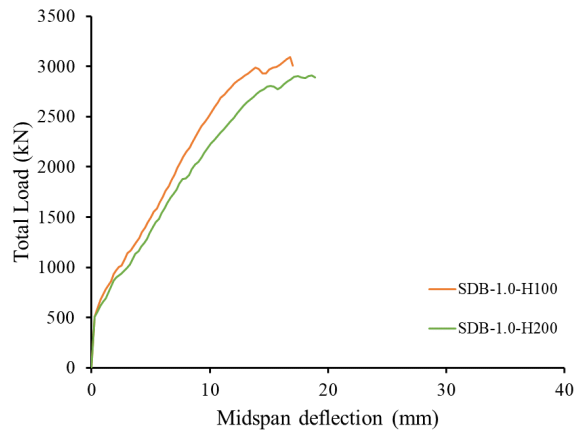
Figure 4.7: Load-deflection responses of solid deep beam models with web reinforcement having a/h = 1.0: (a) f'_c = 28 MPa (b) f'_c = 37 MPa; (c) f'_c = 50 MPa
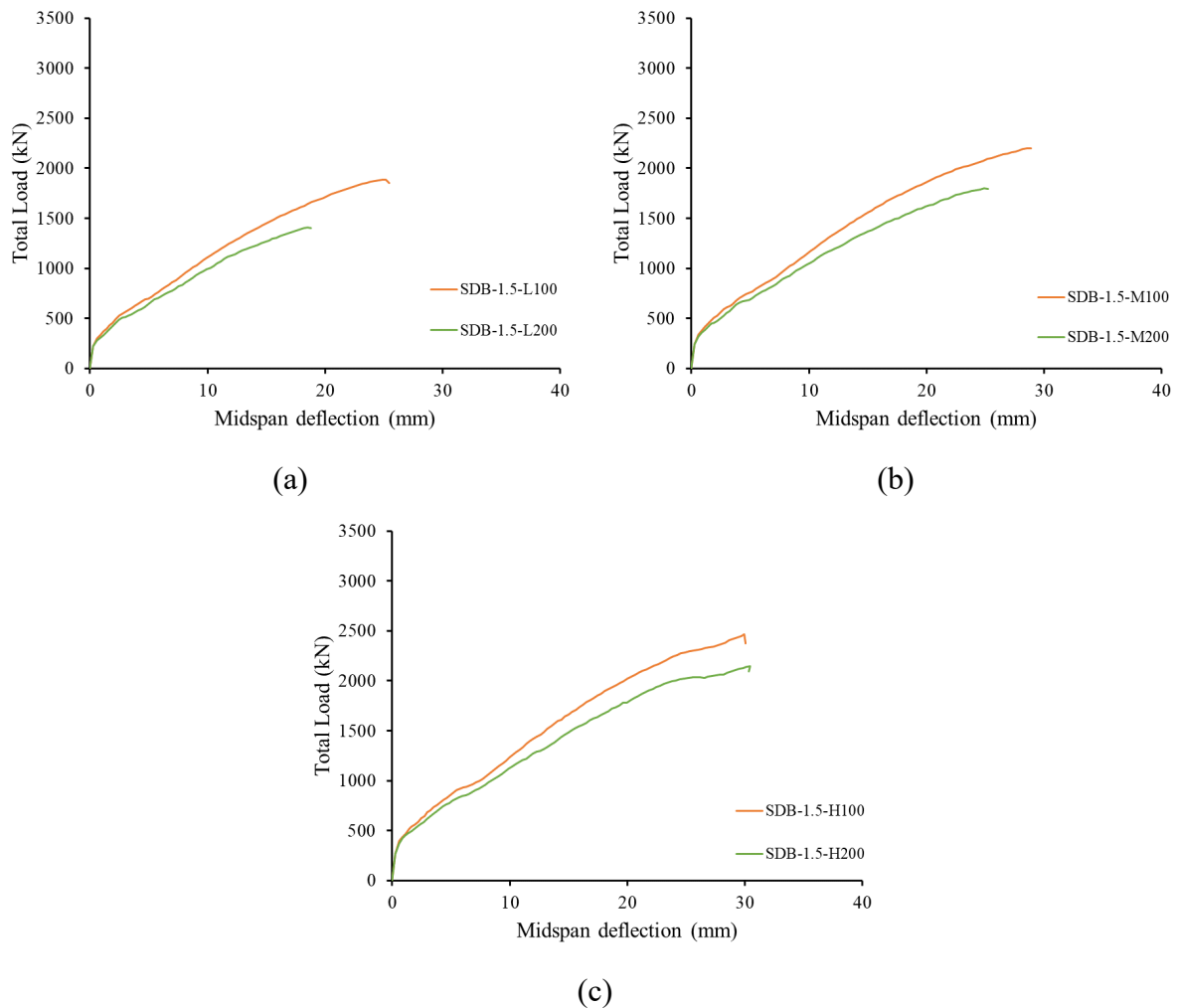
Figure 4.8: Load-deflection responses of solid deep beam models with web reinforcement having $a/h = 1.5$: (a) $f'_c = 28$ MPa (b) $f'_c = 37$ MPa; (c) $f'_c = 50$ MPa

Table 4.2 presents the ultimate load and the deflection capacity for the beam models of this group. The ultimate load of the deep models with $a/h = 1.5$ were lower than those of their counterparts with $a/h = 1.0$. The beam models SDB-1.5-L100, SDB-1.5-M100, and SDB-1.5-H100 with $s = 100$ mm exhibited strength reductions of 25, 22, and 21%, respectively, due to increasing the value of a/h 1.0 to 1.5. Their counterpart beam models SDB-1.5-L200, SDB-1.5-M200, and SDB-1.5-H200 with $s = 200$ mm exhibited greater strength reductions of 33, 31, and 26%, respectively, due to increasing the value of a/h from 1.0 to 1.5. These results indicate that the strength reduction caused by increasing the value of a/h tended to decrease with an increase in the concrete compressive strength. Furthermore, the strength reduction caused by increasing the value of a/h was more pronounced for the beam models with the lower amount of web reinforcement (i.e., greater spacing between web reinforcement). Generally, the beam

53

models with *a/h* = 1.5 failed at a greater deflection capacity than that of their counterparts with *a/h* = 1.0. Such an increase in the deflection capacity due to increasing the value of *a/h* was more significant for the beam models with the higher concrete strength. Average increases of 44, 53, and 71% in the deflection capacity were recorded for the beam models with low (L), moderate (M), and high (H) concrete compressive strengths, respectively.

Table 4.2: Numerical results of the solid deep beam models with web reinforcement

a/h	f_c' (MPa)	Spacing between Web GFRP bars, (*s*) (mm)	Model Designation	Ultimate Load (kN)	Deflection at Ultimate (mm)
1.0 (*a* = 1250 mm)	28	100	SDB-1.0-L100	2510	17.9
		200	SDB-1.0-L200	2100	12.5
	37	100	SDB-1.0-M100	2821	17.3
		200	SDB-1.0-M200	2601	17.8
	50	100	SDB-1.0-H100	3094	16.8
		200	SDB-1.0-H200	2909	18.7
1.5 (*a* = 1800 mm)	28	100	SDB-1.5-L100	1885	25.2
		200	SDB-1.5-L200	1411	18.5
	37	100	SDB-1.5-M100	2199	28.5
		200	SDB-1.5-M200	1797	24.9
	50	100	SDB-1.5-H100	2464	30.0
		200	SDB-1.5-H200	2149	30.5

Figures 4.9a and 4.9b show the effect of the concrete compressive strength and spacing between web reinforcement on the strength of solid beam models with *a/h* values of 1.0 and 1.5, respectively. It is evident that the ultimate load increased almost linearly with an increase in the concrete compressive strength, irrespective of the value of *a/h* and the spacing between the web reinforcement. It is evident that increasing the amount of the web reinforcement through the use of a reduced spacing of 100 mm instead of 200 mm increased the strength of the beam models. The strength gain caused by increasing the amount of the web reinforcement was, however, dependent on the

54

concrete strength and the value of *a/h*. Figure 4.10 shows the effect of f_c' and *a/h* on the strength gain caused by increasing the amount of the web reinforcement in the solid beam models. For the beam models with *a/h* = 1.0, strength gains of 20, 8, and 6% were recorded for the beam models with low (L), moderate (M), and high (H) concrete compressive strengths, respectively. For the beam models with *a/h* = 1.5, strength gains of 34, 22, and 15% were recorded for the beam models with low (L), moderate (M), and high (H) concrete compressive strengths, respectively. These results imply that the impact of increasing the amount of the web reinforcement diminished with an increase in the concrete compressive strength. Furthermore, the strength gain caused by increasing the amount of web reinforcement was more pronounced for the beam models with the greater *a/h* of 1.5.

(a)   (b)
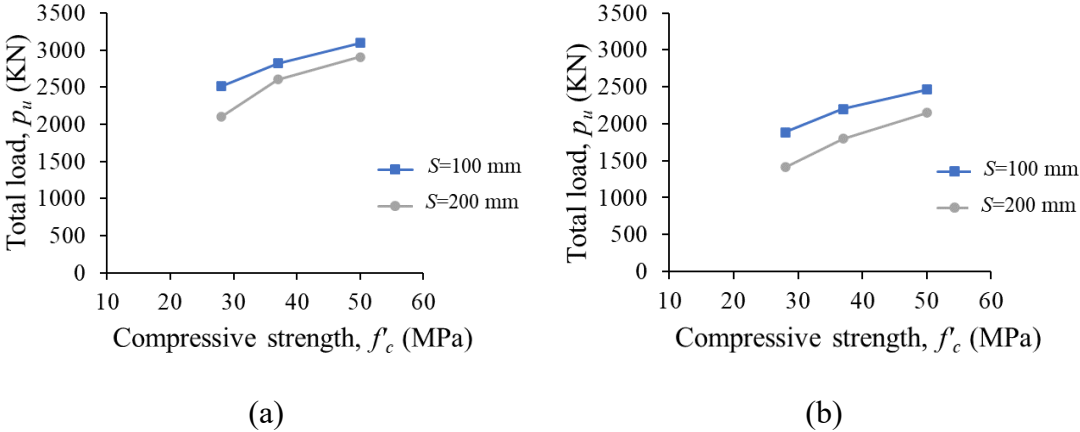
Figure 4.9: Effect of the concrete compressive strength and spacing between web reinforcement on the strength of solid beam models: (a) *a/h* = 1.0; (b) *a/h* = 1.5
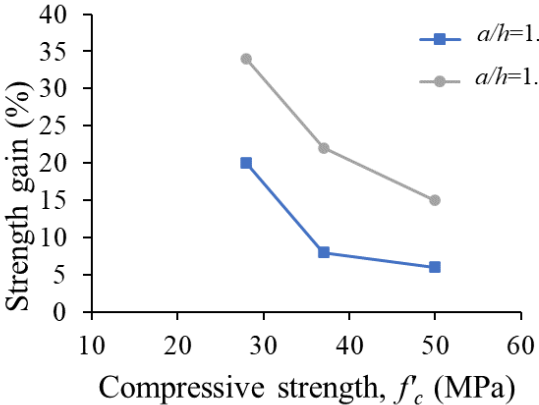
Figure 4.10: Effect of the concrete compressive strength and shear span ratio on the strength gain caused by increasing the web reinforcement in solid beam models

4.2.2.2 Crack Pattern and Failure Mechanism

Figures 4.11 and 4.12 show the crack development and propagation for sample deep beam models with *a/h* = 1.0 and web reinforcement spacing of 100 and 200 mm, respectively. The crack patterns of all beam models at peak load are provided in Appendix A.2. Flexural cracks initiated first in all deep beam models of this group. As the load increased, multiplate shear cracks were then developed along the natural load path connecting the load and support plates, noting that the beam models with the larger spacing of *s* = 200 mm exhibited fewer shear cracks within the shear span than those of the models with the smaller spacing of s = 100 mm. Further increase in the applied load resulted in development of additional shear cracks until ultimate load was reached along the strut connecting the support and load plates. It is noteworthy that the beam models with *s* = 100 mm exhibited a bottle-shaped strut at ultimate load. Figures 4.13 and 4.14 show the crack development and propagation for sample deep beam models with *a/h* = 1.5 and web reinforcement spacing of 100 and 200 mm, respectively. Flexural cracks were initiated at the early stage of loading in the midspan and in the region of the shear span closer to the load points. Several shear cracks were then developed in the shear span. The beam models with the smaller spacing of *s* = 100 mm exhibited higher number of well-distributed shear cracks within the shear span than those of the models with the larger spacing of *s* = 200 mm. Further increase in the applied load resulted in development of additional shear cracks until ultimate load was reached along the diagonal struts formed in the shear span. A fan-shaped distribution of diagonal cracks was formed at ultimate load.
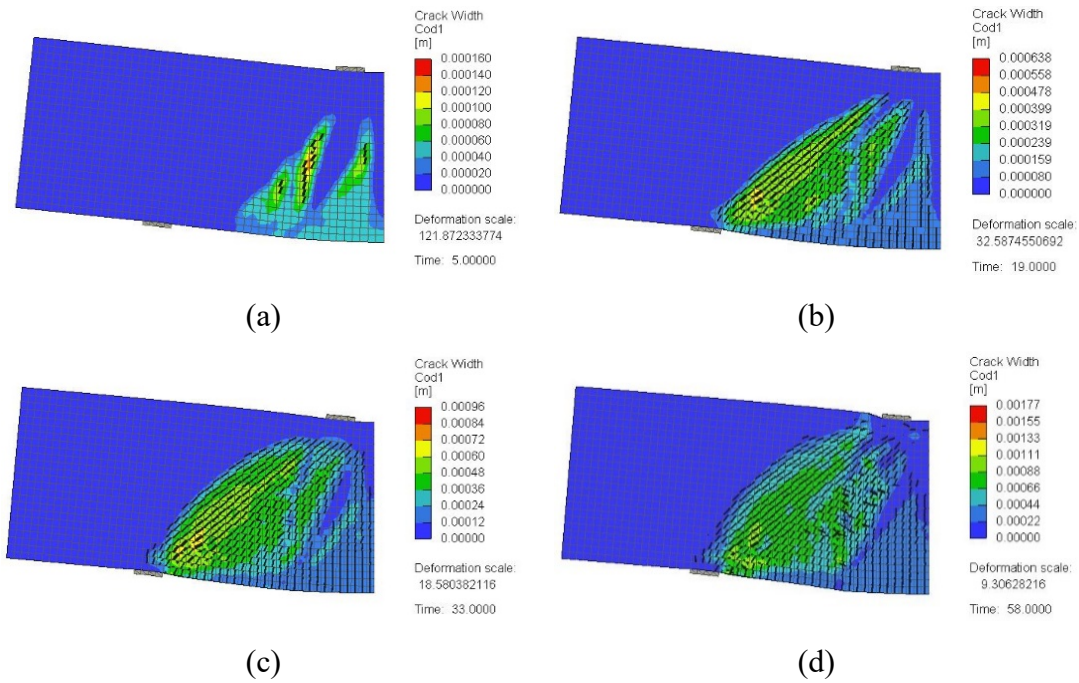
Figure 4.11: Crack pattern for a typical solid model with *a/h* = 1.0 and web reinforcement at *s* = 100 mm and (SDB-1.0-L100): (a) at 25% of peak load; (b) at 50% of peak load; (c) at 75% of peak load; (d) at 100% of peak load
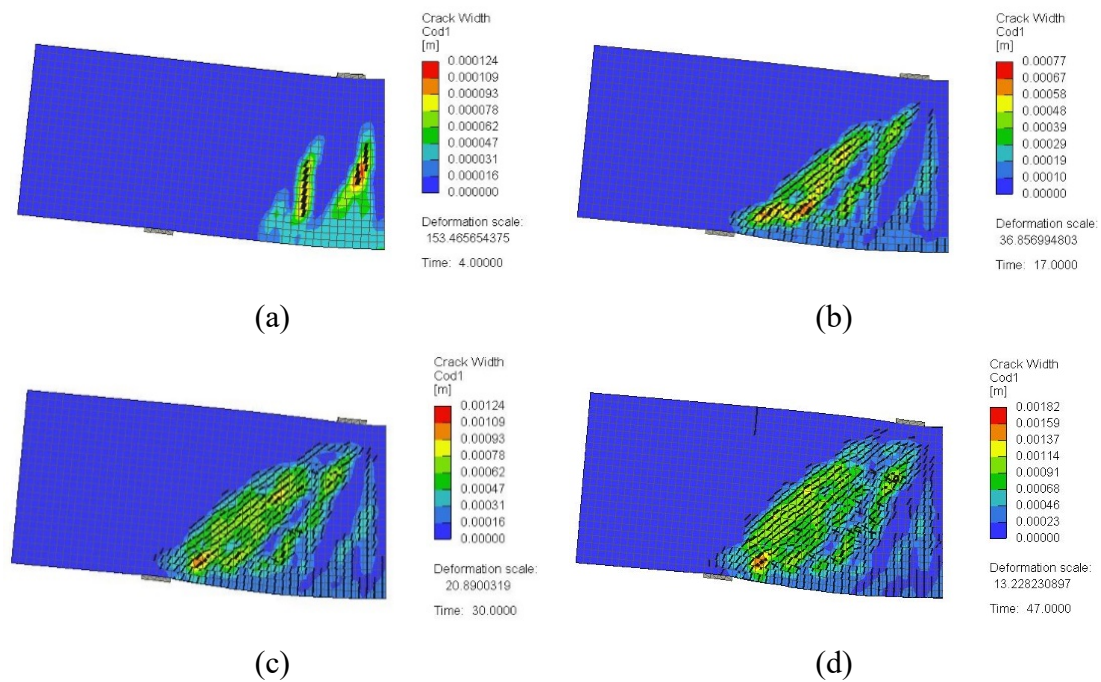
Figure 4.12: Crack pattern for a typical solid model with *a/h* = 1.0 and web reinforcement at *s* = 200 mm and (SDB-1.0-L200): (a) at 25% of peak load; (b) at 50% of peak load; (c) at 75% of peak load; (d) at 100% of peak load
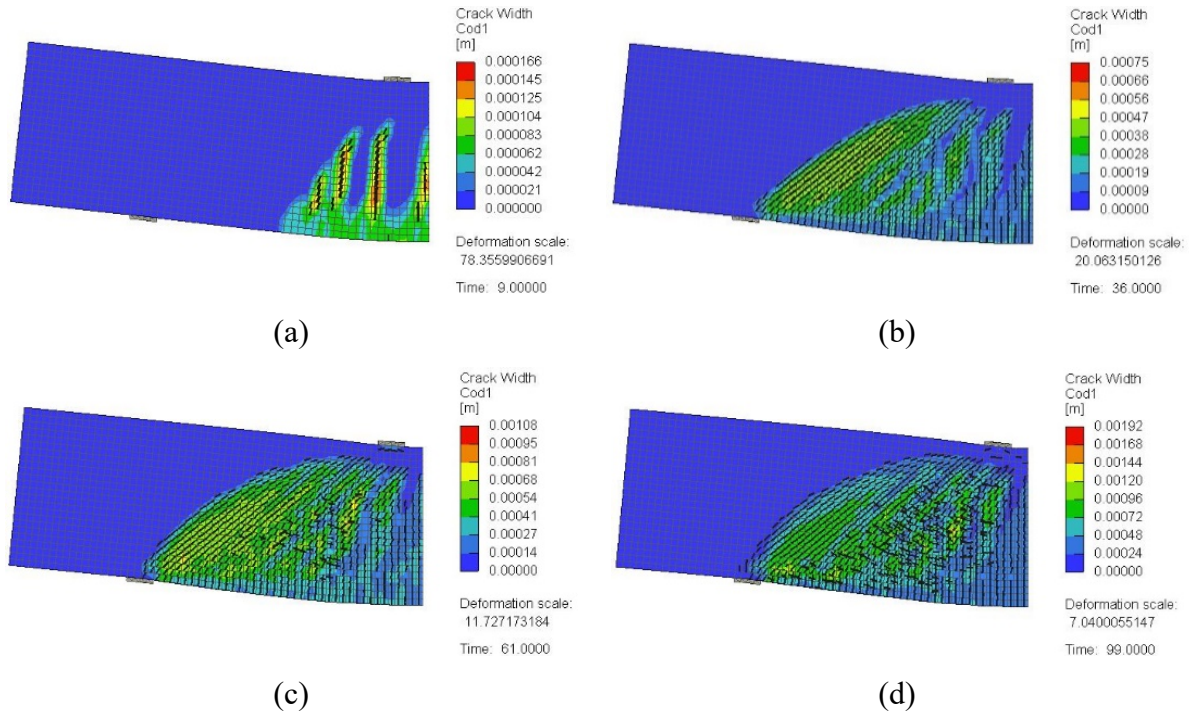
Figure 4.13: Crack pattern for a typical solid model with *a/h* = 1.5 and web reinforcement at *s* = 100 mm and (SDB-1.5-H100): (a) at 25% of peak load; (b) at 50% of peak load; (c) at 75% of peak load; (d) at 100% of peak load
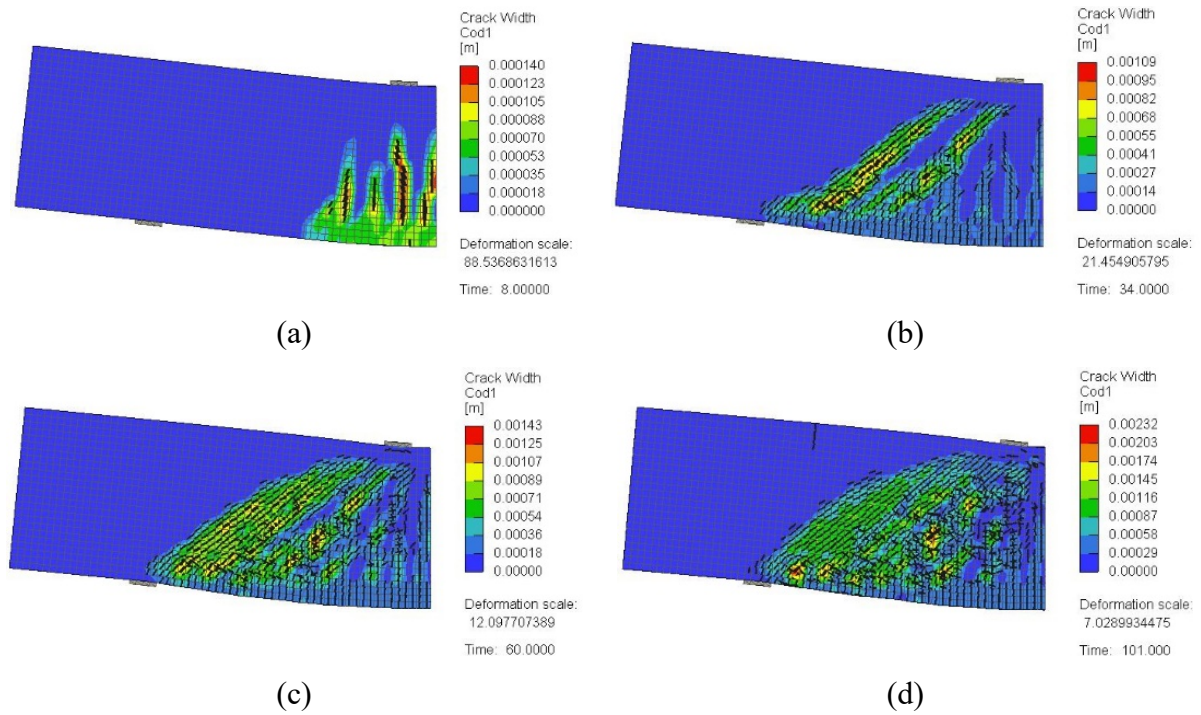
Figure 4.14: Crack pattern for a typical solid model with *a/h* = 1.5 and web reinforcement at *s* = 200 mm and (SDB-1.5-H200): (a) at 25% of peak load; (b) at 50% of peak load; (c) at 75% of peak load; (d) at 100% of peak load

4.2.2.3 GFRP Stresses

Figures 4.15 and 4.16 show general 3D views of the stresses in the vertical GFRP stirrups predicted numerically for the beam models with $a/h = 1.0$ and $a/h = 1.5$, respectively. From Figure 4.15, it can be seen that the top horizontal part along with the top bent portions of the vertical GFRP stirrup under the load plate in most of the beam models with $a/h = 1.0$ almost reached the tensile strength of the bent portion of GFRP bars. The beam model SDB-1.0-L200 was an exception where a maximum stress of 329 MPa (i.e., 72% of the tensile strength of the bent portion of GFRP bars) was recorded in the vertical GFRP stirrups. From Figure 4.16, it can be seen that none of the vertical GFRP stirrups for the beam models with $a/h = 1.5$ reached their tensile strength, expect in model SDB-1.5-H200. The top horizontal part along with the top bent portions of the vertical GFRP stirrup under the load plate in the model almost reached the tensile strength of the bent portion of GFRP (459 MPa). For the beam models with $a/h = 1.5$, the stresses in the vertical GFRP stirrups at peak load tended to increase with an increase in the concrete compressive strength. It seems that increasing the concrete compressive strength delayed failure of the beam and allowed the GFRP stirrups to contribute more to the shear capacity.
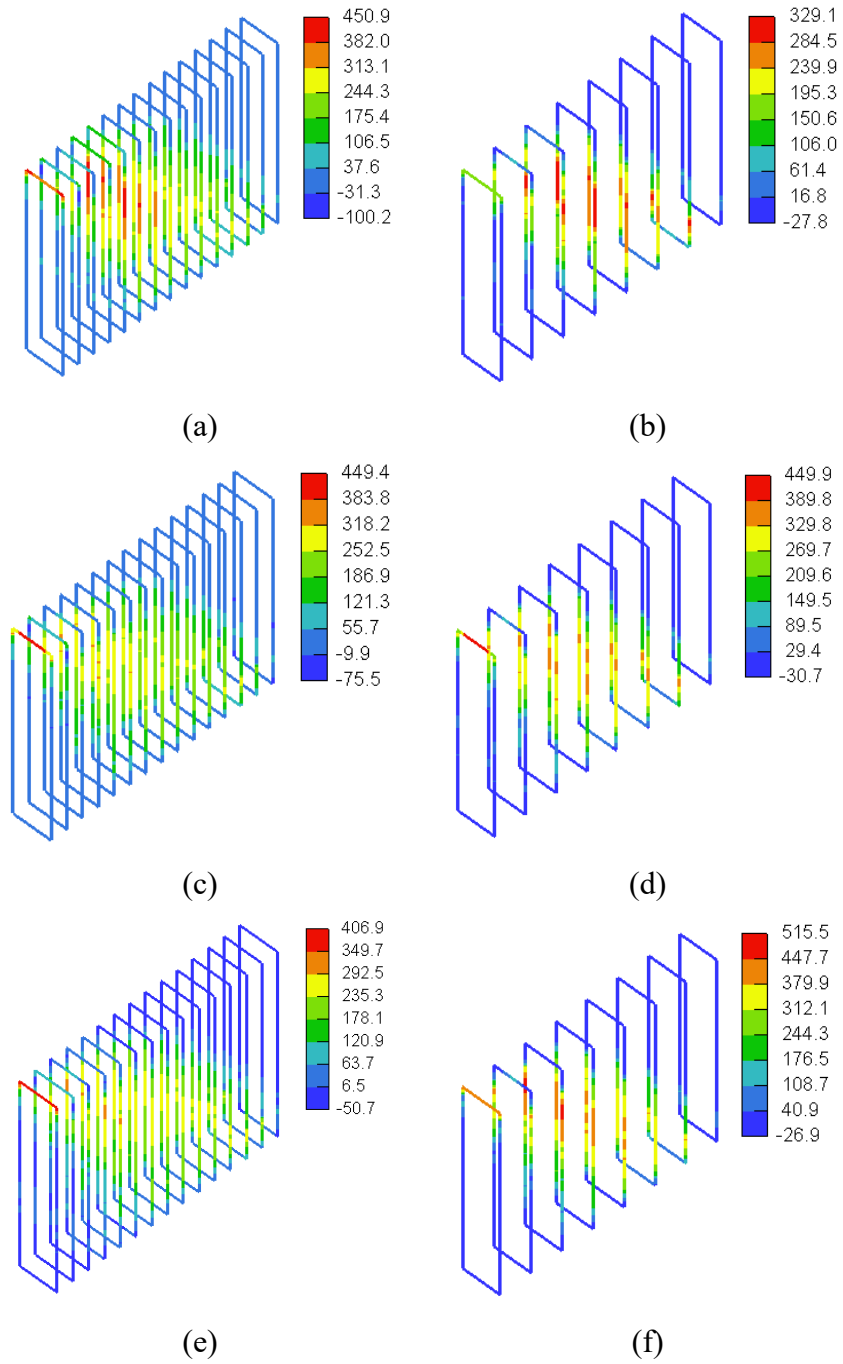
Figure 4.15: 3D view of stresses in GFRP bars for models with *a/h* = 1.0 (MPa): (a) SDB-1.0-L100; (b) SDB-1.0-L200; (c) SDB-1.0-M100; (d) SDB-1.0-M200; (e) SDB-1.0-H100; (f) SDB-1.0-H200

60
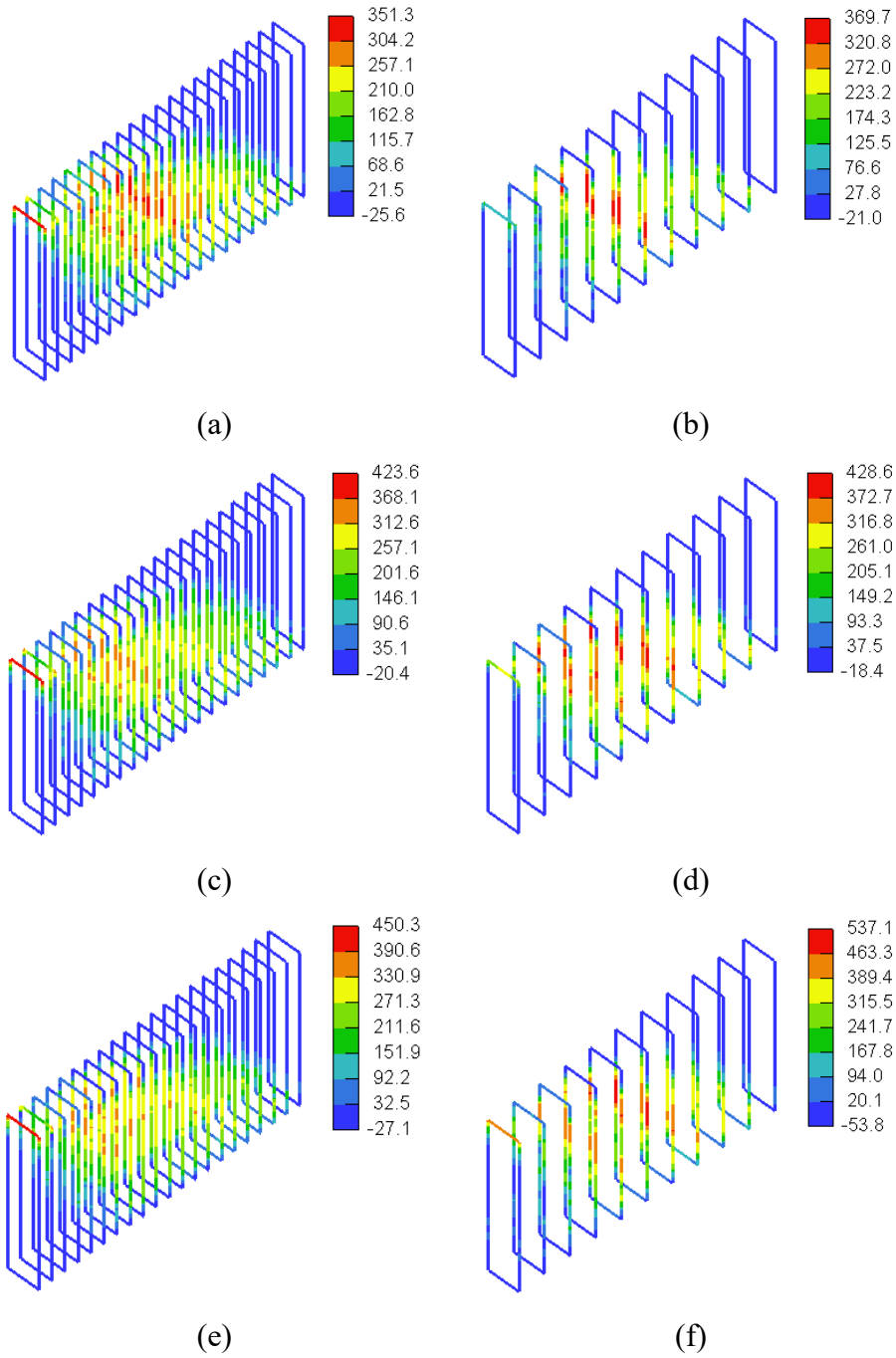
Figure 4.16: 3D view of stresses in GFRP bars for models with *a/h* = 1.5 (MPa): (a) SDB-1.5-L100; (b) SDB-1.5-L200; (c) SDB-1.5-M100; (d) SDB-1.5-M200; (e) SDB-1.5-H100; (f) SDB-1.5-H200

Figures 4.17 and 4.18 show stresses in the horizontal web reinforcement predicted numerically for the beam models with $a/h = 1.0$ and $a/h = 1.5$, respectively. None of the horizontal web reinforcing bars reached their tensile strength. The maximum stress in the horizontal GFRP bars was on average 304 MPa (26% of the tensile strength of straight GFRP bars) for the beam models with $a/h = 1.0$ and 334 MPa for the beam models with $a/h = 1.5$ (28% of the tensile strength of straight GFRP bars). The stresses in the horizontal web reinforcement at peak load tended to increase with an increase in the concrete compressive strength and the amount of web reinforcement. Increasing the concrete compressive strength and/or amount of web reinforcement allowed the beam models to sustain higher loads prior to ultimate load, thus allowing the horizontal GFRP reinforcement to contribute further to the shear capacity through sustaining additional stresses prior to ultimate load. Figures 4.19 and 4.20 show stresses in the tensile flexural reinforcement predicted numerically for the beam models with $a/h = 1.0$ and $a/h = 1.5$, respectively. The tensile flexural reinforcing bars did not reach the tensile strength of straight GFRP bars in any of the models. The stress in the flexural reinforcement was almost uniform within the shear span, except in the region very close to the upper plate and beyond which showed reduced GFRP stresses. The uniform stress distribution of the GFRP in the shear span is ascribed to the arch-action effect, in which the flexural reinforcing bars act as a tie. The maximum stress in the flexural GFRP bars was on average 378 MPa (38% of the tensile strength of straight GFRP bars) for the beam models with $a/h = 1.0$ and 388 MPa for the beam models with $a/h = 1.5$ (39% of the tensile strength of straight GFRP bars). The beam models with the higher concrete compressive strength exhibited higher GFRP stresses at peak load. The delayed failure of the beam models with the higher concrete compressive strength allowed the beam to sustain additional loads and induce extra stresses in the flexural GFRP vars prior to ultimate load.
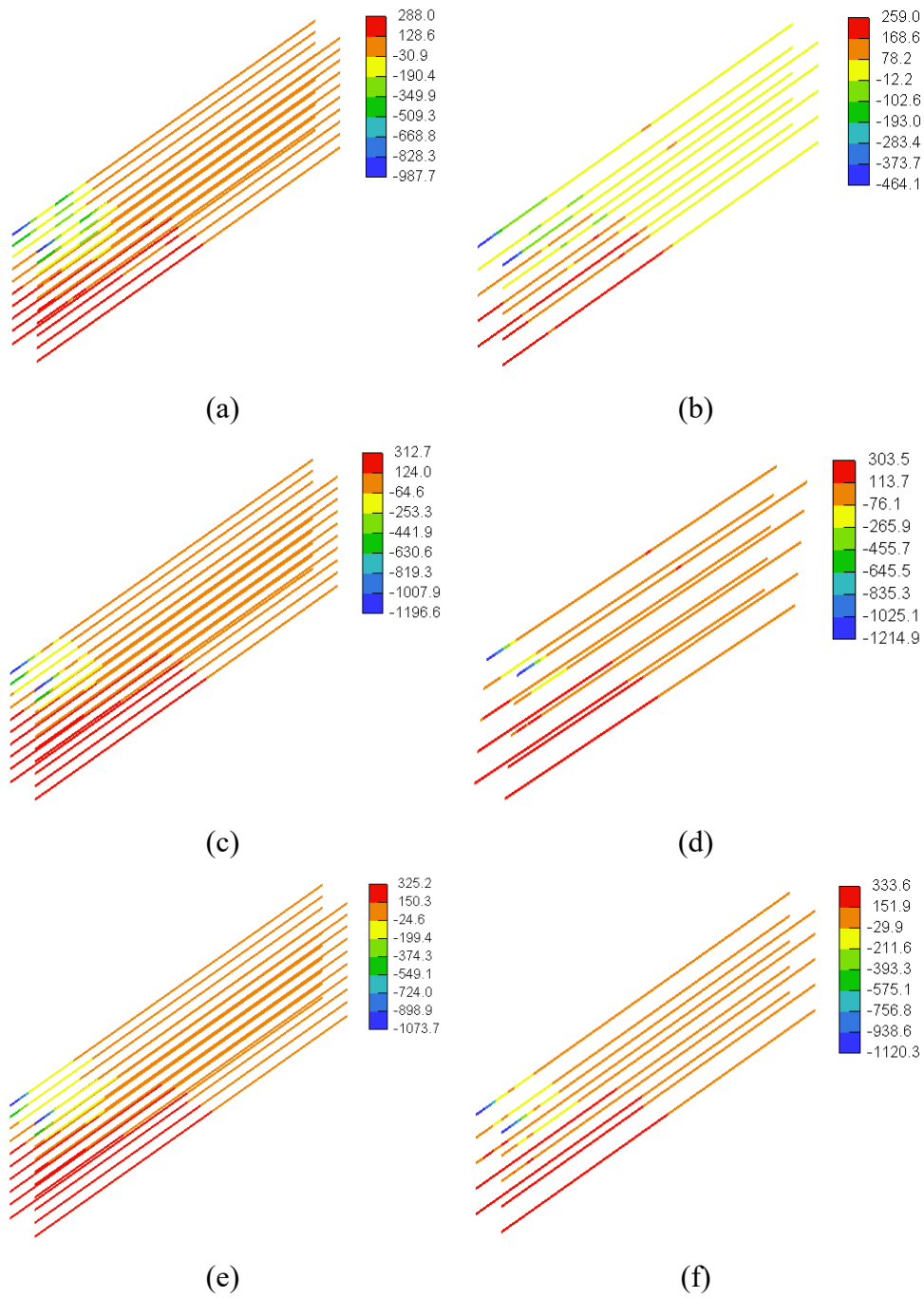
Figure 4.17: Stresses in horizontal GFRP web reinforcement for models with *a/h* = 1.0 (MPa): (a) SDB-1.0-L100; (b) SDB-1.0-L200; (c) SDB-1.0-M100; (d) SDB-1.0-M200; (e) SDB-1.0-H100; (f) SDB-1.0-H200
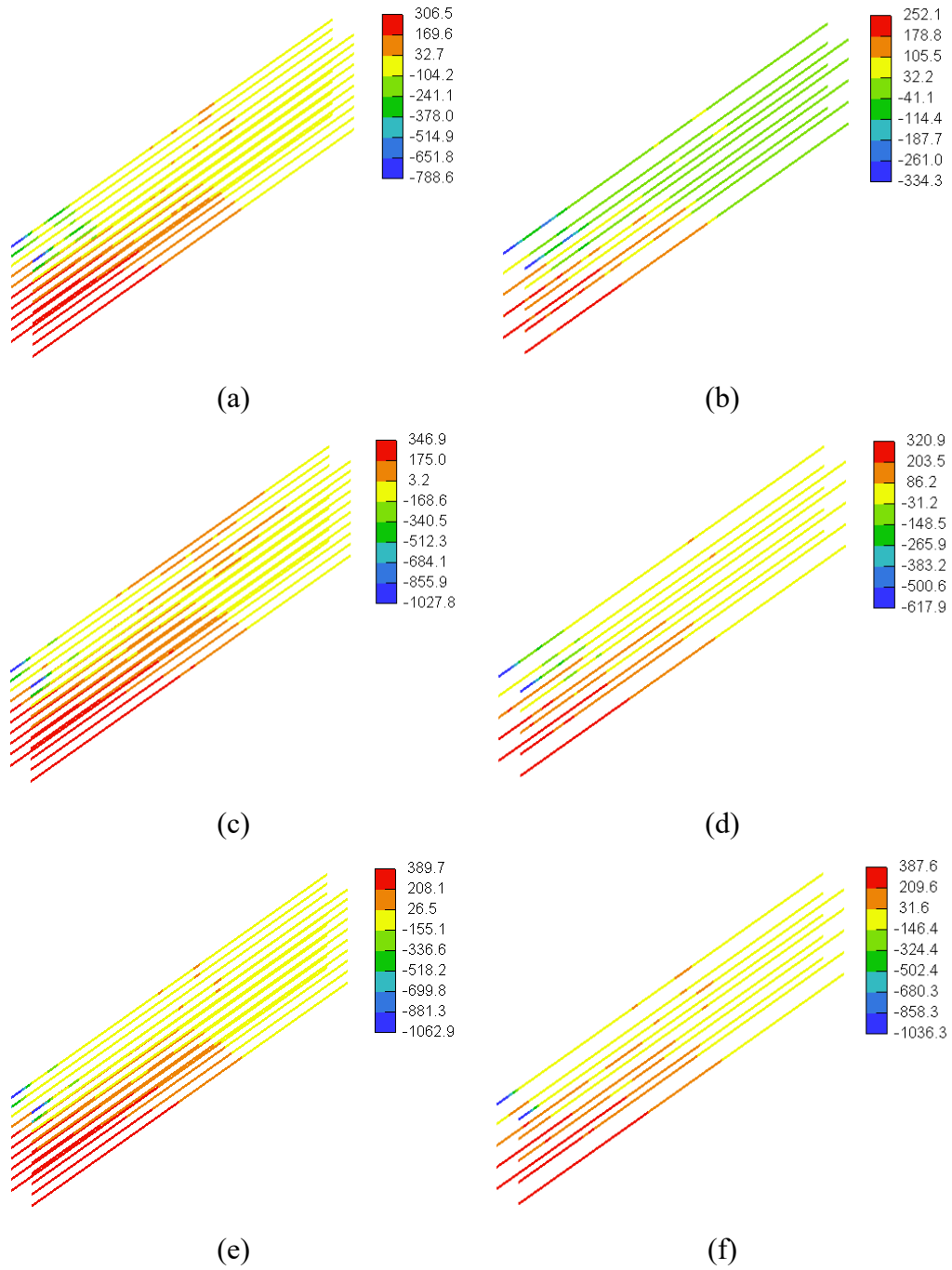
Figure 4.18: Stresses in horizontal GFRP web reinforcement for models with *a/h* = 1.5 (MPa): (a) SDB-1.5-L100; (b) SDB-1.5-L200; (c) SDB-1.5-M100; (d) SDB-1.5-M200; (e) SDB-1.5-H100; (f) SDB-1.5-H200

(a)

(b)

(c)

(d)

(e)

(f)
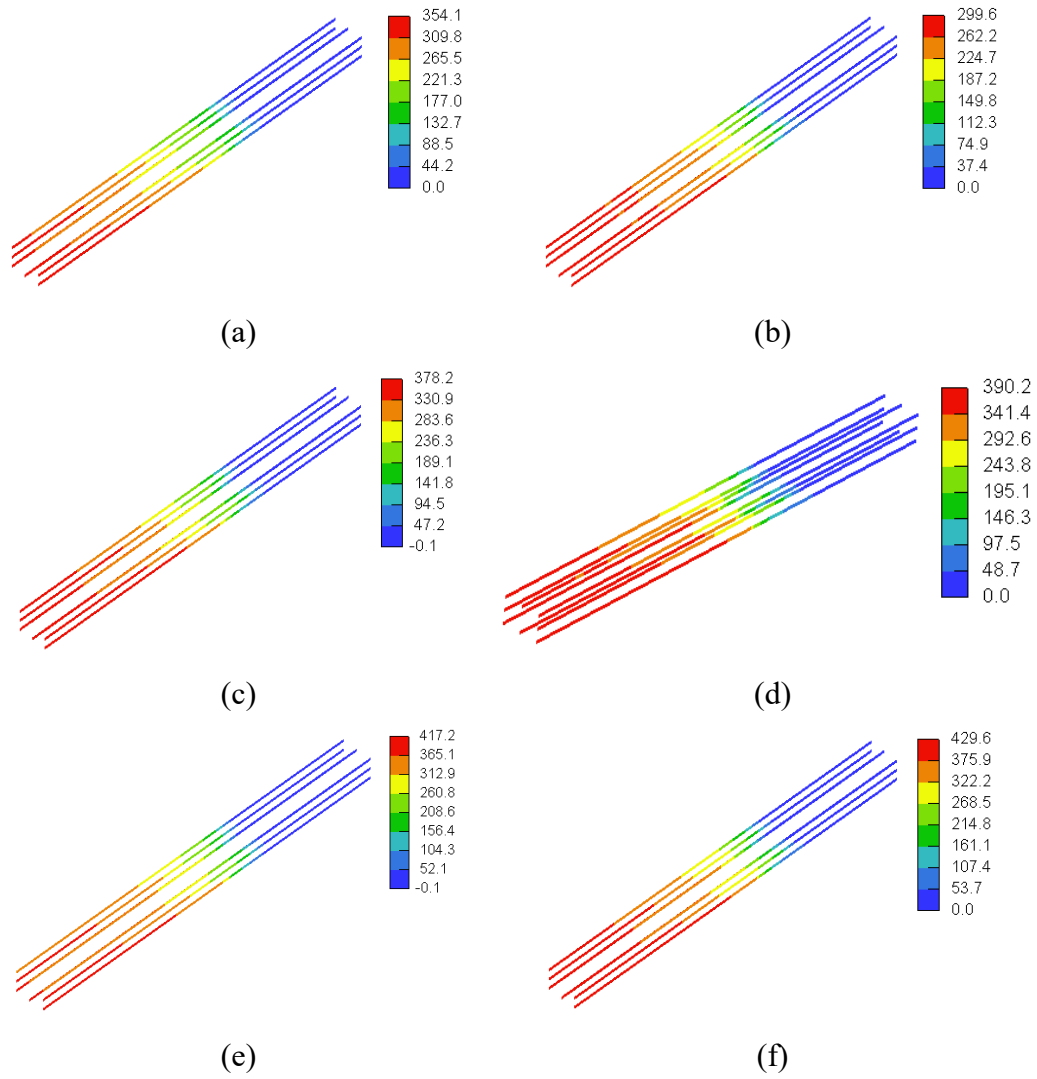
Figure 4.19: Stresses in bottom GFRP flexural reinforcement for models with *a/h* = 1.0 (MPa): (a) SDB-1.0-L100; (b) SDB-1.0-L200; (c) SDB-1.0-M100; (d) SDB-1.0-M200; (e) SDB-1.0-H100; (f) SDB-1.0-H200
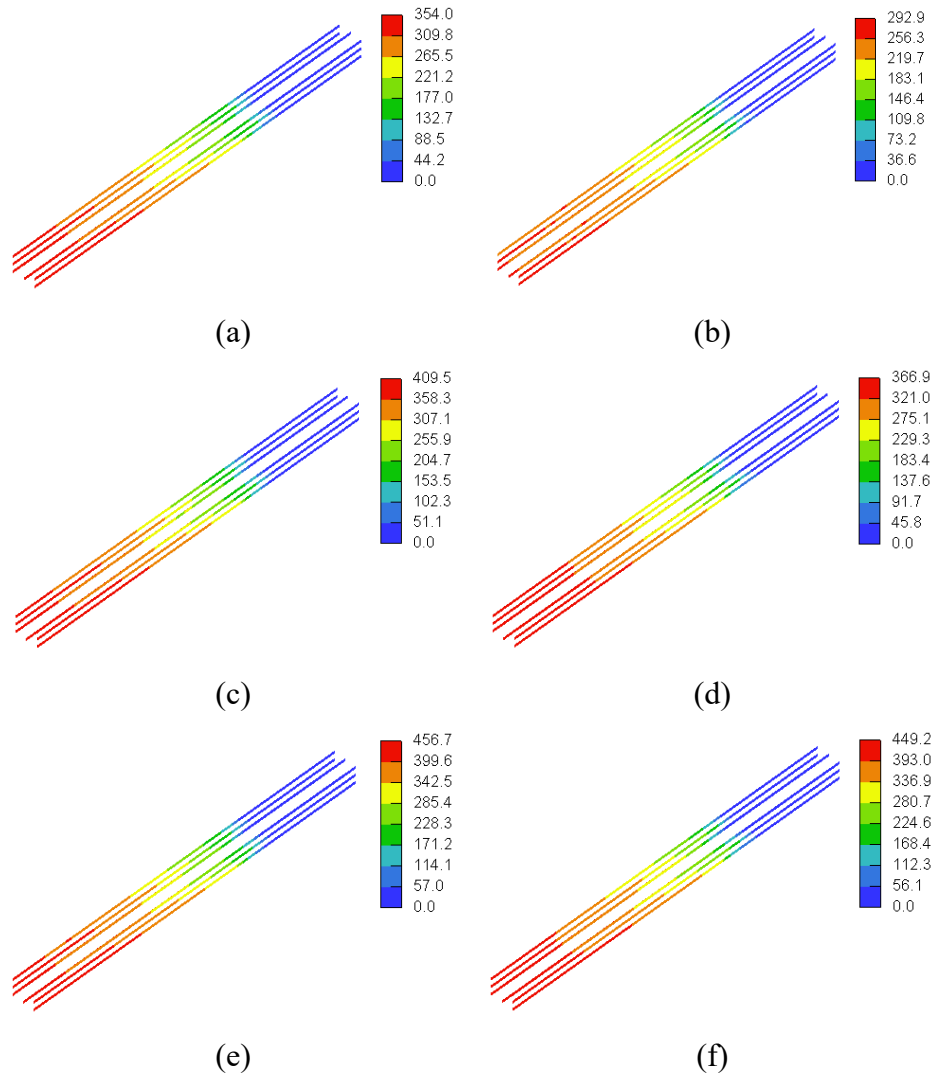
Figure 4.20: Stresses in bottom GFRP flexural reinforcement for models with *a/h* = 1.5 (MPa): (a) SDB-1.5-L100; (b) SDB-1.5-L200; (c) SDB-1.5-M100; (d) SDB-1.5-M200; (e) SDB-1.5-H100; (f) SDB-1.5-H200

4.3 Results of the Deep Beam Models Containing Openings

4.3.1 Results of the Deep Beam Models with Different Opening Sizes

4.3.1.1 Load-Deflection Response

Figures 4.21a to 4.21c show the load-deflection responses of the deep beam models with a web opening of different sizes placed in the middle of the shear span. The response of the solid deep beam model was included in the figures for the purpose of comparison. These deep beam models had the same f_c' value of 37 MPa and *a/h* value of 1.0. The variables included values of w_o/a (0.16, 0.27, and 0.32) and values of h_o/h (0.17,

0.25, and 0.33). The installation of the web opening in the middle of the shear span reduced the shear cracking load and the post-cracking stiffness relative to those of the solid deep beam model. An increase in the opening size further compromised the response of the beam models. The reductions in the cracking load and post-cracking stiffness caused by increasing the opening height were more pronounced for the models with the greater w_o/a of 0.32. The beam models with the web opening failed at a deflection significantly lower than that of the solid beam model DB-S.

(a)

(b)

(c)
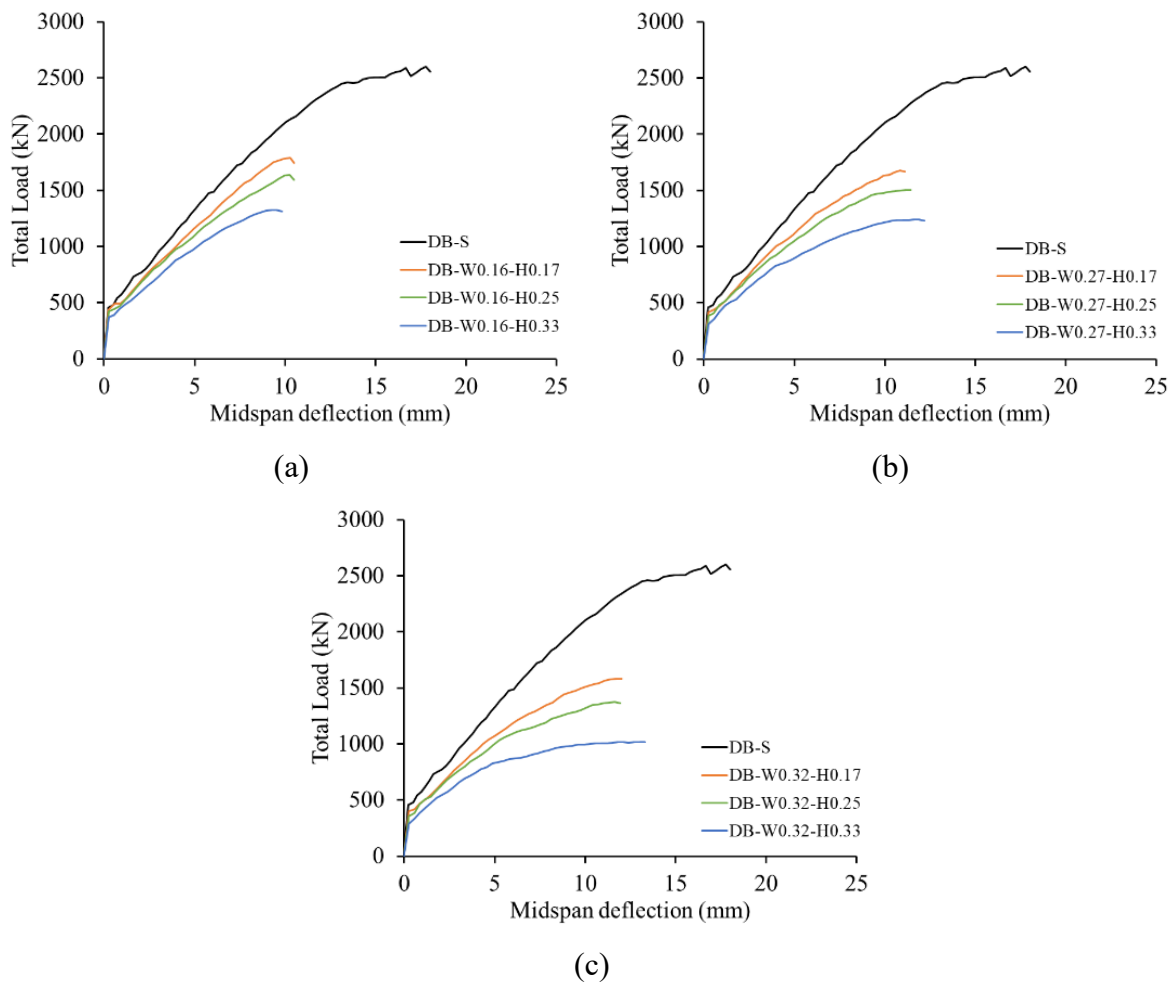
Figure 4.21: Effect of opening size on the load-deflection response: (a) $w_o/a = 0.16$; (b) $w_o/a = 0.27$; (c) $w_o/a = 0.32$

Table 4.3 presents the ultimate load and the deflection at ultimate for the beam models. At the same w_o/a of 0.16, strength reductions of 31, 37, and 49% were recorded for the deep beam models with h_o/h values of 0.17, 0.25, and 0.33, respectively. The strength reduction caused by increasing the opening height was more pronounced at the

greater w_o/a values. At w_o/a of 0.27, strength reductions of 35, 42, and 52% were recorded for the deep beam models with h_o/h values of 0.17, 0.25, and 0.33, respectively. At w_o/a of 0.32, strength reductions of 39, 47, and 61% were recorded for the deep beam models with h_o/h values of 0.17, 0.25, and 0.33, respectively. Although the deflection capacity of the beam models with a web opening was significantly lower than that of the solid deep beam model, changing the opening size had a minor impact on the deflection capacity. The deflection capacity of the beam models with different opening heights were insignificantly different. Increasing the opening width tended, however, to slightly increase the deflection capacity. The deflection capacity of the beam models with w_o/a values of 0.16, 0.27, and 0.32 were 56, 64, and 68% of that of the solid beam model DB-S. The strength of the beam models with web openings was normalized to that of the solid beam model DB-S, and then plotted against the opening size in Figure 4.22. It is evident that the strength of the beam models decreased with an increase in either the opening width or height. The rate of the strength reduction was more significant when the value of w_o/a increased from 0.27, and 0.32 (Figure 4.22a). Similarly, the strength degraded at a higher rate when the value of h_o/h increased from 0.25, and 0.33 (Figure 4.22b). The rate of the strength reduction caused by increasing the opening height (Figure 4.22b) was, however, more significant than that produced by increasing the opening width (Figure 4.22a).

Table 4.3: Numerical results of the deep beam models with different opening sizes

a/h	f_c'	Opening Size (mm)		Model Designation	Ultimate Load (kN)	Deflection at Ultimate (mm)
		w_o	h_o			
1.0 (a = 1250 mm)	37	-	-	DB-S	2601	17.8
		200	200	DB-W0.16-H0.17	1789	10.3
			304	DB-W0.16-H0.25	1637	10.3
			400	DB-W0.16-H0.33	1327	9.5
		340	200	DB-W0.27-H0.17	1678	10.8
			304	DB-W0.27-H0.25	1504	11.2
			400	DB-W0.27-H0.33	1239	11.9
		400	200	DB-W0.32-H0.17	1585	11.7
			304	DB-W0.32-H0.25	1374	11.7
			400	DB-W0.32-H0.33	1019	13.0
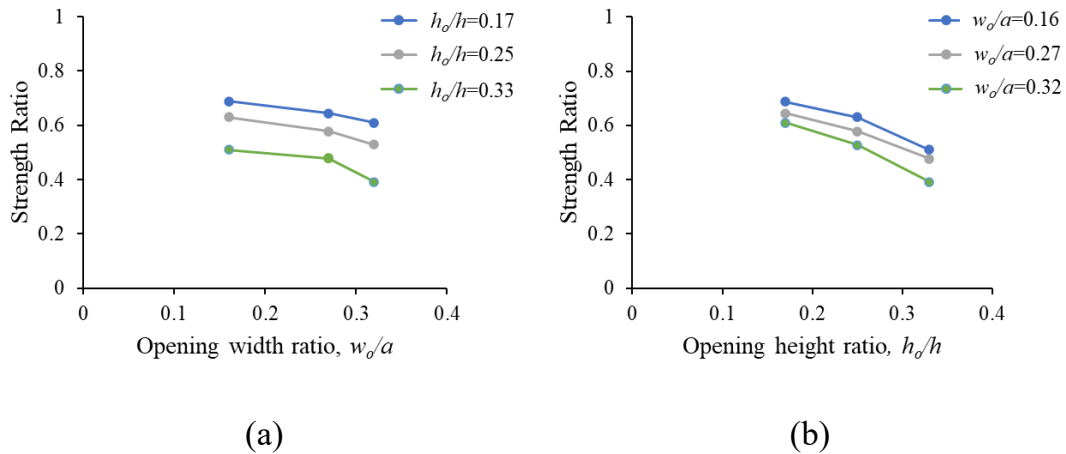
Figure 4.22: Effect of the opening size on the strength: (a) effect of the opening width; (b) effect of the opening height

4.3.1.2 Crack Pattern and Failure Mechanism

Figure 4.23 to 4.25 show the crack development and propagation at different stages of loading along with the final pattern for sample deep beam models having a web opening in the middle of the shear span. The crack patterns of all beam models at peak load are provided in Appendix A.3. The first crack in all beam models of this groups initiate at the opening corners closer to the support and load points. As the load progressed, these cracks propagated diagonally toward the support and load plates. Flexural cracks were also initiated at the midspan and within the shear span during loading, noting that the beam models DB-W0.32-H0.25 and DB-W0.32-H0.33 with the large web opening exhibited no or very few flexural cracks at a load value less than 50% of their peak loads. Further increase in the load resulted in the development of additional shear crack in the top and bottom chords causing a band of shear cracks below and above the opening. The final failure was dependent on the opening size. The deep beam models with the opening widths of 200 and 340 mm having respective w_o/a values of 0.16 and 0.27 failed due fracture of the concrete along the lower load path connecting the edge of the support plate and the opposite corner of the opening in the bottom chord along with excessive widening of the shear crack at the opening corner. In most of the deep beam models with w_o/a values of 0.16 and 0.27, extensive shear cracks were also developed along the upper load path in the top chord connecting the edge of the load plate to the

opposite corner of the opening causing failure along the upper load path simultaneously with that occurred along lower load path. It is noteworthy that the lower load path is vulnerable to fail before the upper load path because of the transverse strains caused by the stresses in the flexural tensile reinforcement at the bottom of the beam model. In contrast, the deep beam models with the opening width of 400 mm having a respective w_o/a of 0.32 failed due excessive widening of shear cracks at the opening corners closer to the load and support plates along with excessive rotation that occurred in the top and bottom chords.

(a) (b)

(c) (d)
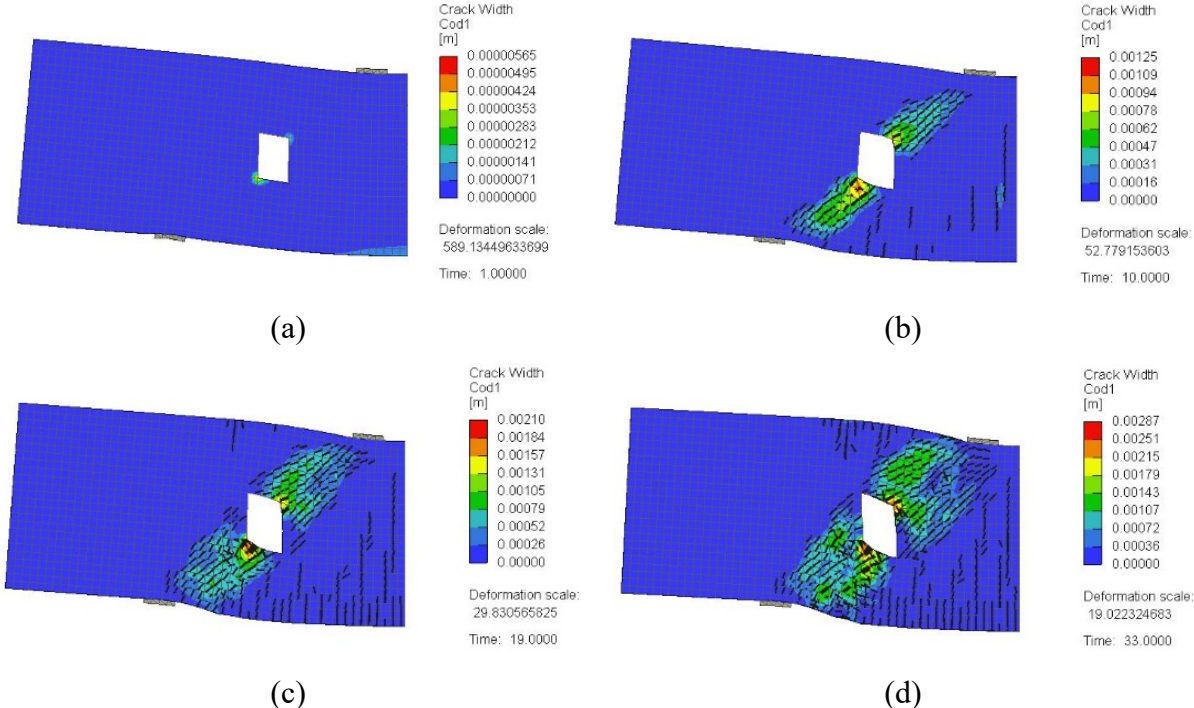
Figure 4.23: Crack pattern for a typical model failed along the lower load path (DB-W0.16-H0.25): (a) at 25% of peak load; (b) at 50% of peak load; (c) at 75% of peak load; (d) at 100% of peak load
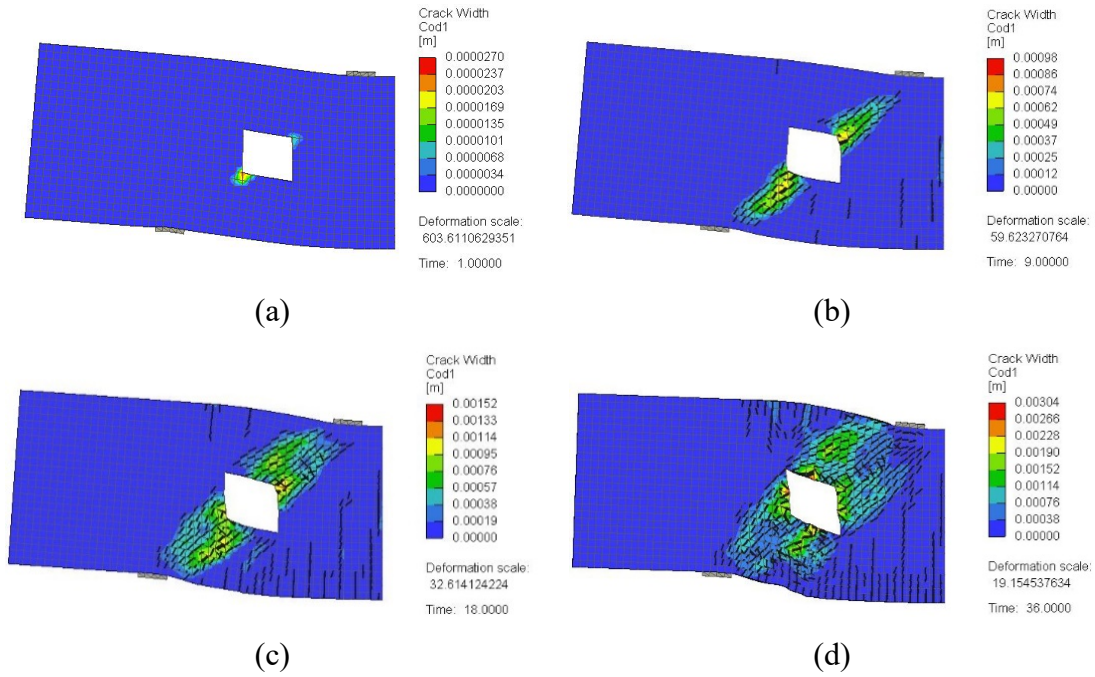
Figure 4.24: Crack pattern for a typical model failed along the lower and upper load path (DB-W0.27-H0.25): (a) at 25% of peak load; (b) at 50% of peak load; (c) at 75% of peak load; (d) at 100% of peak load
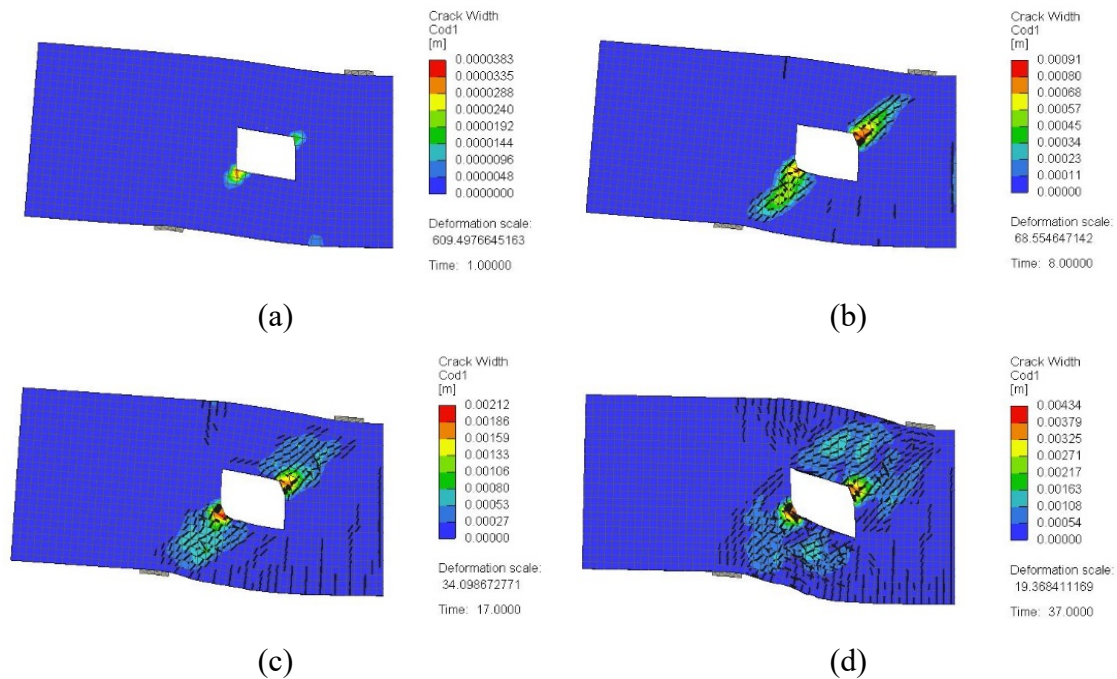
Figure 4.25: Crack pattern for a typical model failed due to an excessive widening of shear cracks at the opening corners (DB-W0.32-H0.25): (a) at 25% of peak load; (b) at 50% of peak load; (c) at 75% of peak load; (d) at 100% of peak load

4.3.1.3 GFRP Stresses

General 3D views of the stresses in the vertical GFRP stirrups predicted numerically for the beam models of this group are shown in Figures 4.26 to 4.28. For the beam models with the smaller w_o/a value of 0.16, the maximum stresses in the vertical GFRP stirrups were in the straight portions of the stirrup near the corner of the web opening closer to the support plate (Figure 4.26). The maximum GFRP stress at peak load for DB-W0.16-H0.17 with $w_o/a = 0.16$ and $h_o/h = 0.17$ was 48% of the tensile strength of straight GFRP bars. The respective value for the other two models with the greater h_o/h values of 0.25 and 0.33 was, on average, 57% of the tensile strength of straight GFRP bars. For the beam models with $w_o/a = 0.27$, the maximum stresses in the vertical GFRP stirrups were in the straight portions of the stirrup near both corners of the web opening closer to the support and load plates (Figure 4.27). The maximum GFRP stresses at peak load for the beam models with $w_o/a = 0.27$ and h_o/h of 0.17, 0.25, and 0.33 were 42, 47, and 54% of the tensile strength of straight GFRP bars, respectively. These results indicate that the vertical GFRP bars at the sides of the opening exhibited higher stresses in the beam models with the greater opening height. The beam models with the greatest w_o/a value of 0.32, the maximum stresses in the vertical GFRP stirrups were in the straight portions of the stirrup near the corner of the web opening closer to the support plate, except for DB-W0.32-H0.17, which exhibited maximum GFRP stresses at both corners of the web opening (Figure 4.28). The maximum GFRP stresses at peak load for the beam models with w_o/a of 0.32 were in the range of 34 to 42% of the tensile strength of straight GFRP bars, and they also tended to increase with an increase in the opening height. In contrast, when the GFRP stresses in the vertical stirrups of the beam models having the same opening height and different opening widths, it can be seen that the stresses in the vertical GFRP stirrups at the sides of the opening decreases with an increase in the opening width. This behavior could be due to an increased transfer of shear stresses through the upper and lower chords for the beam models with the greater opening width. It is noteworthy that the stresses in the bottom portion of the vertical legs of the GFRP stirrup placed at the side of the opening closer to the support plate in most of the beam models with w_o/a of 0.16 and 0.27 was in the range of 90 to 100% of the tensile strength of the bent portion of GFRP bars for the beam models.

72

These results implied possible rupture of these vertical GFRP stirrups at the bent portions in most of the beam models with w_o/a of 0.16 and 0.27. For the beam models with the greater w_o/a of 0.32, the stresses in the vertical GFRP bars were below the rupture strength of the bent portions of the GFRP bars.

(a)   (b)   (c)
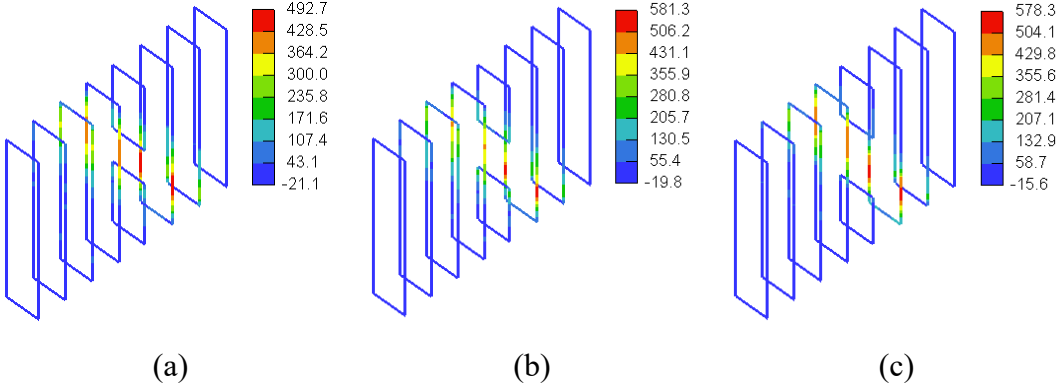
Figure 4.26: 3D view of stresses in GFRP bars for models with w_o/a = 0.16 (MPa): (a) DB-W0.16-H0.17; (b) DB-W0.16-H0.25; (c) DB-W0.16-H0.33

(a)   (b)   (c)

Figure 4.27: 3D view of stresses in GFRP bars for models with w_o/a = 0.27 (MPa): (a) DB-W0.27-H0.17; (b) DB-W0.27-H0.25; (c) DB-W0.27-H0.33

(a)   (b)   (c)

Figure 4.28: 3D view of stresses in GFRP bars for models with w_o/a = 0.32 (MPa): (a) DB-W0.32-H0.17; (b) DB-W0.32-H0.25; (c) DB-W0.32-H0.33

None of the horizontal web reinforcing bars or the flexural reinforcement at tension side in the deep beam models of this group reached their tensile strength. The stresses in the horizontal web reinforcement and tensile flexural reinforcement predicted numerically for the beam models of this group are shown in Figures 4.29 to 4.34. For the beam models with the smaller w_o/a value of 0.16, the maximum stresses in the horizontal web reinforcement were on average 258 MPa, which corresponded to 22% of the tensile strength of the GFRP bars (Figure 4.29). The maximum stress in their tensile flexural reinforcement ranged from 190 to 249 MPa, which correspond to 19 to 25% of the tensile strength of the GFRP bars (Figure 4.30). The beam models with the w_o/a value of 0.27 exhibited maximum stresses of 240 to 348 MPa (i.e., 21 to 30% of the tensile strength of the GFRP bars) in the horizontal web reinforcement and 200 to 236 MPa (i.e., 20 to 24% of the tensile strength of the GFRP bars) in the tensile flexural reinforcement as shown in Figures 4.31 and 4.32, respectively. The beam models with the w_o/a value of 0.32 exhibited maximum stresses of 324 to 382 MPa (i.e., 27 to 38% of the tensile strength of the bars) in the horizontal web reinforcement and 169 to 226 MPa (i.e., 17 to 23% of the tensile strength of the GFRP bars) in the tensile GFRP flexural reinforcement as shown in Figures 4.33 and 4.34, respectively. These results indicate that for the beam models with the web opening in the middle of the shear span, varying the opening size had insignificant effect on the maximum stresses of the horizontal web reinforcement and tensile flexural reinforcement recorded at peak load. Generally, the maximum stresses recorded in the horizontal web reinforcement were in the range of 21 to 38% of the GFRP tensile strength, whereas those of the tensile flexural reinforcement were in the range of 19 to 25% of the GFRP tensile strength.

(a)　　　　　　　　　　　(b)　　　　　　　　　　　(c)
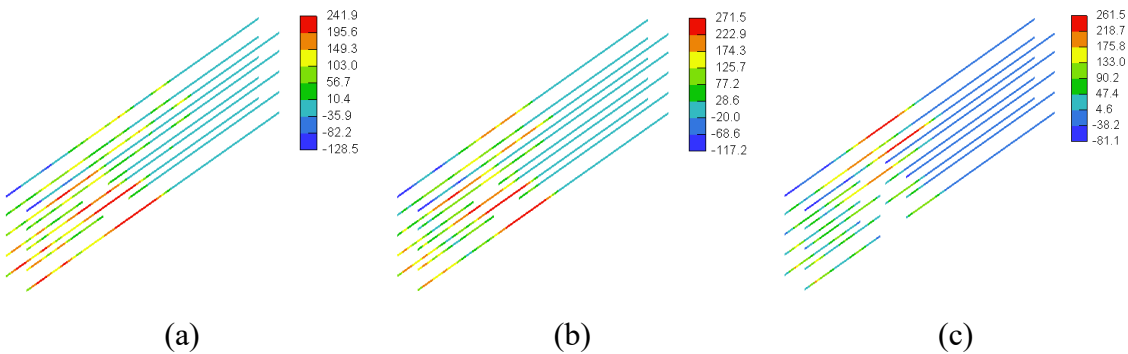
Figure 4.29: Stresses in horizontal GFRP web reinforcement for models with $w_o/a = 0.16$ (MPa): (a) DB-W0.16-H0.17; (b) DB-W0.16-H0.25; (c) DB-W0.16-H0.33

(a)   (b)   (c)
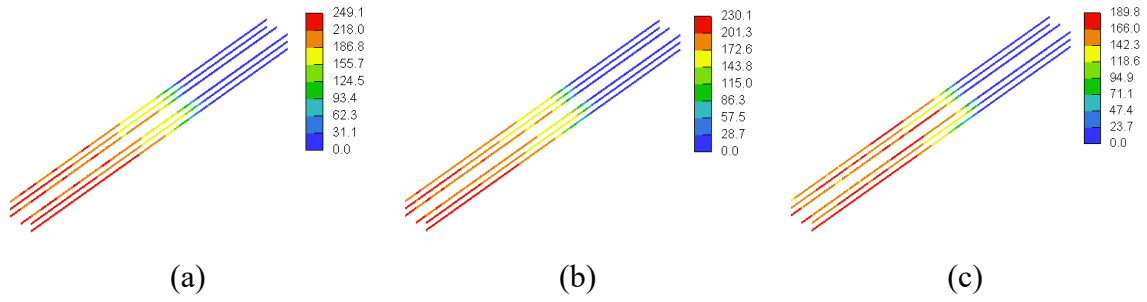
Figure 4.30: Stresses in bottom GFRP flexural reinforcement for models with w_o/a = 0.16 (MPa): (a) DB-W0.16-H0.17; (b) DB-W0.16-H0.25; (c) DB-W0.16-H0.33

(a)   (b)   (c)
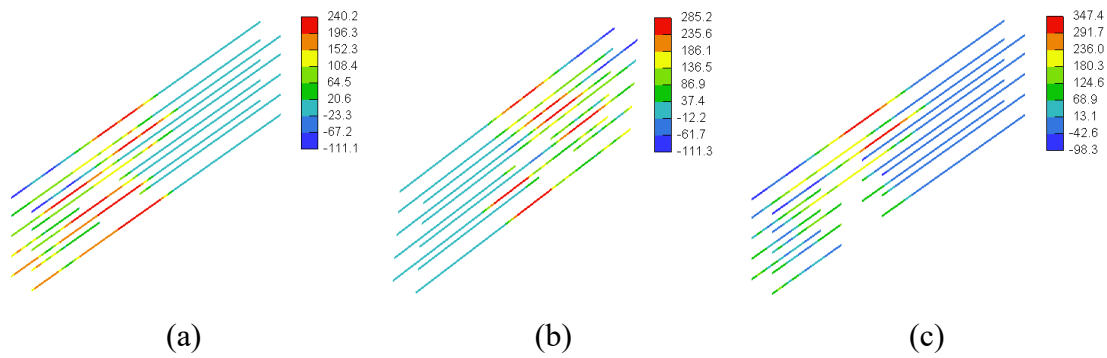
Figure 4.31: Stresses in horizontal GFRP web reinforcement for models with w_o/a = 0.27 (MPa): (a) DB-W0.27-H0.17; (b) DB-W0.27-H0.25; (c) DB-W0.27-H0.33

(a)   (b)   (c)
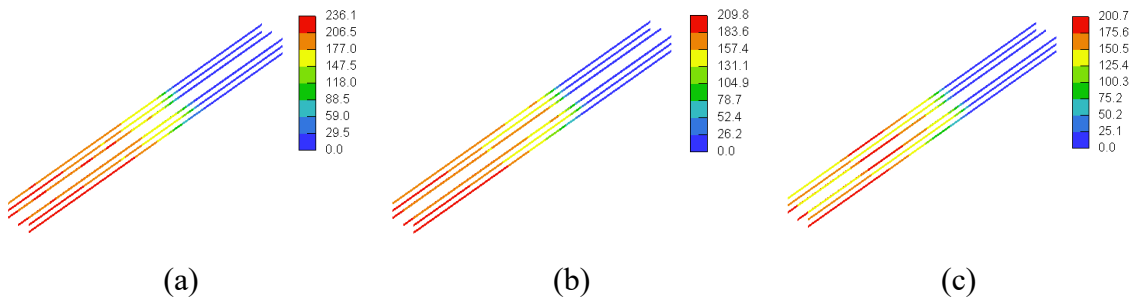
Figure 4.32: Stresses in bottom GFRP flexural reinforcement for models with w_o/a = 0.27 (MPa): (a) DB-W0.27-H0.17; (b) DB-W0.27-H0.25; (c) DB-W0.27-H0.33

(a)   (b)   (c)
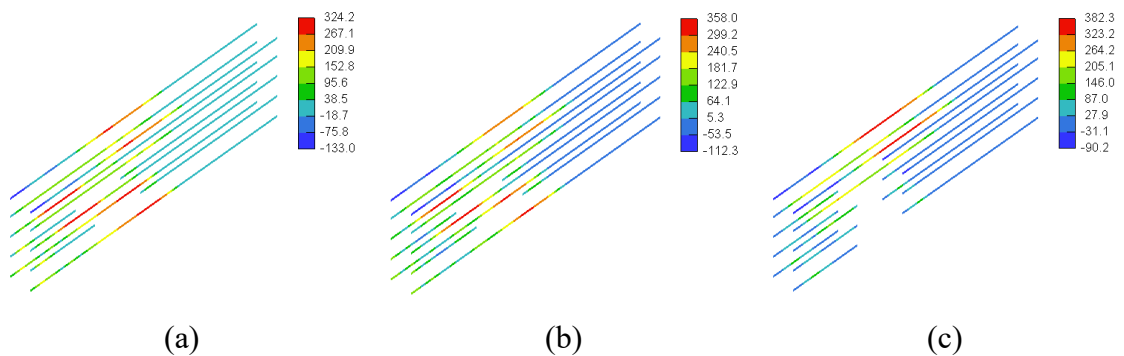
Figure 4.33: Stresses in horizontal GFRP web reinforcement for models with w_o/a = 0.32 (MPa): (a) DB-W0.27-H0.17; (b) DB-W0.27-H0.25; (c) DB-W0.27-H0.33
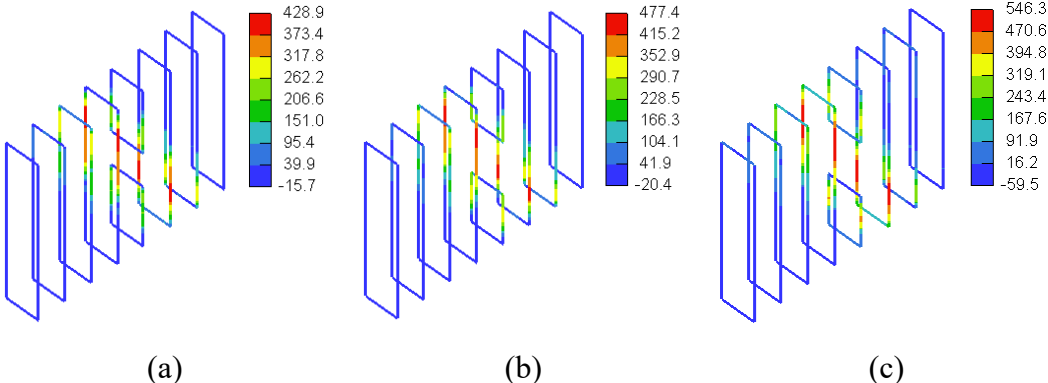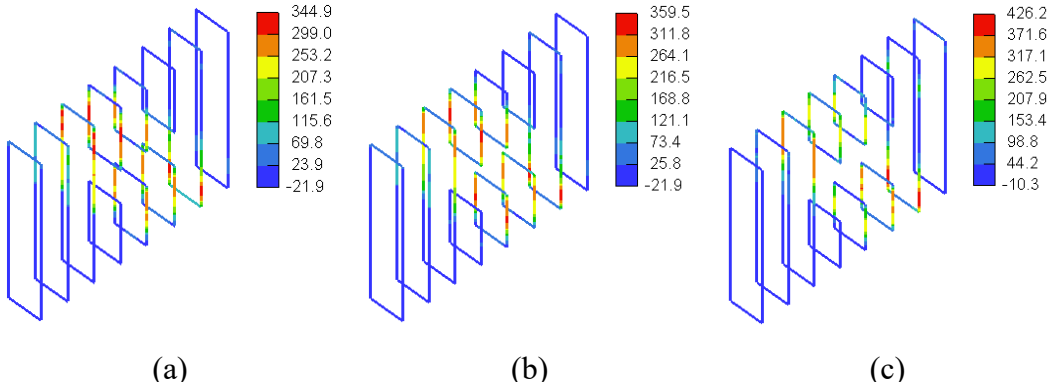
75
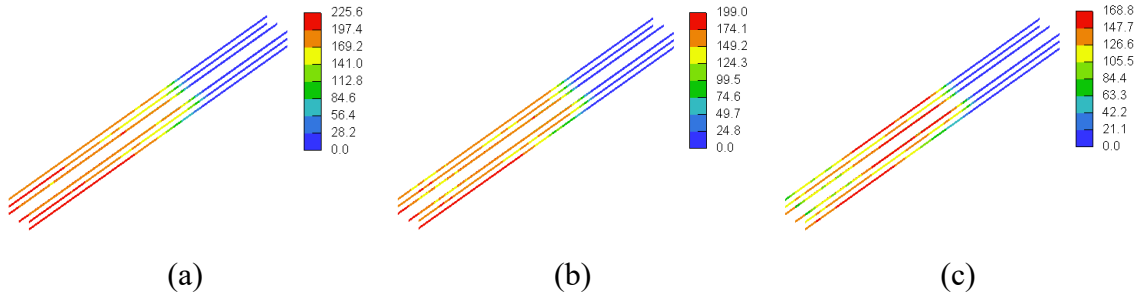
Figure 4.34: Stresses in bottom GFRP flexural reinforcement for models with $w_o/a = 0.32$ (MPa): (a) DB-W0.32-H0.17; (b) DB-W0.32-H0.25; (c) DB-W0.32-H0.33

4.3.2 Results of the Deep Beam Models with Different Opening Locations

The deep beam models of this group had the same f_c' value of 37 MPa, a/h value of 1.0, and a web opening size of $w_o = 340$ mm and $h_o = 304$ mm (i.e., $w_o/a = 0.27$ and $h_o/h = 0.25$). The primary variable of this group was the location of the web opening. The center of the web opening was located at a distance x_o from the face of the support plate and y_o from the bottom soffit of the beam model. The location of the center of the opening in the horizontal and vertical directions were normalized to the clear shear span (X_c) and the beam depth (h), respectively. Values of the term x_o/X_c were 0.25, 0.50, and 0.75, whereas those of the term y_o/h were 0.33, 0.50, and 0.75.

4.3.2.1 Load-Deflection Response

Figures 4.35a to 4.35c show the load-deflection responses of the deep beam models with a web opening having x_o/X_c of 0.25, 0.50, and 0.75 respectively. The response of the solid deep beam model DB-S was included in the figures for the purpose of comparison. Figure 4.35a shows that installation of the web opening near the support at x_o/X_c of 0.25 seriously impaired the response of the beam models. The detrimental effect of the web opening was more pronounced for the beam models DB-X0.25-Y0.33 and DB-X0.25-Y0.50 with the lower y_o/h values of 0.33 and 0.50, respectively, because the opening in these two models fully interrupted the natural load path. The web opening in the beam model DB-X0.25-Y0.75 did not interrupt the natural load path, and hence, its post-cracking stiffness was almost same as that of the DB-S. The beam model DB-X0.25-Y0.75 failed, however, at lower load and deflection capacities than those of DB-S. Although, the web opening in DB-X0.25-Y0.75 did not interrupt the natural load path,

76

it could have affected the width of the middle portion of a bottled-shaped strut that could have formed in the shear span. In addition, placing the web opening in the compression zone above the natural load path hindered transfer of the load to the support through other struts formed above the natural load path. Figure 4.35b shows that the behavior of the beam models with the web opening installed at x_o/X_c of 0.50 was affected by the location of the center of the opening with respect to the bottom face of the beam (y_o). Although the behavior of all models was inferior to that of the solid deep beam model DB-S, the degradation in the behavior intensified with an increase in the distance between the center of the opening and the bottom face of the beam. These results indicate that placing the web opening above the natural load path was more detrimental to the structural behavior than placing it below the natural load path. The presence of a web opening in the compression zone above the natural load path hindered formation of struts in this region, and hence, compromised the structural response. Figure 4.35c shows that the behavior of the beam models with the web opening installed at x_o/X_c of 0.75 was seriously affected by the location of the center of the opening in the vertical direction (y_o). The behavior of the beam model DB-X0.75-Y0.33 was not seriously affected by the opening since it was provided at the tension side ($y_o/h = 0.33$) away from the natural load path. In contrast, the behavior of the beam model DB-X0.75-Y0.75 with $y_o/h = 0.75$ was seriously compromised since the opening was very close to the load plate and fully interrupted the natural load path. The behavior of the beam model DB-X0.75-Y0.50 with $y_o/h = 0.50$ almost coincided with that of DB-X0.75-Y0.33 with $y_o/h = 0.33$ until the load reached a value of approximately 1250 kN. Next, a degradation in the behavior of the beam model DB-X0.75-Y0.50 occurred until it failed at load and deflection capacities lower than those of DB-X0.75-Y0.33. It is noteworthy that a change in the slope of the load-deflection response was observed prior to reaching the ultimate load, probably because of the development of new major cracks.
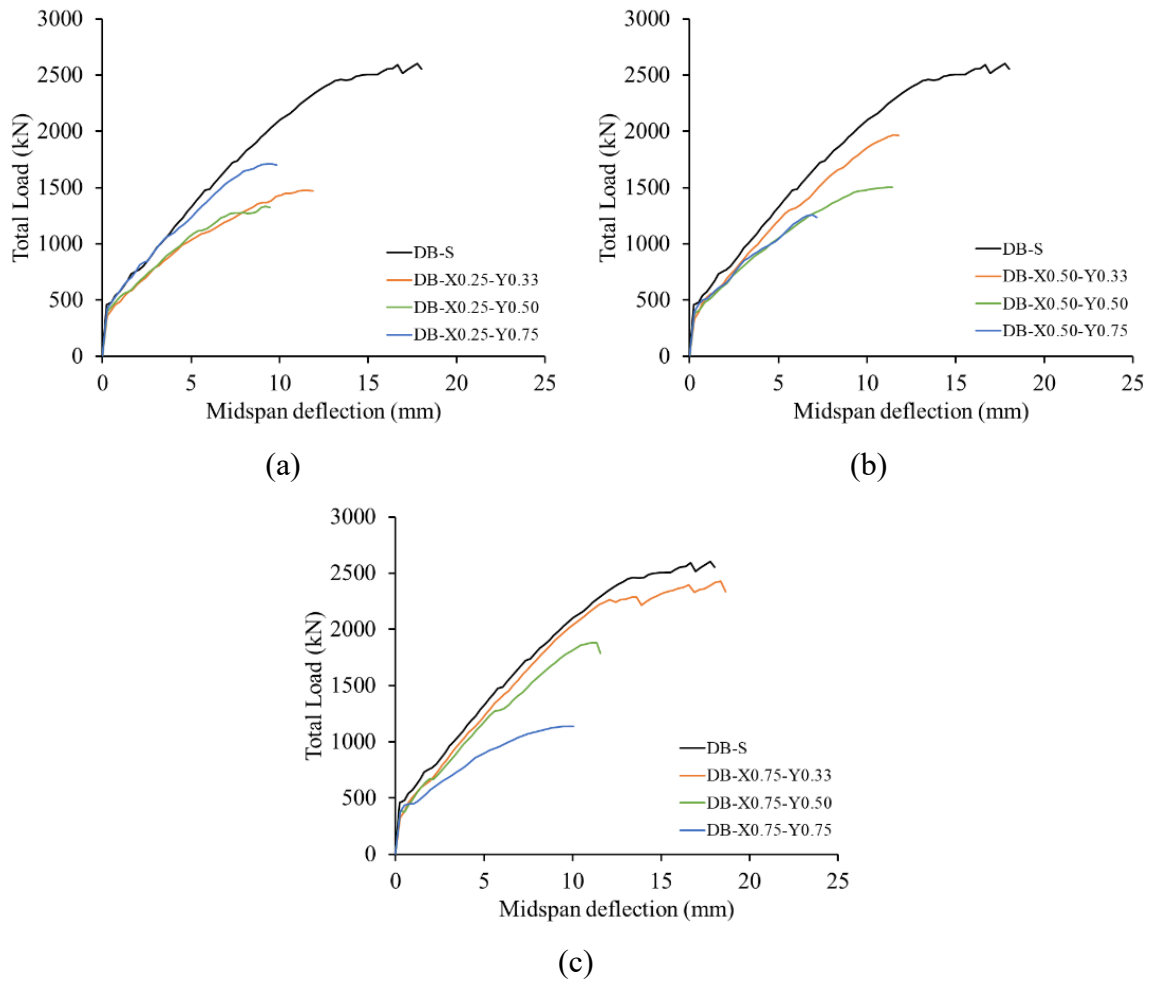
Figure 4.35: Effect of opening location on the load-deflection response: (a) $x_o/X_c = 0.25$ (b) $x_o/X_c = 0.50$; (c) $x_o/X_c = 0.75$

Table 4.4 presents the ultimate load and the deflection capacity for the beam models of this group. For the beam models having a web opening with x_o/X_c of 0.25, strength reductions of 43 and 49% were recorded for DB-X0.25-Y0.33 and DB-X0.25-Y0.50 having y_o/h values of 0.33 and 0.50, respectively. It is noteworthy that the web opening in DB-X0.25-Y0.33 and DB-X0.25-Y0.50 fully interrupted the natural load path. When the opening was pushed upward away from the natural load path in DB-X0.25-Y0.75, a lower strength reduction of 34% was recorded. The deflection capacity of the beam models containing a web opening with x_o/X_c of 0.25 was, on average 57% of that of DB-S. For the beam models having a web opening with x_o/X_c of 0.50, strength reductions of 24, 42, and 52% were recorded for DB-X0.50-Y0.33, DB-X0.50-Y0.50, and DB-X0.50-Y0.75 having y_o/h values of 0.33, 0.50, and 0.75, respectively. These results indicate that the strength reduction was intensified with an increase in the

78

distance between the center of the opening and the bottom face of the beam, noting that the opening in these three models fully interrupted the natural load path. The reduction in the ultimate load was accompanied by a reduction in the corresponding deflection capacity of 35 to 61%. For the beam models having a web opening with x_o/X_c of 0.75, strength reductions of 7, 28, and 56% were recorded for DB-X0.75-Y0.33, DB-X0.75-Y0.50, and DB-X0.75-Y0.75 having y_o/h values of 0.33, 0.50, and 0.75, respectively. The beam model DB-X0.75-Y0.33 exhibited a negligible strength reduction of 7% because the web opening was in the tension side and also did not interrupt the natural load path. In contrast, the beam model DB-X0.75-Y0.75 exhibited a significant strength reduction of 56% because the web opening was in the compression zone close to the load plate and fully interrupted the natural load path. The deflection capacity of DB-X0.75-Y0.33 with y_o/h of 0.33 was almost same as that of DB-S. Conversely, the beam model DB-X0.75-Y0.75 with y_o/h of 0.75 exhibited 45% reduction in the deflection capacity relative to that of DB-S.

Table 4.4: Numerical results of the deep beam models with different opening locations

a/h	f_c'	Opening Location (mm)		Model Designation	Ultimate Load (kN)	Deflection at Ultimate (mm)
		x_o	y_o			
1.0 (a = 1250 mm)	37	-	-	DB-S	2601	17.8
		262.5	400	DB-X0.25-Y0.33	1478	11.6
			590	DB-X0.25-Y0.50	1337	9.2
			900	DB-X0.25-Y0.75	1714	9.6
		525	400	DB-X0.50-Y0.33	1971	11.5
			590	DB-X0.50-Y0.50	1504	11.2
			900	DB-X0.50-Y0.75	1259	6.9
		787.5	400	DB-X0.75-Y0.33	2429	18.4
			590	DB-X0.75-Y0.50	1881	11.4
			900	DB-X0.75-Y0.75	1139	9.7

The relationships between the strength reduction caused by the web opening and the opening location are provided in Figure 4.36. For the beam models with y_o/h of 0.33 and 0.50, the strength increased with an increase in the distance measured from the face of the support within the shear span. The strength of the beam models with y_o/h of 0.33

tended to be higher than that of their counterparts with y_o/h of 0.50, and this behavior was more evident with an increase in the distance from the face of the support plate. The beam models with y_o/h of 0.75 exhibited an opposite trend, where the strength decreased with an increase in the distance measured from the face of the support within the shear span. These results verified the detrimental effect of placing a web opening in the compression zone closer to the load plate ($x_o/X_c = 0.75$ and $y_o/h = 0.75$). The results implied also that a negligible strength reduction could be obtained when the web opening was placed in the tension side above the flexural reinforcement but away from the natural load path and the support plate ($x_o/X_c = 0.75$ and $y_o/h = 0.33$).
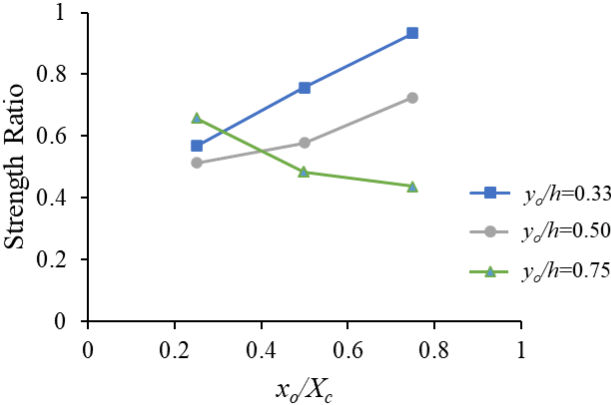
Figure 4.36: Effect of the opening location on the strength

4.3.2.2 Crack Pattern and Failure Mechanism

Figures 4.37 to 4.40 show the crack development and propagation at different stages of loading along with the final pattern for sample deep beam models of this group. The crack patterns of all beam models at peak load are provided in Appendix A.4. The beam models of this group, except those with the web opening close to the compression face of the beam ($y_o/h = 0.75$), exhibited first cracking at the opposite corner of the opening closer to the support and load points at a load value ≤ 25% of their strength. The beam models with $y_o/h = 0.75$ exhibited very few flexural cracks at 25% of the strength, whereas shear cracks were initiated at the opening corners at a load value higher than 25% of the strength. The shear cracks initiated earlier at the opening corners propagated diagonally toward the support and load plates as the load progressed. Flexural cracks were also initiated at the midspan, within the shear span, and in the bottom chord below

80

the opening. Additional shear cracks were developed with an increase in the applied load creating a band of shear cracks. The final crack pattern and failure mode was dependent on the location of the opening. The beam models with the web opening away from the natural load path (DB-X0.25-Y0.75 and DB-X0.75-Y0.33) exhibited failure of the diagonal strut connecting the load and support plates. The beam model DB-X0.75-Y0.50 failed due to extensive diagonal shear cracking crossing the opening center. Other beam models failed due to development of extensive diagonal cracks that caused simulations failure of the concrete along the upper and lower load paths or failure of the concrete along one of them combined with extensive diagonal cracks along the other load path as well as excessive widening of shear cracks at the opening corners.

(a)   (b)

(c)   (d)
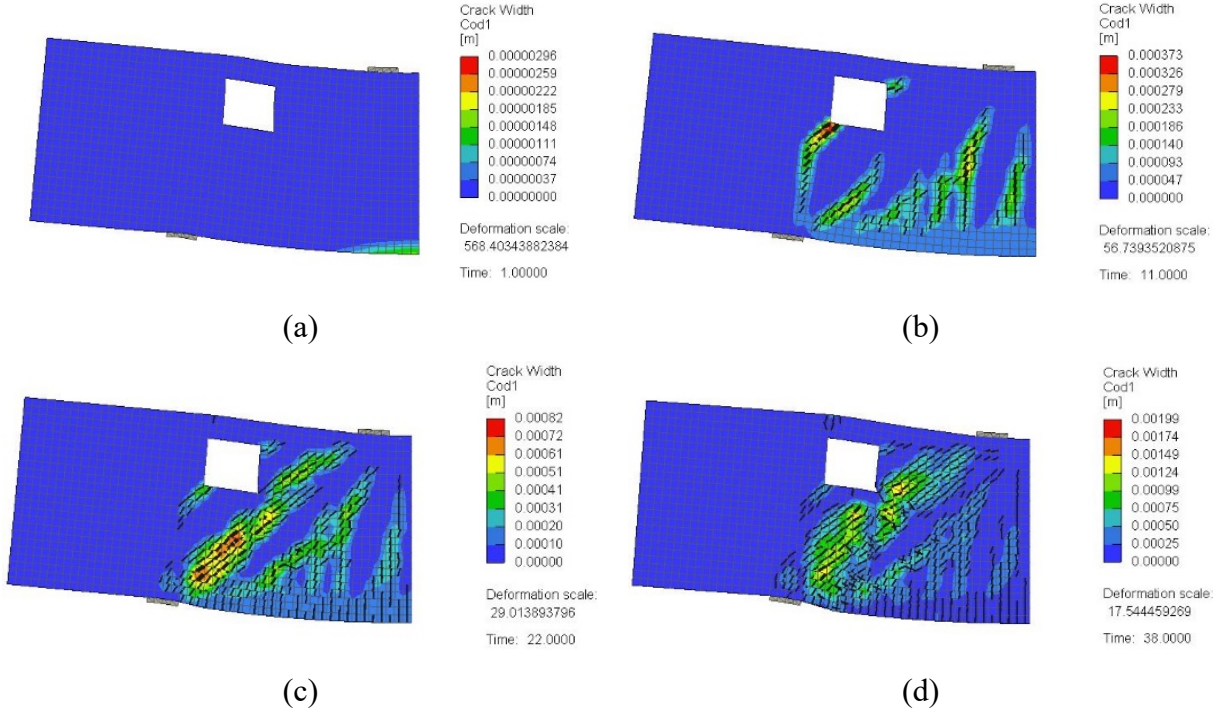
Figure 4.37: Crack pattern for a typical model failed along the strut connecting the load and support plates (DB-X0.25-Y0.75): (a) at 25% of peak load; (b) at 50% of peak load; (c) at 75% of peak load; (d) at 100% of peak load
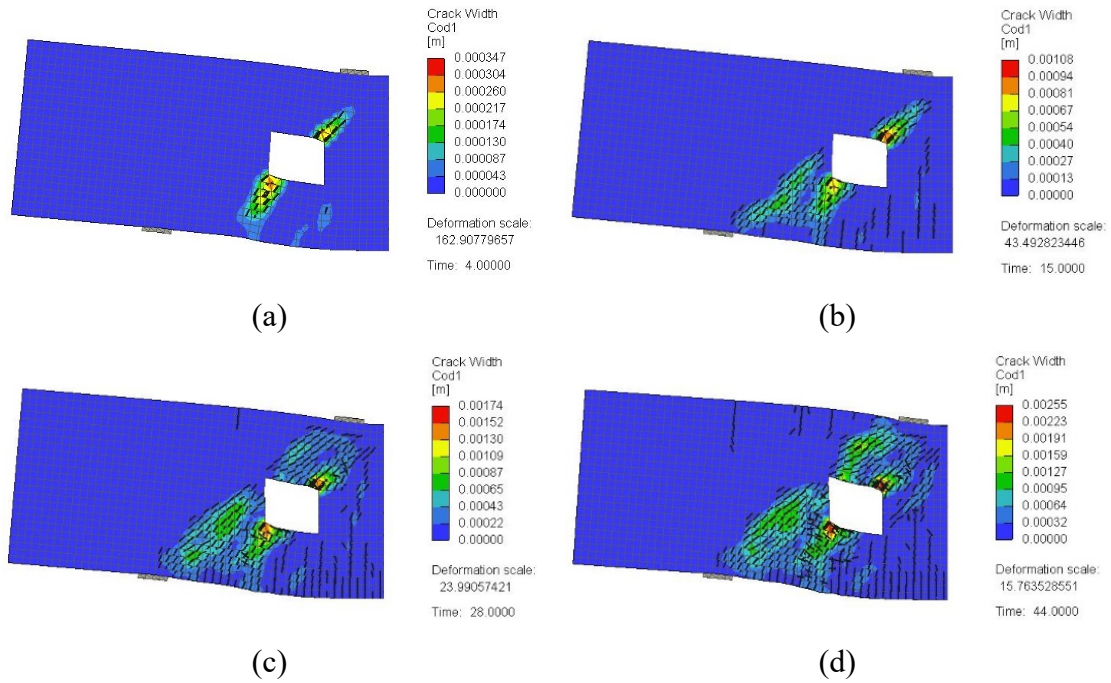
Figure 4.38: Crack pattern for a typical model failed due to extensive diagonal shear cracking at the opening corners (DB-X0.75-Y0.50): (a) at 25% of peak load; (b) at 50% of peak load; (c) at 75% of peak load; (d) at 100% of peak load
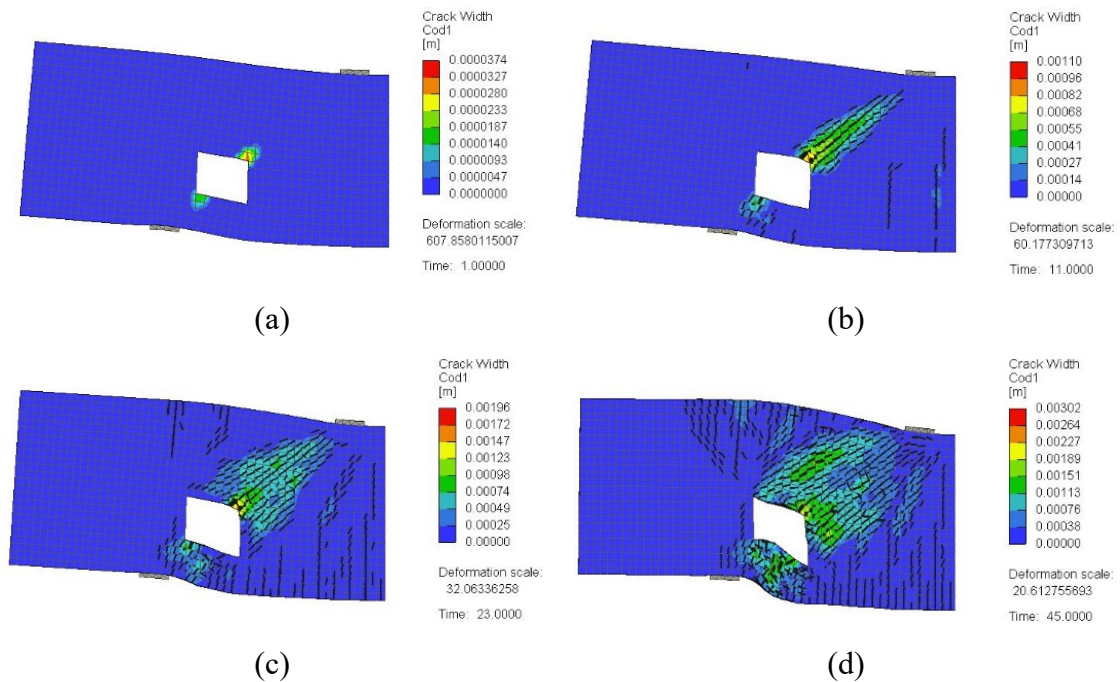
Figure 4.39: Crack pattern for a typical model failed due to simultaneous failure of the concrete along the upper and lower load paths (DB-X0.25-Y0.33): (a) at 25% of peak load; (b) at 50% of peak load; (c) at 75% of peak load; (d) at 100% of peak load
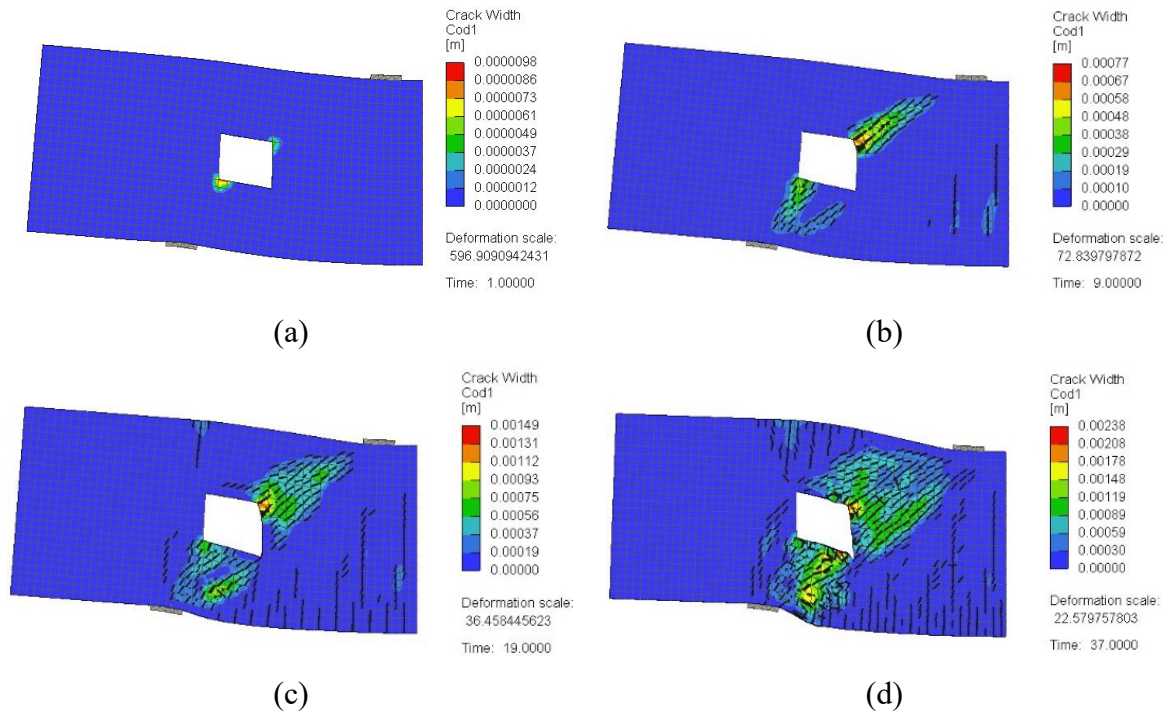
Figure 4.40: Crack pattern for a typical model failed due to failure of the concrete along the lower load path and excessive widening of shear cracks at the opening corner (DB-X0.25-Y0.50): (a) at 25% of peak load; (b) at 50% of peak load; (c) at 75% of peak load; (d) at 100% of peak load

4.3.2.3 GFRP Stresses

General 3D views of the stresses in the vertical GFRP stirrups predicted numerically for the beam models of this group are shown in Figures 4.41 to 4.43. The maximum stress in the vertical GFRP stirrups did not exceed the tensile strength of the bent portion (459 MPa), expect in model DB-X0.50-Y0.50, which exhibited a maximum stress of 477 MPa in a location close to the bent portion. For the beam models with x_o/X_c = 0.25 (Figure 4.41), the maximum stress in the vertical GFRP stirrups ranged from 335 to 431 MPa. The location of the maximum stress in the vertical GFRP stirrups varied based on the value of y_o/h. When the opening was close to the tension face (DB-X0.25-Y0.33), the maximum stress was in the vertical GFRP stirrup at the side of the opening. When the opening was pushed upward (DB-X0.25-Y0.50 and DB-X0.25-Y0.75), the maximum stress was in the short vertical GFRP stirrups located in the lower chord below the opening. Figure 4.42 shows that the beam models DB-X0.50-Y0.0.33 and DB-X0.50-Y0.75 exhibited a maximum stress in the vertical GFRP stirrups of 375 and 315 MPa, respectively, which was typically located in the full-depth vertical stirrup at one of

83

the sides of the opening. The maximum GFRP stress in model DB-X0.50-Y0.50 (477 MPa) was in the two full-depth vertical stirrups located at both sides of the opening. For the beam models with $x_o/X_c = 0.75$ (Figure 4.43), the maximum stress in the vertical GFRP stirrups ranged from 333 to 452 MPa. The top horizontal part of the vertical stirrup below the load point in DB-X0.75-Y0.33 reached 98% of the tensile strength of the bent portion of the GFRP. The maximum GFRP stress for the beam model DB-X0.75-Y0.50 was in one of the short GFRP stirrups in the top chord above the opening and in the full-depth vertical GFRP stirrup at the side of the opening closer to the support. For the beam model DB-X0.75-Y0.75, the maximum stress was in the full-depth vertical GFRP stirrup at the side of the opening closer to the support.

(a)   (b)   (c)
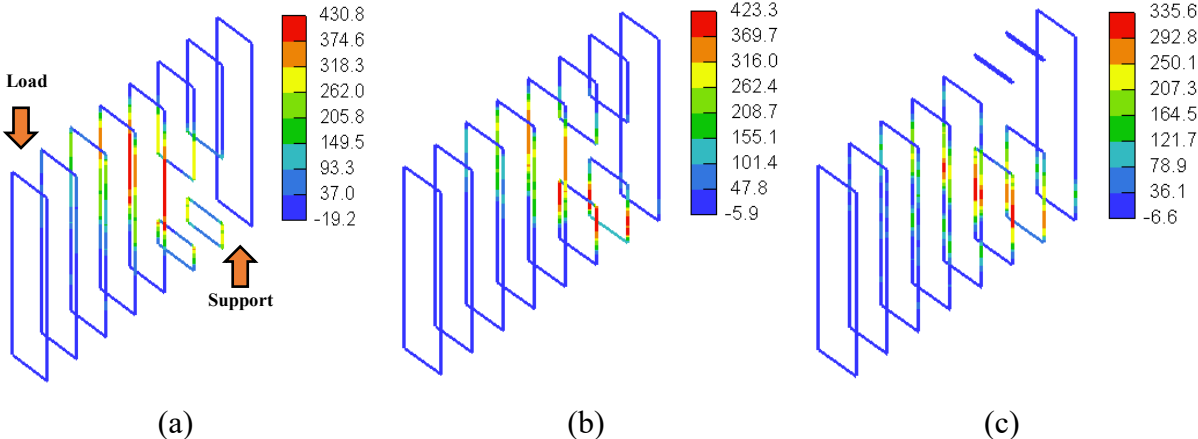
Figure 4.41: 3D view of stresses in GFRP bars for models with $x_o/X_c = 0.25$ (MPa): (a) DB-X0.25-Y0.33; (b) DB-X0.25-Y0.50; (c) DB-X0.25-Y0.75

(a)   (b)   (c)
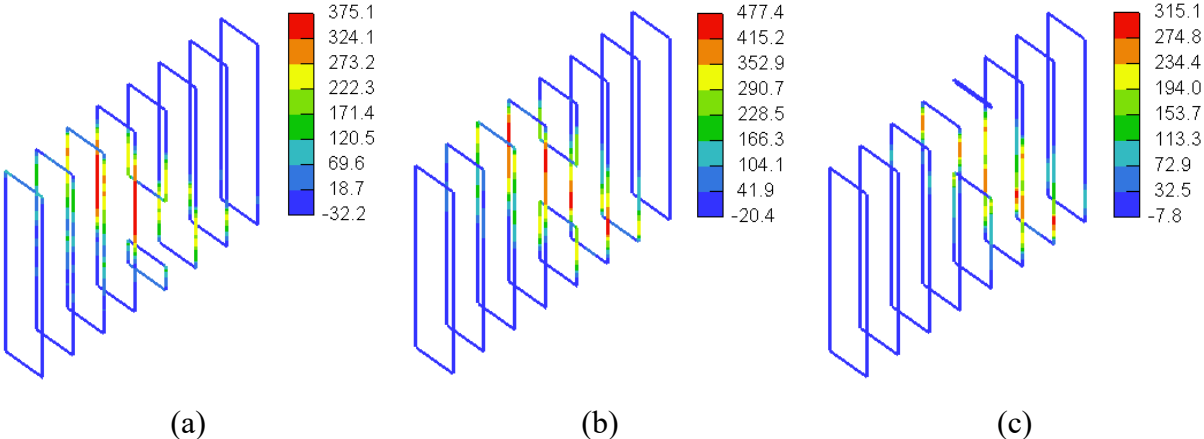
Figure 4.42: 3D view of stresses in GFRP bars for models with $x_o/X_c = 0.50$ (MPa): (a) DB-X0.50-Y0.33; (b) DB-X0.50-Y0.50; (c) DB-X0.50-Y0.75

84
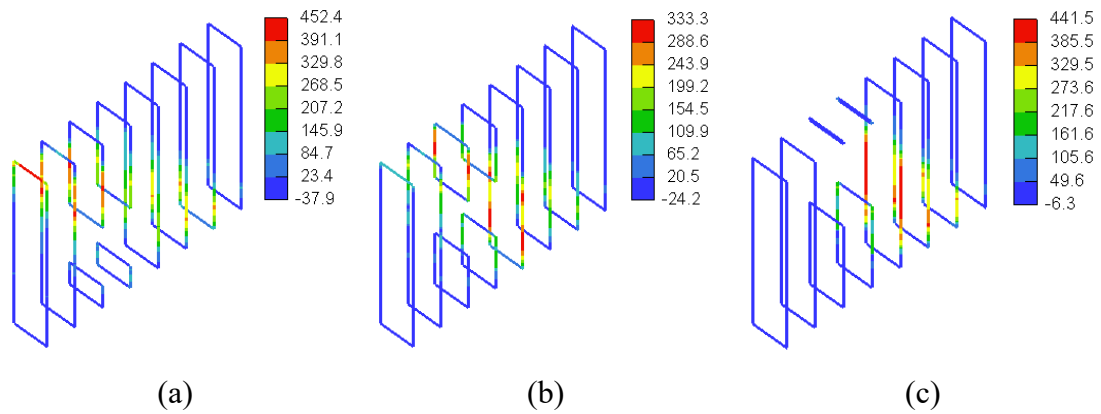
Figure 4.43: 3D view of stresses in GFRP bars for models with $x_o/X_c = 0.75$ (MPa): (a) DB-X0.75-Y0.33 (b) DB-X0.75-Y0.50; (c) DB-X0.75-Y0.75

Figures 4.44 to 4.49 show stresses in the horizontal web reinforcement and tensile flexural reinforcement predicted numerically for the beam models of this group. None of the horizontal web reinforcing bars or the flexural reinforcement at tension side in the deep beam models of this group reached their tensile strength. Generally, the maximum stress in the horizontal GFRP bars was on average 275 MPa (23% of the tensile strength of straight GFRP bars), with a minimum of 188 MPa (16% of the tensile strength of straight GFRP bars) and a maximum of 325 MPa (27% of the tensile strength of straight GFRP bars). The stresses in the flexural tensile GFRP reinforcement within the shear span were almost constant within the shear span, except at the region near the support which exhibited reduced values of GFRP stresses. The near-uniform stress distribution of the GFRP stress in the flexural GFRP reinforcing bars within the shear span indicated that they acted as a tie, which is in alignment with the behavior of D-regions. The maximum stress in the flexural GFRP bars was on average 240 MPa (24% of the tensile strength of straight GFRP bars), with a minimum of 176 MPa (18% of the tensile strength of straight GFRP bars) and a maximum of 386 MPa (39% of the tensile strength of straight GFRP bars). The value of the maximum GFRP stress was dependent on the value of the ultimate load. The beam models with the higher ultimate load typically exhibited higher GFRP stresses in the flexural reinforcement at peak load. For instance, the smallest longitudinal GFRP stresses of 176, 184, and 190 MPa were recorded for the beam models DB-X0.25-Y0.50, DB-X0.50-Y0.75, and DB-X0.75-Y0.75 having the

85

lowest ultimate loads. The greatest longitudinal GFRP stress of 386 MPa was recorded for the beam model DB-0.75-0.33 having the greatest ultimate load.

(a)   (b)   (c)
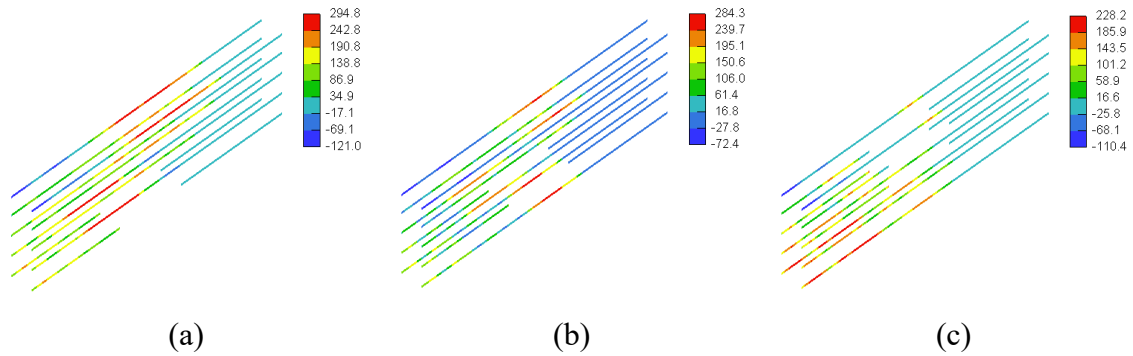
Figure 4.44: Stresses in horizontal GFRP web reinforcement for models with $x_o/X_c =$ 0.25 (MPa): (a) DB-X0.25-Y0.33; (b) DB-X0.25-Y0.50; (c) DB-X0.25-Y0.75

(a)   (b)   (c)
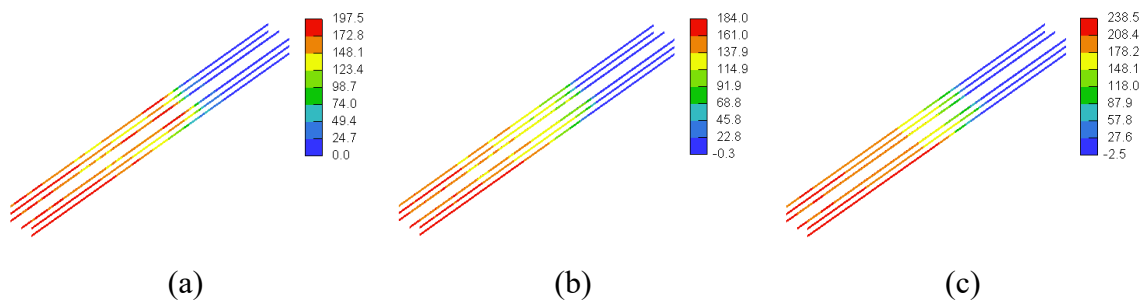
Figure 4.45: Stresses in bottom GFRP flexural reinforcement for models with $x_o/X_c =$ 0.25 (MPa): (a) DB-X0.25-Y0.33; (b) DB-X0.25-Y0.50; (c) DB-X0.25-Y0.75

(a)   (b)   (c)
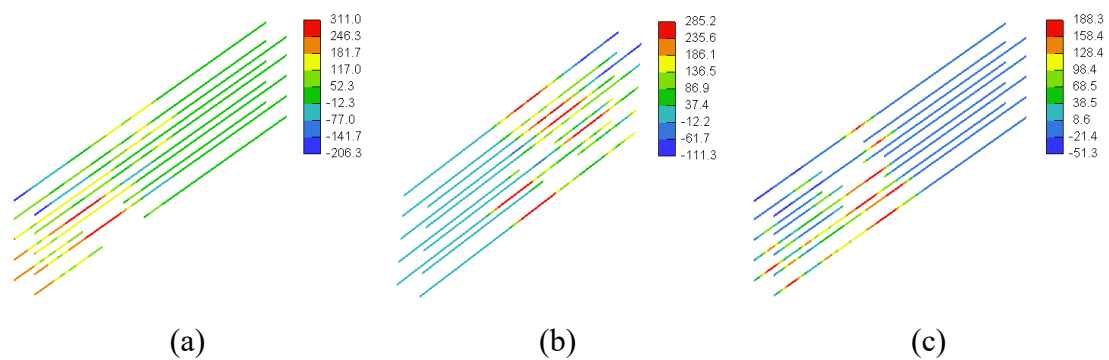
Figure 4.46: Stresses in horizontal GFRP web reinforcement for models with $x_o/X_c =$ 0.50 (MPa): (a) DB-X0.50-Y0.33; (b) DB-X0.50-Y0.50; (c) DB-X0.50-Y0.75

86
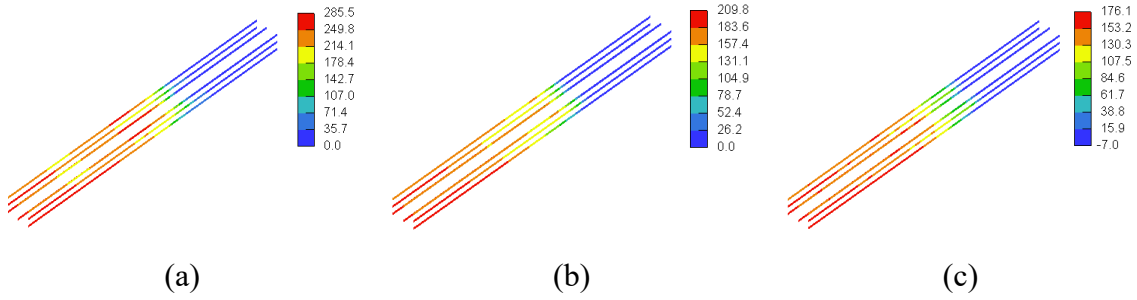
Figure 4.47: Stresses in bottom GFRP flexural reinforcement for models with $x_o/X_c =$ 0.50 (MPa): (a) DB-X0.50-Y0.33; (b) DB-X0.50-Y0.50; (c) DB-X0.50-Y0.75
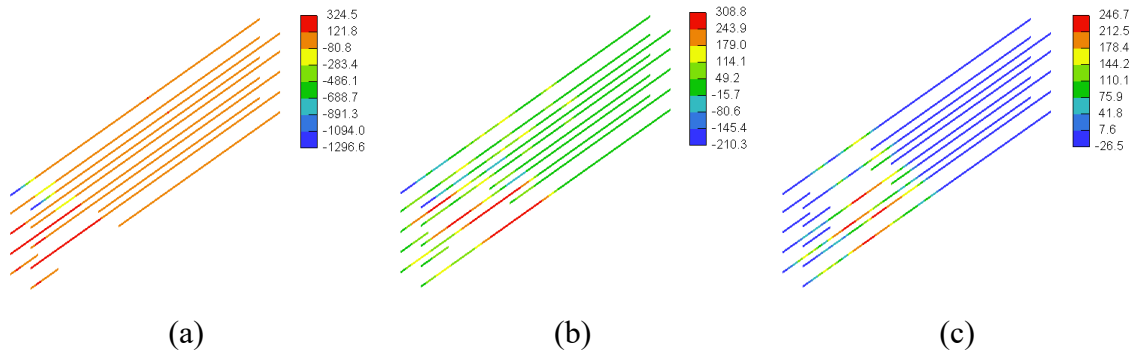
Figure 4.48: Stresses in horizontal GFRP web reinforcement for models with $x_o/X_c =$ 0.75 (MPa): (a) DB-X0.75-Y0.33 (b) DB-X0.75-Y0.50; (c) DB-X0.75-Y0.75
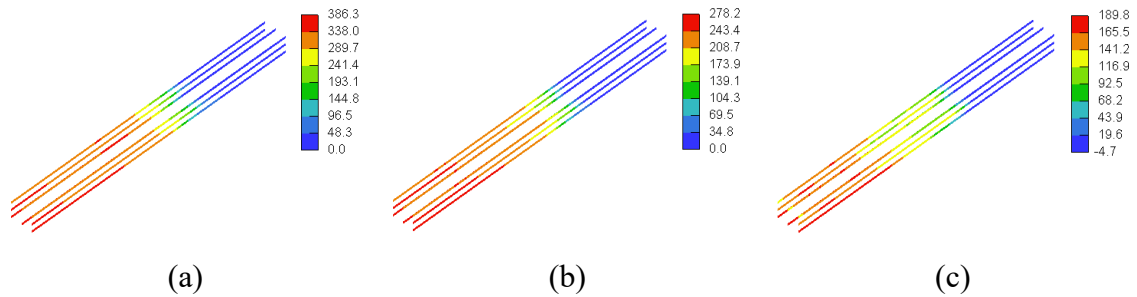
Figure 4.49: Stresses in bottom GFRP flexural reinforcement for models with $x_o/X_c =$ 0.75 (MPa): (a) DB-X0.75-Y0.33 (b) DB-X0.75-Y0.50; (c) DB-X0.75-Y0.75

4.4 Simplified Analytical Formulas

4.4.1 Solid Deep Beams

Kong et al. [37] proposed Equation 1 to estimate the shear capacity (V_u) of solid concrete deep beams reinforced with steel bars. For simplicity, the equation is called Kong's formula in the following text, noting that the ultimate load (P_u) of the deep

beams of the present study equals $2V_u$. In these equations, X = clear shear span, f_t = tensile strength of the concrete, b = width of the beam, h = total depth of the beam, A = area of an individual web bar or a main reinforcing bar, y_1 = depth at which a typical bar intersects a potential critical shear crack, α_1 = angle of inclination between a typical bar and the critical shear crack, C_1 = 1.4 for normal weight concrete, and C_2 = 300 N/mm^2 for deformed steel bars.

Table 4.5 compares predictions of Kong's Equation 1 [37] for the solid deep beams included in the parametric study to the strengths predicted by the numerical analysis. It is evident that Kong's Equation 1 significantly overestimated the ultimate loads of the solid deep beam models by up to 82%. The unconservative predictions provided by Kong's Equation 1 [37] could be attributed to two reasons. Firstly, a reduction in the contribution of the concrete to the shear capacity caused by the increased transverse strain due to stressing of the GFRP bars and the increased crack width of the inclined shear cracks developed along the strut developed in the shear span. The second reason is the reduced dowel action provided by the GFRP longitudinal reinforcement. The replacement of the steel reinforcement by GFRP bars necessitates a modification in the contribution of the concrete to the shear resistance to account for the increased crack width on the strut capacity and in the value of C_2 for the main longitudinal bars to account for an anticipated reduction in the dowel action in GFRP-reinforced concrete deep beams. As such, Equations 2, proposed in the present study, represent a refined formula to estimate V_u of solid concrete deep beams reinforced with GFRP bars, where A_f = individual area of a main reinforcing bar, A_w = individual area of a web reinforcing bar, E_f = elastic modulus of the main GFRP reinforcing bars (66.4 GPa), and E_s = elastic modulus of steel bars (200 GPa). As shown in Table 4.5, predictions of the refined analytical formula are in good agreement with the numerical results. The ultimate loads predicted by the refined analytical formula were within an 11% error band. The minor deviation between predictions of the analytical formula and the numerical results verifies its capacity to provide reasonable predictions for the ultimate load of solid GFRP-reinforced concrete deep beams.

$$V_u = C_1 \left[1 - 0.35 \frac{X}{h} \right] f_t bh + \sum C_2 A \frac{y_1}{h} \sin^2 \alpha_1 \qquad (1)$$

$$V_u = C_1 \left[1 - 0.50 \frac{X}{h} \right] f_t bh + \sum C_2 \frac{E_f}{E_s} A_f \frac{y_1}{h} \sin^2 \alpha_1 + \sum C_2 A_w \frac{y_1}{h} \sin^2 \alpha_1 \quad (2)$$

Table 4.5: Comparison between predictions of analytical formulas and numerical results

Model	Ultimate Load (kN)				
	Numerical	Kong's Formula [37] (Eq. 1)		Refined Formula (Eq. 2)	
		Prediction	Error (%) [1]	Prediction	Error (%) [1]
SDB-1.0-L	1865	2819	+51	1678	-10
SDB-1.0-M	2064	3253	+58	2030	-2
SDB-1.0-H	2661	3805	+43	2478	-7
SDB-1.5-L	1101	1998	+81	1013	-8
SDB-1.5-M	1284	2332	+82	1221	-5
SDB-1.5-H	1644	2756	+68	1487	-10
SDB-1.0-L100	2510	3700	+47	2559	2
SDB-1.0-L200	2100	3214	+53	2072	-1
SDB-1.0-M100	2821	4134	+47	2911	3
SDB-1.0-M200	2601	3647	+40	2424	-7
SDB-1.0-H100	3094	4686	+51	3358	+9
SDB-1.0-H200	2909	4200	+44	2872	-1
SDB-1.5-L100	1885	3082	+63	2097	+11
SDB-1.5-L200	1411	2546	+80	1560	+11
SDB-1.5-M100	2199	3416	+55	2306	5
SDB-1.5-M200	1797	2879	+60	1769	-2
SDB-1.5-H100	2464	3840	+56	2571	4
SDB-1.5-H200	2149	3304	+54	2034	-5

[1] Error (%) $= \frac{\text{Formula-Numerical}}{\text{Numercial}} \times 100$

4.4.2 Deep Beams with a Web Opening in the Midpoint of the Shear Span

Kong and Sharp [38] developed Equation 3 to determine V_u of steel-reinforced deep beams with a web opening, noting that the ultimate load (P_u) of the deep beams of the present study equals $2V_u$. The coefficients a_1, a_2, K_1, K_2, and λ are introduced in Equation 4 for deep beams with web openings. The coefficients $K_1 = X_o/X$ and $K_2 = Y_o/h$ define the position of the opening, where X_o = horizontal distance between the center of the opening and the inner face of the support plate and Y_o = vertical distance between the

center of the opening and the bottom face of the beam. The coefficients $a_1 = w_o/2X$ and $a_2 = h_o/2h$ define the opening size. The coefficient $\lambda = 1.0$ for main longitudinal bars, whereas for web reinforcing bars, $\lambda = 1.5$. Table 4.6 compares predictions of Kong's Equation 3 [38] for the GFRP-reinforced deep beams with a web opening in the middle of the shear span included in the parametric study to the strengths predicted by the numerical analysis. It is evident that Kong's Equation 3 consistently overestimated the ultimate loads of the deep beam models a web opening in the middle of the shear span by up to 20%. The unconservative predictions provided by Kong's Equation 3 [38] could be attributed to the reduced dowel action provided by the GFRP longitudinal reinforcement. As such, Equations 4, proposed in the present study, represent a refined formula to estimate V_u of GFRP-reinforced concrete deep beams with a web opening, where $A_f =$ individual area of a main reinforcing bar, $A_w =$ individual area of a web reinforcing bar, $E_f =$ elastic modulus of the main GFRP reinforcing bars (66.4 GPa), and $E_s =$ elastic modulus of steel bars (200 GPa). As shown in Table 4.6, predictions of the refined analytical formula provided conservative prediction for the ultimate loads of the deep beam models with an opening in the middle of the shear span.

$$V_u = C_1 \left[1 - 0.35 \frac{X}{h} \right] f_t b h + \sum C_2 \frac{E_f}{E_s} A_f \frac{y_1}{h} sin^2 \alpha_1 + \sum C_2 A_w \frac{y_1}{h} sin^2 \alpha_1 \qquad (3)$$

$$V_u = C_1 \left[1 - 0.35 \frac{(K_1 + a_1)X}{(K_2 - a_2)h} \right] f_t b (K_2 - a_2) h + \sum C_2 \frac{E_f}{E_s} A_f \frac{y_1}{h} sin^2 \alpha_1 + \sum \lambda C_2 A_w \frac{y_1}{h} sin^2 \alpha_1 \qquad (4)$$

Table 4.6: Comparison between predictions of the analytical formulas and numerical results of deep beams with an opening in the middle of the shear span

Model	Ultimate Load (kN)				
	Numerical	Kong's Formula [38] (Eq. 3)		Refined Formula (Eq. 4)	
		Prediction	Error (%) [1]	Prediction	Error (%) [1]
DB-W0.16-H0.17	1789	1942	+9	1378	-23
DB-W0.16-H0.25	1637	1863	+14	1373	-16
DB-W0.16-H0.33	1327	1385	+4	966	-27
DB-W0.27-H0.17	1678	1928	+15	1438	-14
DB-W0.27-H0.25	1504	1709	+14	1291	-14
DB-W0.27-H0.33	1239	1242	+1	892	-28
DB-W0.32-H0.17	1585	1871	+18	1405	-11
DB-W0.32-H0.25	1374	1653	+20	1258	-8
DB-W0.32-H0.33	1019	1038	+2	709	-30

[1] Error (%) $= \frac{\text{Formula-Numerical}}{\text{Numercial}} \times 100$

4.4.3 Deep Beams with a Web Opening Shifted from the Midpoint of the Shear Span

Table 4.7 compares predictions of Kong's Equation 3 [38] for the GFRP-reinforced deep beams with a web opening at different locations within the shear span. It is evident that Kong's Equation 3 provided inconsistent results. In many cases, the prediction of Equation 3 was significantly higher than the strength obtained from the numerical analysis. In some other cases, the prediction of Equation 3 was lower. It is noteworthy that Equation 4 proposed in the current study did not provide satisfactory results when the web opening was shifted from the middle of the shear span. These results indicate that for GFRP-reinforced beams with a web opening shifted from the middle of the shear span, a modified Equation should be adopted. As such, the refined formula given in Equation 5 is proposed for the prediction of the shear strength of GFRP-reinforced deep beams with a web opening shifted from the midpoint of the shear span. Two coefficients were introduced in this formula, namely λ_1 and λ_2 to account for the opening size and location, respectively. These two coefficients were proposed based on careful examination of the ultimate loads of the deep beam models with a web opening shifted from the midpoint of the shear span. The results of the parametric study showed an increase in the ultimate load with an increase in the distance from the support

for the beam models with K_2 values of 0.33 and 0.5. The results of the parametric study also indicated that when the center of the opening was located at K_2 value of 0.75, a reduction in the ultimate load was recorded with an increase in the distance from the support. The coefficient λ_2 reflects the trend of the results of the parametric study. Predictions of the refined Equation 5 are in good agreement with the results of the numerical analysis. It is noteworthy that for models DB-X0.25-Y0.75 and DB-X0.75-Y0.33 having a web opening not interrupting the natural load path, the formulas for the solid deep beams were also examined in Table 4.7. The ultimate loads of DB-X0.25-Y0.75 and DB-X0.75-Y0.33 predicted by Kong's formula for solid deep beams (Equation 1) were still overestimated. When the refined formula for solid deep beams (Equation 2) was applied, it provided good prediction for the ultimate load of model DB-X0.75-Y0.33, but overestimated the ultimate load of model DB-X0.25-Y0.75. As such, it is recommended to use Equation 5 for deep beams with an opening shifted from the midpoint of the shear span even if the opening is not interrupted by the natural load path.

$$V_u = \lambda_1 \lambda_2 C_1 \left[1-0.35\frac{X}{h} \right] f_t bh + \sum C_2 \frac{E_f}{E_s} A_f \frac{y_1}{h} sin^2 \alpha_1 + \sum C_2 A_w \frac{y_1}{h} sin^2 \alpha_1 \qquad (5)$$

$$\lambda_1 = (1 - a_1)(1 - a_2)$$

$$\lambda_2 = \left[1-\frac{K_2}{3K_1} \right] ; \text{ when } K_2 = 0.33 \text{ or } 0.50$$

$$\lambda_2 = \left[1-\frac{K_1}{1.15K_2} \right]; \text{ when } K_2 = 0.75$$

Table 4.7: Comparison between predictions of the analytical formulas and numerical results of deep beams with an opening shifted from the midpoint of the shear span

Model	Ultimate Load (kN)				
	Numerical	Kong's Formula [38] (Eq. 3)		Refined Formula (Eq. 5)	
		Prediction	Error (%) [1]	Prediction	Error (%) [1]
DB-X0.25-Y0.33	1478	1216	-18	1436	-3
DB-X0.25-Y0.50	1337	2264	+69	1188	-11
DB-X0.25-Y0.75	1714	3513 (3647) [2]	+105 (+112) [2]	1848 (2424) [3]	8 (+41) [3]
DB-X0.50-Y0.33	1971	916	-54	1825	-7
DB-X0.50-Y0.50	1504	1709	+14	1683	12
DB-X0.50-Y0.75	1259	2863	+127	1349	7
DB-X0.75-Y0.33	2429	1042 (3647) [2]	-57 (+50) [2]	2055 (2424)[3]	-15 (0) [3]
DB-X0.75-Y0.50	1884	1461	-22	1877	0
DB-X0.75-Y0.75	1139	2399	+111	910	-20

[1] Error (%) $= \frac{\text{Formula-Numerical}}{\text{Numercial}} \times 100$

[2] Values between parentheses represent the prediction and corresponding error in case Kong's Eq.1 for solid deep beams is applied.

[3] Values between parentheses represent the prediction and corresponding error in case the refined Eq.2 for solid deep beams is applied.

Chapter 5: Conclusion

5.1 Design Implications

This research provided new knowledge on the behavior of GFRP-reinforced concrete deep beams with and without a web opening through a numerical analysis. The simulation models developed in the current study served as a numerical platform for performance prediction of GFRP-reinforced deep beams with and without a web opening. The location and size of the web opening played a critical role in the behavior of GFRP-reinforced deep beams. Placing the web opening in the compression zone close to the load plate or in the tension zone close to the support plate was very detrimental to the beam strength. A negligible strength reduction could be obtained when the web opening was placed in the tension side above the flexural reinforcement at the section of maximum moment away from the natural load path. Existing empirical equations for shear strength predictions of concrete deep beams with and without a web opening reinforced with conventional steel bars were not valid for GFRP-reinforced concrete deep beams. The new refined equations proposed in the current study predicted the ultimate load of GFRP-reinforced concrete deep beams with and without a web opening with good accuracy. The findings of the present study are anticipated to assist practitioners and researchers in designing concrete D-regions reinforced with GFRP bars. The outcomes of the study are anticipated to advance development of design guidelines and standards on reinforcing concrete structures with GFRP bars. The widespread use of GFRP reinforcing bars instead of the conventional steel reinforcement in construction would reduce repair cycles and operational costs with positive impacts on the UAE and worldwide.

5.2 Research Implications

Three-dimensional (3D) simulation models capable of predicting the structural behavior of GFRP-reinforced concrete beams with D-regions were developed and validated against published experimental data. A parametric study was conducted to investigate the influence of key parameters affecting the structural behavior of GFRP-reinforced concrete deep beams with and without a web opening. Refined simplified

94

analytical formulas were introduced for shear strength prediction of GFRP-reinforced concrete beams with D-regions. Based on results of the numerical analysis, the following conclusions are drawn:

- The ultimate loads of the solid deep models without web reinforcement increased with an increase in the concrete compressive strength. At $a/h = 1.0$, the strengths of the solid deep beam models without web reinforcement having moderate and high concrete compressive strengths were 11 and 43% higher than that of the model with the low concrete strength. The respective values at $a/h = 1.5$ were 17 and 49%.

- The ultimate loads of the deep models without web reinforcement with $a/h = 1.5$ were lower than those of their counterparts with $a/h = 1.0$. However, varying the concrete compressive strength had almost no effect on the strength reduction caused by increasing the value of a/h 1.0 to 1.5. The beam models with low, moderate, and high concrete compressive strengths showed strength reductions of 41, 38, and 38%, respectively due to increasing the value of a/h 1.0 to 1.5.

- The ultimate load of solid deep models without web reinforcement increased almost linearly with an increase in f'_c, irrespective of the value of a/h. The strength gain caused by reducing the value of a/h from 1.5 to 1.0 was in the range of 64% with a minimum of 61% and a maximum of 69%.

- The ultimate load of the solid deep beam models with web reinforcement decreased with an increase in the value of a/h from 1.0 to 1.5. The strength reduction caused by increasing the value of a/h tended to decrease with an increase in the concrete compressive strength. The deep beam models with web reinforcement having low, moderate, and high concrete compressive strengths with $s = 100$ mm exhibited strength reductions of 25, 22, and 21%, respectively, due to increasing the value of a/h 1.0 to 1.5. Their counterpart beam models with $s = 200$ mm exhibited greater strength reductions of 33, 31, and 26%, respectively, due to increasing the value of a/h from 1.0 to 1.5. The strength reduction caused by increasing the value of a/h was more pronounced

for the beam models with the lower amount of web reinforcement (i.e., greater spacing between web reinforcement).

- The ultimate load of the solid deep beam models with web reinforcement increased almost linearly with an increase in the concrete compressive strength and a decrease in the spacing between the web reinforcement, irrespective of the value of a/h. The strength gain caused by increasing the amount of web reinforcement was more pronounced for the beam models with the greater a/h of 1.5. furthermore, the impact of increasing the amount of the web reinforcement diminished with an increase in the concrete compressive strength. For the beam models with $a/h = 1.0$, strength gains of 20, 8, and 6% were recorded at low, moderate, and high concrete compressive strengths, respectively. The respective values for the beam models with $a/h = 1.5$ were 34, 22, and 15%.

- The behavior of the deep beam models was dependent on the opening size and location. The strength of the beam models decreased with an increase in either the opening width or height. The rate of the strength reduction caused by increasing the opening height was, however, more significant than that produced by increasing the opening width. At the same w_o/a of 0.16, strength reductions of 31, 37, and 49% were recorded for the deep beam models having an opening in the midpoint of the shear span with h_o/h values of 0.17, 0.25, and 0.33, respectively. The strength reduction caused by increasing the opening height was more pronounced at the greater w_o/a values. At w_o/a of 0.27, strength reductions of 35, 42, and 52% were recorded for the deep beam models with h_o/h values of 0.17, 0.25, and 0.33, respectively. At w_o/a of 0.32, strength reductions of 39, 47, and 61% were recorded for the deep beam models with h_o/h values of 0.17, 0.25, and 0.33, respectively.

- The location of the web opening within the shear span played a primary role in the behavior of the deep beam models. Placing a web opening in the compression zone close to the load plate ($x_o/X_c = 0.75$ and $y_o/h = 0.75$) was very detrimental to the beam strength. A negligible strength reduction was recorded when the web opening was placed in the tension side above the

flexural reinforcement and away from the natural load path and the support plate ($x_o/X_c = 0.75$ and $y_o/h = 0.33$). For the beam models with y_o/h of 0.33 and 0.50, the strength increased with an increase in the distance measured from the face of the support within the shear span. The strength of the beam models with y_o/h of 0.33 tended to be higher than that of their counterparts with y_o/h of 0.50, and this behavior was more evident with an increase in the distance from the face of the support plate. The beam models with y_o/h of 0.75 exhibited an opposite trend, where the strength decreased with an increase in the distance measured from the face of the support within the shear span.

- For the beam models having a web opening with x_o/X_c of 0.25, strength reductions of 43 and 49% were recorded at y_o/h values of 0.33 and 0.50, respectively. When the opening was pushed upward away from the natural load path ($x_o/X_c = 0.25$ and $y_o/h = 0.75$), a lower strength reduction of 34% was recorded. For the beam models having a web opening with x_o/X_c of 0.50, strength reductions of 24, 42, and 52% were recorded at y_o/h values of 0.33, 0.50, and 0.75, respectively. The beam model with $x_o/X_c = 0.75$ and $y_o/h = 0.33$ exhibited a negligible strength reduction of 7% because the web opening was in the tension side and also did not interrupt the natural load path. In contrast, the beam model The beam model with $x_o/X_c = 0.75$ and $y_o/h = 0.75$ exhibited a significant strength reduction of 56% because the web opening was in the compression zone close to the load plate and fully interrupted the natural load path.

- Existing empirical equations for concrete deep beams reinforced with conventional steel bars with and without a web opening provided inconsistent and unconservative predictions for the ultimate load of the beam models reinforced with GFRP bars.

- Previously published analytical equations for shear strength prediction of deep beams with and without a web opening were refined through modifying and/or adding coefficients to account for the effect of changing the type of reinforcement from steel to GFRP on the shear capacity. These coefficients were obtained based on an inverse analysis approach aimed at minimizing the

difference between predictions of the refined analytical formulas and results of the numerical models. The refined analytical formulas proposed in the present study provided reasonable predictions for the shear capacity of GFRP-reinforced concrete deep beams with and without a web opening.

5.3 Limitation and Future Work

Results of the present study are limited to the range of values adopted in the numerical analysis in terms of the concrete compressive strength, a/h, detailing and properties of the GFRP reinforcement, and the sizes and locations of the web openings considered in this study as well as the materials properties used. Also, changing the concrete section size may have an impact on the results of the numerical analysis. Future work should investigate the effect of varying the concrete section size, properties of the nonmetallic reinforcement, and detailing of the reinforcement around the web opening on the behavior of concrete deep beams with nonmetallic FRP reinforcement.

References

[1] A. Committee, Building Code Requirements for Structural Concrete (ACI 318-19) and Commentary (ACI 318R-19), MI: American Concrete Institute (ACI), 2019.

[2] J. MacGregor and J. Wight, Reinforced Concrete Mechanics and Design - 4th Edition, Singapore: Prentice Hall, 2005.

[3] F. K. Kong, Reinforced Concrete Deep Beams, London: Blackie and Son Ltd, 1991.

[4] K. H. Tan and M. A. Mansur, Concrete Beams with Openings: Analysis and Design, New York: CRC Press, 1999.

[5] K. H. T. and M. A. Mansur, Concrete Beams with Openings: Analysis and Design, New York: CRC Press, 1999.

[6] C. S. Association, Design and Construction of Building Structures with Fibre-reinforced Polymers (CSA S806), Mississauga: Canadian Standards Association, 2012.

[7] A. C. Institute, Guide for the Design and Construction of Structural Concrete Reinforced with Fiber-Reinforced Polymer (FRP) Bars (ACI 440.1R-15), MI: American Concrete Institute (ACI), 2015.

[8] C. E. Bakis, Bank, B. V. L. L. C., E. D. J. F. Cosenza, J. J. Lesko, A. R. S. H. Machida and T. C. Triantafillou, "Fiber-Reinforced Polymer Composites for Construction-State-of-the-Art Review," *J. Compos. Constr.,* vol. 6, no. 2, pp. 73-87, 2002.

[9] L. Bank, Composites for Construction: Structural Design with FRP Materials, New Jersy: John Wiley & Sons, 2006.

[10] H. V. S. GangaRao, N. Taly, and P. V. Vijay, Reinforced Concrete Design with FRP Composites, New York: CRC Press, 2006.

[11] A. Nanni, A. De Luca, and H. J. Zadeh, Reinforced Concrete with FRP Bars: Mechanics and Design - 1st Edition, New York: CRC Press, 2014.

[12] A. Obaida, Behavior of Double-Sided Concrete Corbels Reinforced With Glass-Fiber Reinforced Polymer Bars, Al Ain: United Arab Emirates University, 2016.

[13] A. K. Tureyen and R. J. Frosch, "Shear Tests of FRP-Reinforced Concrete Beams without Stirrups," *ACI Struct. J. ,* vol. 99, no. 4, pp. 427-434, 2002.

[14] M. Guadagnini, K. Pilakoutas and P. Waldron, "Shear Resistance of FRP RC Beams: Experimental Study," *J. Compos. Constr. ,* vol. 10, no. 6, pp. 464-473, 2006.

[15] A. K. El-Sayed, E. F. El-Salakawy and B. Benmokrane, "Shear Capacity of Hight-Strength Concrete Beams Reinforced with FRP Bars," *ACI Struct. J.,* vol. 103, no. 3, pp. 383-389, 2006.

[16] A. K. El-Sayed, E. F. El-Salakawy and B. Benmokrane, "Shear Strength of FRP-Reinforced Concrete Beams without Transverse Reinforcement," *ACI Struct. J.,* vol. 103, no. 2, pp. 235-243, 2006.

[17] E. C. Bentz, L. Massam and M. J. Collins, "Shear Strength of Large Concrete Members with FRP Reinforcement," *J. Compos. Constr.,* vol. 14, no. 6, pp. 637-646, 2010.

[18] I. F. Kara, "Prediction of shear strength of FRP-reinforced concrete beams without stirrups based on genetic programming," *Advan. Eng. Softw. ,* vol. 42, no. 6, pp. 295-304, 2011.

[19] D. Tomlinson and A. Fam, "Performance of Concrete Beams Reinforced with Basalt FRP for Flexure and Shear," *J. Compos. Constr. ,* vol. 19, no. 2, 2014.

[20] A. El-Refai and F. Abed, "Concrete Contribution to Shear Strength of Beams Reinforced with Basalt Fiber-Reinforced Bars," *J. Compos. Constr. ,* vol. 20, no. 4, 2015.

[21] M. A. Issa, T. Ovitigala and M. Ibrahim, "Shear Behavior of Basalt Fiber Reinforced Concrete Beams with and without Basalt FRP Stirrups," *J. Compos. Constr.,* vol. 20, no. 4, 2015.

[22] A. Al-Hamrani and W. Alnahhal, "Shear behavior of basalt FRC beams reinforced with basalt FRP bars and glass FRP stirrups: Experimental and analytical investigations," *Eng. Struct. ,* vol. 242, p. 112612, 2021.

[23] A. El-Refai, W. Alnahhal, A. Al-Hamrani and S. Hamed, "Shear performance of basalt fiber-reinforced concrete beams reinforced with BFRP bars," *Compos. Struct. ,* vol. 288, p. 115443, 2022.

[24] Z. Omeman, M. Nehdi and H. El-Chabib, "Experimental study on shear behavior of carbon fiber-reinforced polymer reinforced concrete short beams without web reinforcement," *Can. J. Civ. Eng.,* vol. 35, no. 1, pp. 1-10, 2008.

[25] F. Abed, H. El-Chabib and M. Alhamaydeh, "Shear characteristics of GFRP-reinforced concrete deep beams without web reinforcement," *J. Reinf. Plast. Compos. ,* vol. 31, no. 16, pp. 1063-1073 , 2012.

[26] A. S. Farghaly and B. Benmokrane, "Shear Behavior of FRP-Reinforced Concrete Deep Beams without Web Reinforcement," *J. Compos. Constr. ,* vol. 17, no. 6, 2013.

[27] M. F. Andermatt and A. S. Lubell, "Behavior of Concrete Deep Beams Reinforced with Internal Fiber-Reinforced Polymer—Experimental Study," *ACI Struct. J. ,* vol. 110, no. 4, 2013.

[28] D. Kim, J. Lee and Y. H. Lee, "Effectiveness factor of strut-and-tie model for concrete deep beams reinforced with FRP rebars," *Compos. Part B,* vol. 56, pp. 117-125, 2014.

[29] H. Liu, J. Yang, X. Wang and D. Han, "Experimental Study on Shear Behavior of BFRP-reinforced Recycled Aggregate Concrete Deep Beams Without Stirrups," *KSCE. J. ,* vol. 21, no. 6, pp. 2289-2299, 2016.

[30] S. Alhamad, Y. Al-Banna, A. Al-Osman, J. Mouthassseeb, S. Abdalla and F. Abed, "Effect of shear span-to-depth ratio on the shear behavior of BFRP-RC deep beams," *MATEC,* vol. 120, p. 01012, 2017.

[31] F. Abed, A. El-Refai and S. Abdalla, "Experimental and finite element investigation of the shear performance of BFRP-RC short beams," *Struct.,* vol. 20, pp. 689-701, 2019.

[32] A. Abu-Obaida, B. El-Ariss and T. El-Maaddawy, "Behavior of Short-Span Concrete Members Internally Reinforced with Glass Fiber–Reinforced Polymer Bars," *J. Compos. Constr.,* vol. 22, no. 5, 2018.

[33] K. Mohamed, A. S. Farghaly and B. Benmokrane, "Effect of Vertical and Horizontal Web Reinforcement on the Strength and Deformation of Concrete Deep Beams Reinforced with GFRP Bars," *J. Struct. Eng. ,* vol. 143, no. 8, 2017.

[34] J. Frappier, K. Mohamed, A. S. Farghaly and B. Benmokrane, "Behavior and Strength of Glass Fiber-Reinforced Polymer Reinforced Concrete Deep Beams with Web Openings," *ACI Struct. J.*, vol. 116, no. 5, pp. 275-285, 2019.

[35] S. Arabasi and T. El-Maaddawy, "Reinforcing of discontinuity regions in concrete deep beams with GFRP composite bars," *Compos. Part C,* vol. 3, p. 100064 , 2020.

[36] C. e. C. s.r.o., "ATENA Computer Software," Prague, Czech Republic, [Online]. Available: https://www.cervenka.cz/ . [Accessed 25 March 2022].

[37] F. Kong, P. Robins, A. Singh, G. Sharp, "Shear analysis and design of reinforced concrete deep beams," *The Structural Engineer,* vol. 50, pp. 405-409, 1972.

[38] F. P. Kong and G. R. Sharp, "Structural idealisation for deep beams with web openings," *Magazine of Concrete Research,* vol. 29, no. 99, pp. 81-91, 1977.

List of Publications

- A. Sheikh-Sobeh, N. Kachouh, and T. El-Maaddawy, "Numerical analysis of GFRP-reinforced concrete deep beams containing web openings", *International Conference on Advances in Structural and Geotechnical Engineering (ICASGE'23)*, 6-9 March 2023, Hurghada, Egypt.
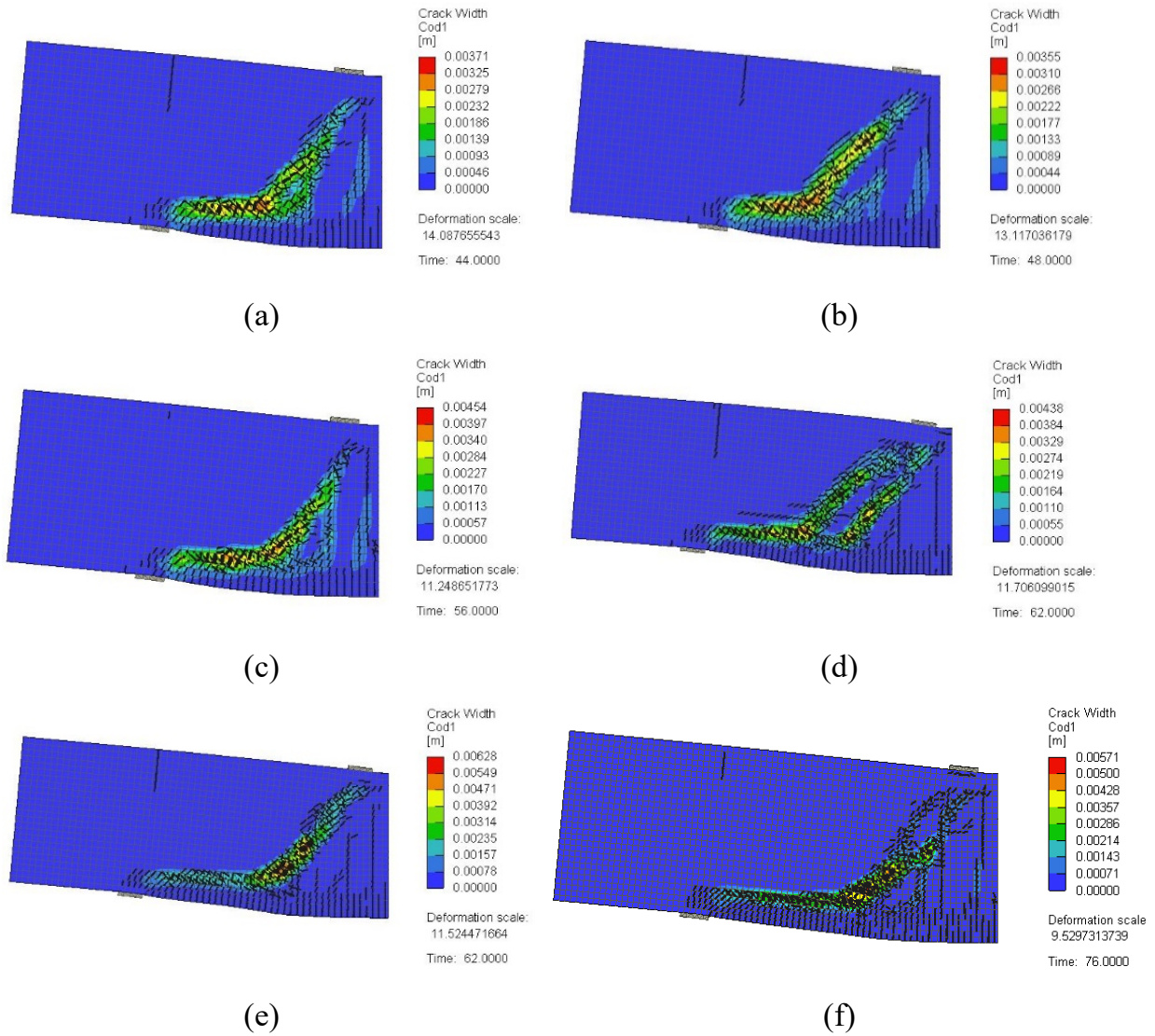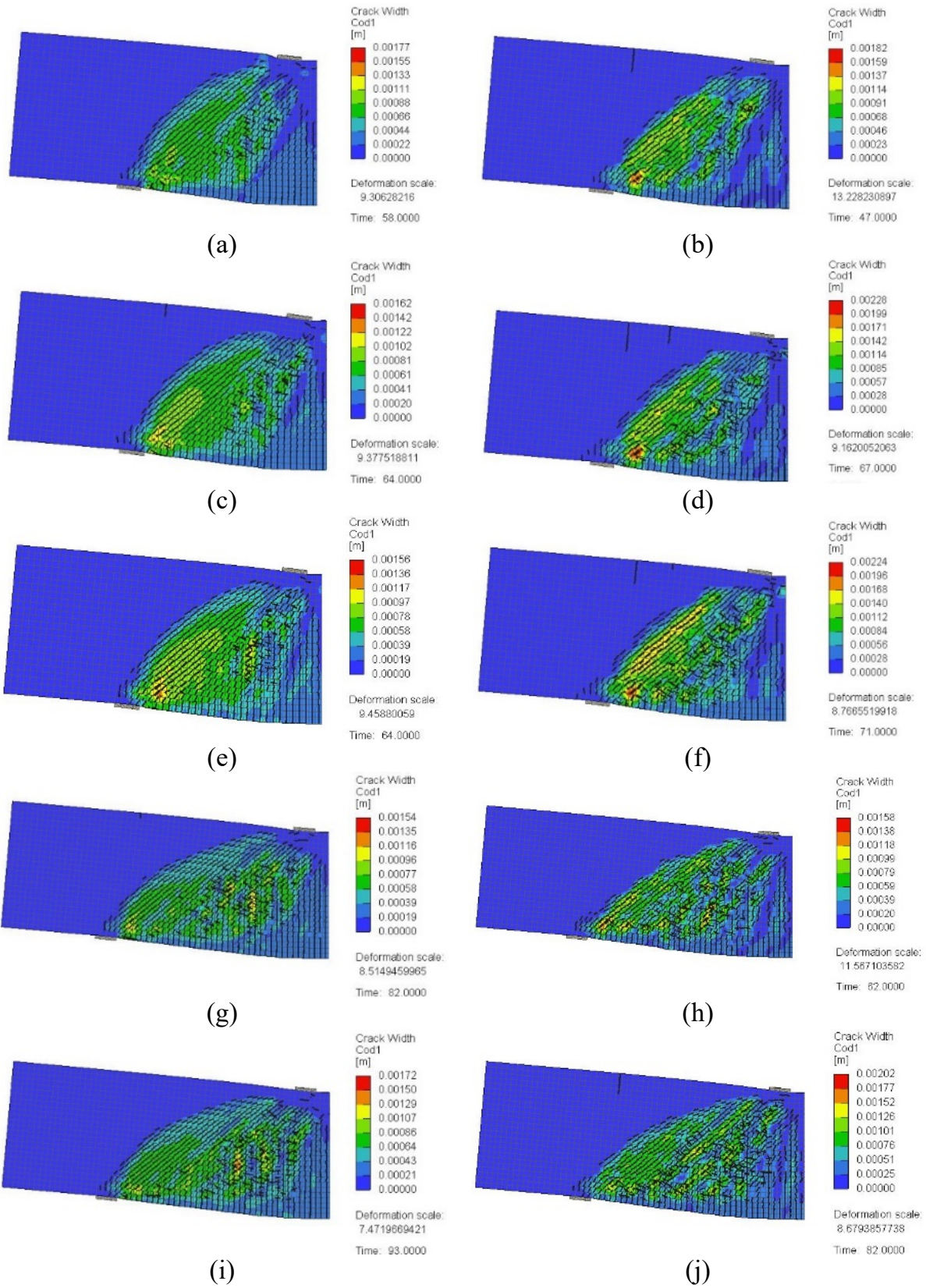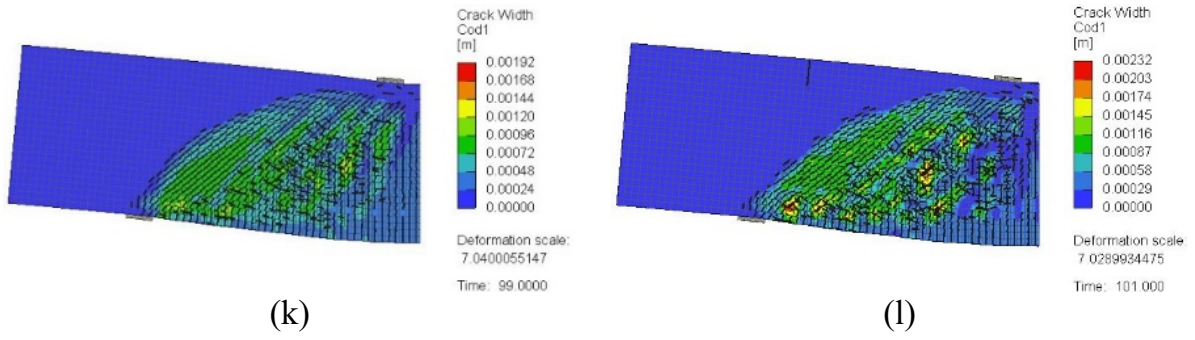
Appendices

Appendix A

(a)

(b)

(c)

(d)

(e)

(f)

Figure A.1: Crack pattern for typical solid models without web reinforcement at peak load: (a) SDB-1.0-L; (b) SDB-1.0-M; (c) SDB-1.0-H; (d) SDB-1.5-L; (e) SDB-1.5-M; (f) SDB-1.5-H

(a)

(b)

(c)

(d)

(e)

(f)

(g)

(h)

(i)

(j)

(k)

(l)

Figure A.2: Crack pattern for typical solid models with web reinforcement at peak load: (a) SDB-1.0-L100; (b) SDB-1.0-L200; (c) SDB-1.0-M100 (d) SDB-1.0-M200; (e) SDB-1.0-H100; (f) SDB-1.0-H200; (g) SDB-1.5-L100; (h) SDB-1.5-L200; (i) SDB-1.5-M100; (j) SDB-1.5-M200; (k) SDB-1.5-H100; (l) SDB-1.5-H200
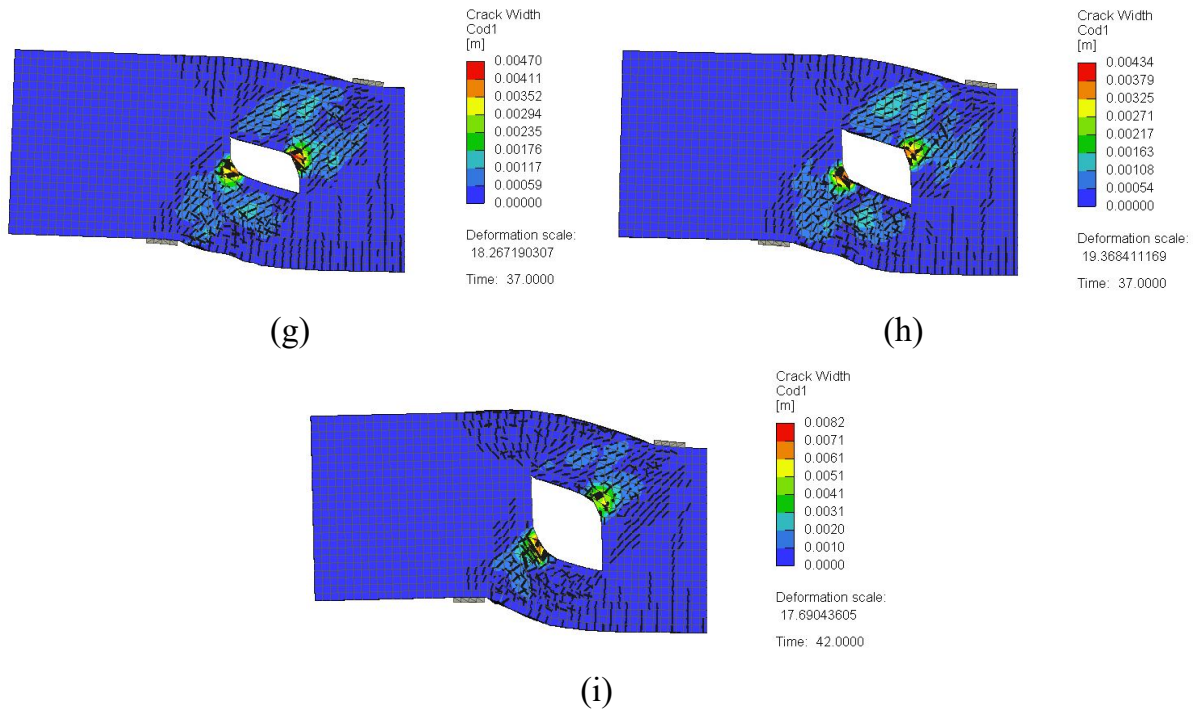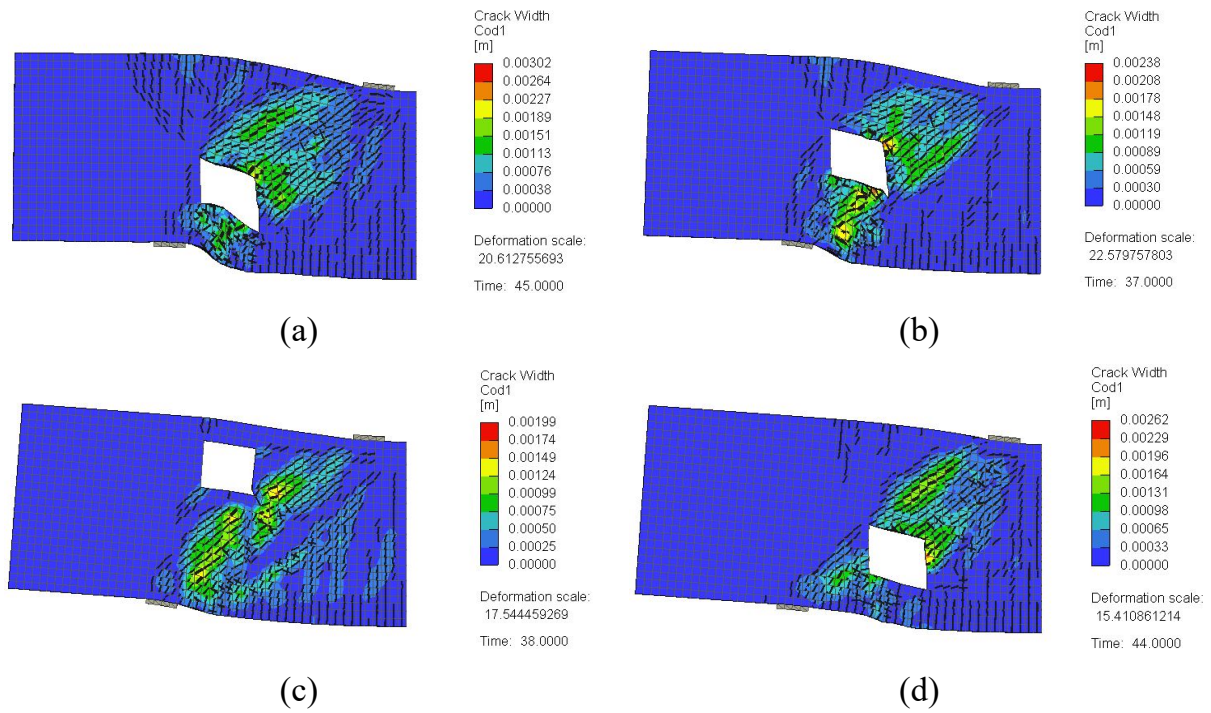

(a)

(b)

(c)

(d)

(e)

(f)

106

(g)

(h)

(i)
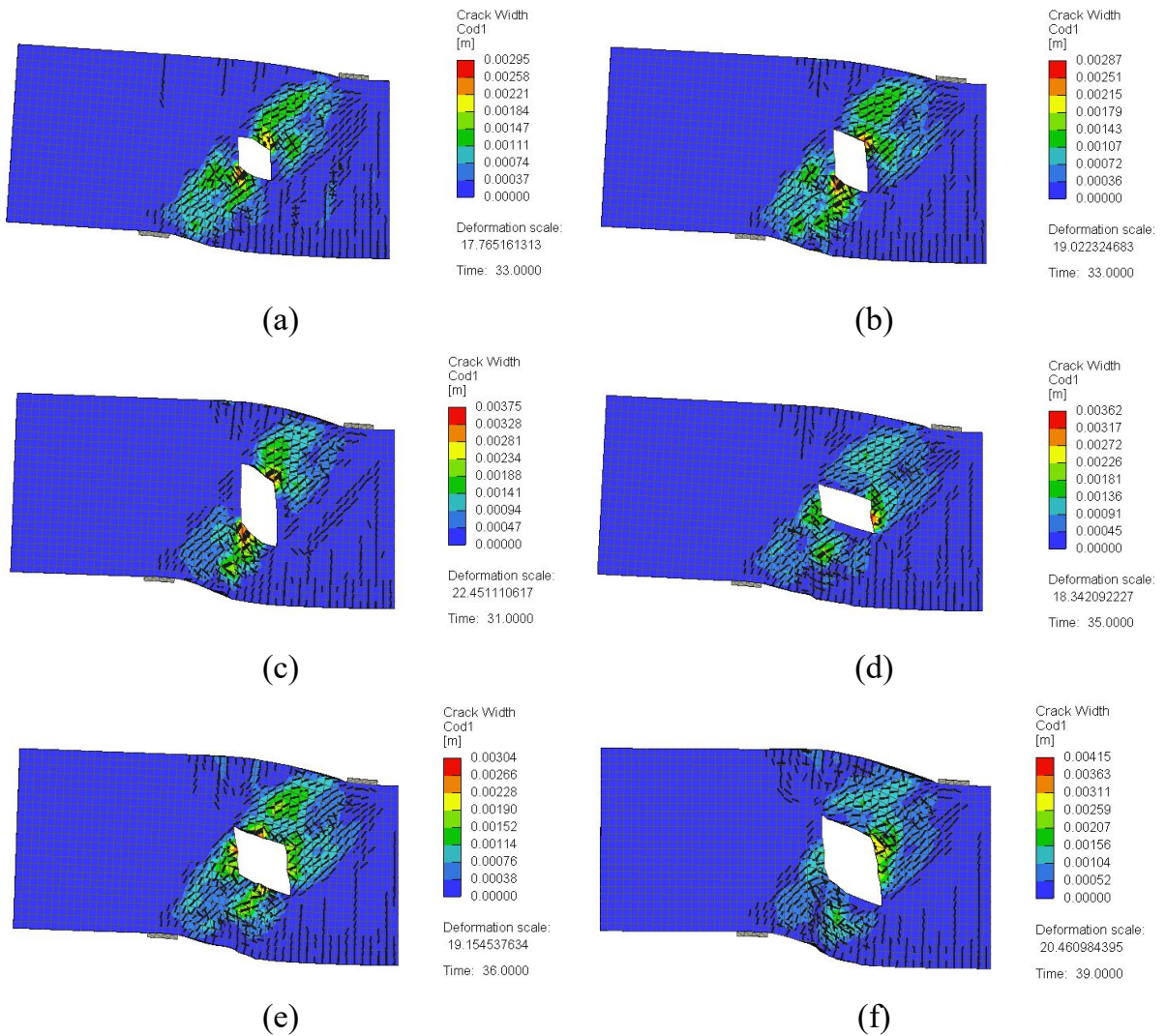
Figure A.3: Crack pattern for deep beam models with different opening sizes at peak load: (a) DB-W0.16-H0.17; (b) DB-W0.16-H0.25; (c) DB-W0.16-H0.33; (d) DB-W0.27-H0.17; (e) DB-W0.27-H0.25; (f) DB-W0.27-H0.33; (g) DB-W0.32-H0.17; (h) DB-W0.32-H0.25; (i) DB-W0.32-H0.33
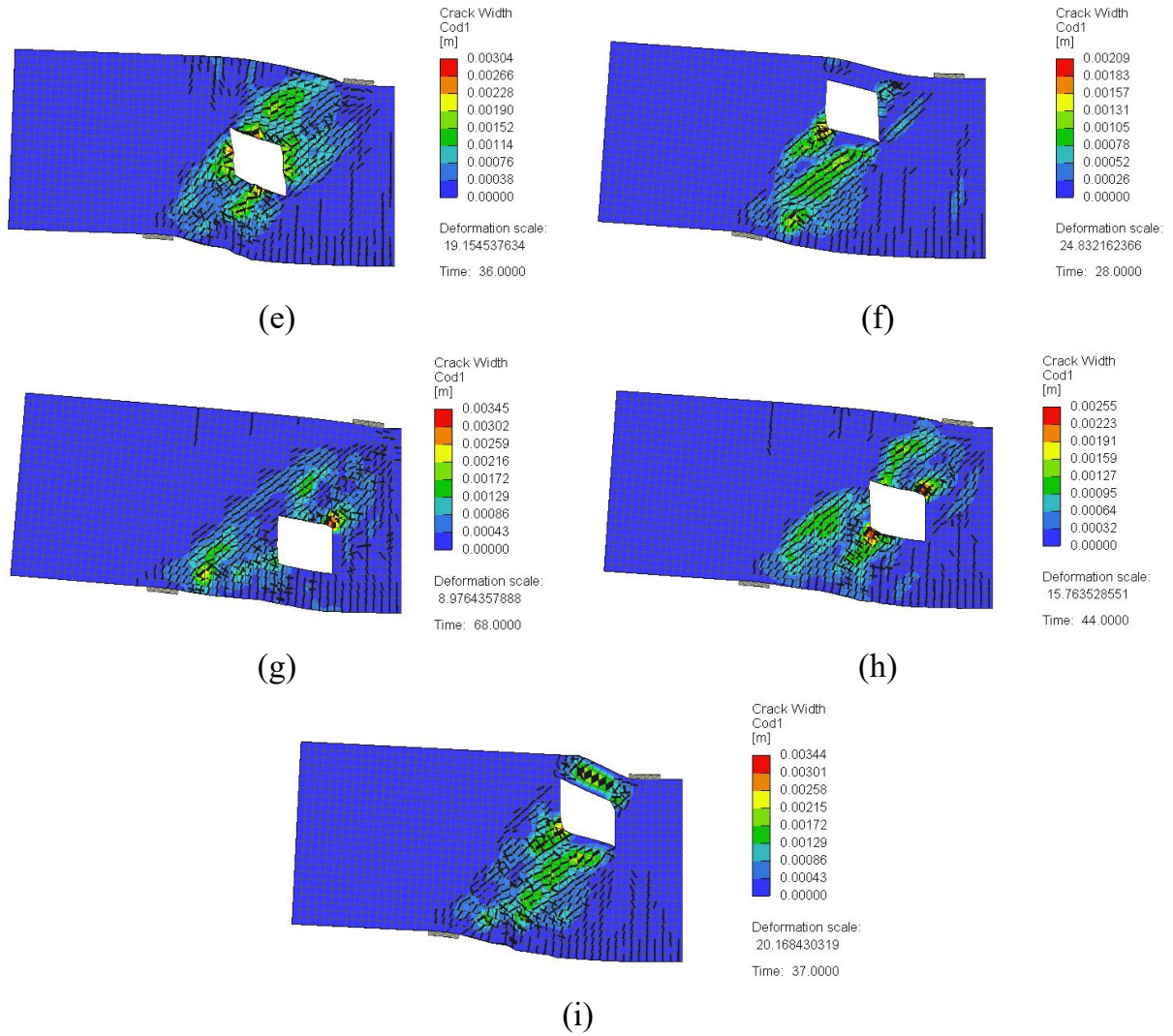
(a)

(b)

(c)

(d)

(e)

(f)

(g)

(h)

(i)

Figure A.4: Crack pattern for deep beam models with different opening locations at peak load: (a) DB-X0.25-Y0.33; (b) DB-X0.25-Y0.50; (c) DB-X0.25-Y0.75; (d) DB-X0.50-Y0.33; (e) DB-X0.50-Y0.50; (f) DB-X0.50-Y0.75; (g) DB-X0.75-Y0.33; (h) DB-X0.75-Y0.50; (i) DB-X0.75-Y0.75

UAE UNIVERSITY MASTER THESIS NO. 2023: 46

In this research 3D simulation models capable of predicting the structural behavior of GFRP-reinforced concrete beams with D-regions were developed and validated against published experimental data. A parametric study was also conducted to investigate the influence of key parameters affecting the structural behavior of GFRP-reinforced concrete deep beams with and without a web opening. Refined simplified analytical formulas were introduced for shear strength prediction of GFRP-reinforced concrete beams with D-regions.

Amena Sheikh Sobeh received her Master of Science in Civil Engineering from the Department of Civil and Environmental Engineering, College of Engineering at UAE University, UAE. She received her Bachelor of Science in Civil Engineering from the College of Engineering, Abu Dhabi University, UAE.

www.uaeu.ac.ae